ABSTRACT

Title of Dissertation: OPTIMAL CONTROL OF OBJECTS ON THE MICRO- AND NANO-SCALE BY ELECTROKINETIC AND ELECTROMAGNETIC MANIPULATION: FOR BIO-SAMPLE PREPARATION, QUANTUM INFORMATION DEVICES AND MAGNETIC DRUG DELIVERY

Roland Probst, Doctor of Philosophy, 2010

Dissertation Directed By: Professor Benjamin Shapiro
Department of Aerospace Engineering

In this thesis I show achievements for precision feedback control of objects inside micro-fluidic systems and for magnetically guided ferrofluids. Essentially, this is about doing flow control, but flow control on the microscale, and further even to nanoscale accuracy, to precisely and robustly manipulate micro and nano-objects (i.e. cells and quantum dots). Target applications include methods to miniaturize the operations of a biological laboratory (lab-on-a-chip), i.e. presenting pathogens to on-chip sensing cells or extracting cells from messy bio-samples such as saliva, urine, or blood; as well as non-biological applications such as deterministically placing quantum dots on photonic crystals to make multi-dot quantum information systems. The particles are steered by creating an electrokinetic fluid flow that carries all the particles from where they are to where they should be at each time step. The control loop comprises sensing, computation, and actuation to steer particles along trajectories. Particle locations are identified in real-time by an optical system and

transferred to a control algorithm that then determines the electrode voltages necessary to create a flow field to carry all the particles to their next desired locations. The process repeats at the next time instant. I address following aspects of this technology. First I explain control and vision algorithms for steering single and multiple particles, and show extensions of these algorithms for steering in three dimensional (3D) spaces. Then I show algorithms for calculating power minimum paths for steering multiple particles in actuation constrained environments. With this microfluidic system I steer biological cells and nano particles (quantum dots) to nano meter precision. In the last part of the thesis I develop and experimentally demonstrate two dimensional (2D) manipulation of a single droplet of ferrofluid by feedback control of 4 external electromagnets, with a view towards enabling feedback control of magnetic drug delivery to reach deeper tumors in the long term. To this end, I developed and experimentally demonstrated an optimal control algorithm to effectively manipulate a single ferrofluid droplet by magnetic feedback control. This algorithm was explicitly designed to address the nonlinear and cross-coupled nature of dynamic magnetic actuation and to best exploit available electromagnetic forces for the applications of magnetic drug delivery.

OPTIMAL CONTROL OF OBJECTS ON THE MICRO- AND NANO-SCALE BY ELECTROKINETIC AND ELECTROMAGNETIC MANIPULATION: FOR BIO-SAMPLE PREPARATION, QUANTUM INFORMATION DEVICES AND MAGNETIC DRUG DELIVERY

by

Roland Probst.

Dissertation submitted to the Faculty of the Graduate School of the
University of Maryland, College Park, in partial fulfillment
of the requirements for the degree of
Doctor of Philosophy
2010

Advisory Committee:
Dr. Benjamin Shapiro, Chair/Advisor
Dr. Pamela Abshire, Dean's Representative
Dr. Cristopher Cadou
Dr. Sean Humbert
Dr. Elisabeth Smela
Dr. Edo Waks

Dedication

I dedicate this work in memory of my grandparents, for their love and dedication.

Acknowledgements

First I would like to acknowledge my advisor Dr. Benjamin Shapiro for the years of support, guidance, effective mentoring and for promoting my creative abilities to bring out the best ideas in me. He taught me how to ask meaningful questions and the value of plain explanations. He showed me how to approach research problem, how to write academic papers and the need to be persistent to accomplish any goal. He was always there to meet and talk about my ideas, to correct my papers and to ask me good questions that helped me think through my problems. The skills I learned from him will serve me well for the years to come. Thank you Ben!

A special thanks goes to my advisory committee: Dr. Pamela Abshire, Dr. Cristopher Cadou, Dr.Sean Humbert, Dr.Elisabeth Smela and Dr.Edo Waks for their encouragements, hard questions and for raising me to this level which wouldn't have been possible without their dedication and guidance from the beginning till the end of my doctoral training.

This work would not have been possible without the dedication and enthusiastic team work of my colleges, Mike Armani, Satej Chaudhary, Zach Cummins, Arash Komaee, Rakesh Kumar, John Lin, Alek Nacev, Chad Ropp and Sina Sahand. I wish them well and a prosperous and rewarding continuation of these projects.

Last, but not least, I thank my family and friends: my parents, Eva and Robert Probst, and my sister, Renate Probst, for their support and encouragement to pursue my interests. Shabnam Tafreshi for her unconditional love, endless patience and positive spirit in times when it was most required. I would like to thank my godfather and his wife, Gábor and Emerencia Déri, for being great role models and for their wise advices. I am also very grateful to all my friends, for their contribution to a memorable time during my PhD work.

During the course of this work I was supported in parts by the Defense Advancement Research Project Agency (DARPA), by grants from the National Science Foundation (NSF) and grants from the National Institutes of Health (NIH).

Table of Contents

Dedication ii
Acknowledgements iii
Table of Contents v
List of Figures viii
Chapter 1: Introduction 1
Electrokinetic Control of Particles 1
Overview of Steering by Electrokinetic Feedback Control 4
Electrokinetic Control of Biological Cells and Microbes 7
Electrokinetic Control of Quantum Dots 14
Magnetic Control of Ferro Fluids 17
Thesis Outline 22
Chapter 2: Feedback Control of Particle by Micro Flows 23
Model of Fluid and Particle Motion 23
Particle Steering Control Algorithms 29
Minimum Power Path Planning Algorithms 35
Particle Tracking Algorithm 45
System and Measurement Model for Particle Tracking 46
Particle Identification Algorithm 50
Combination of Particle Identification and Kalman Filter 51
Tracking Multiple Particles 52
Experimental Design and Methods 54
System Setup 54
Materials used 56
Electroosmotic Flow Actuation and Particle Velocities 58
Vision System to Locate Particles in Real Time 60
Device Fabrication 62
Maximizing Actuation Strength in Control Area 68
Design Conditions for Living Cell Control 69
Experimental Sequence 71
Experimental Results 73
Steering a Single Particle 73
Steering Biological Cells 74
Steering Swimming Bacteria 76
Steering Multiple Particle 79
Steering Accuracy 82
Miniaturization 84
Chapter 3: Manipulating Quantum Dots to Nanometer Precision 85
Experimental Design Advancements 85
Steering a Single Quantum Dot 87
Positioning Accuracy 91
Autocorrelation Measurement of a Single QD 93

Chapter 4: Three Dimensional Electrokinetic Tweezers 95
Introduction 95
Device Design 97
Governing Equations 98
Controller Design 102
Accuracy and Image Sensing 104
Chapter 5: Magnetic Control of Ferro-Fluids 106
Model of Magnetic Fields and Ferro Fluid Motion 106
Ferro Fluid Steering Control Algorithms 113
Experimental Design and Methods 116
Materials Used 117
Camera and Real-Time Ferrofluid Position Detection Software 118
Control Algorithm Implementation Hardware and Software 119
Electromagnets 119
Results 120
Chapter 6: Conclusion and Outlook 122
Chapter 7: Intellectual Contributions 125
Authors Contribution to the Research within the Larger Team 127
Bibliography 129

List of Figures

Figure 1: (Top) Feedback control particle steering approach for a single particle. A microfluidic device with routine electroosmotic actuation is observed by a vision system that informs the control algorithm of the current particle position. The control algorithm compares the actual position against the desired position and finds the actuator voltages that will create a particle buffer fluid flow, at the particle location, to steer that particle from where it is to where it should be. The process repeats continuously to steer the particle along its desired path. (Bottom) Four basic flows that can be generated by applying a voltage to each electrode individually. By actuating these four flows together correctly, it is possible to generate an electrokinetic velocity at the chosen particles location in any desired direction to always carry that particle from where it is to closer to where it should be..... 5

Figure 2: Illustration of the QD positioning concept. A micro-fluidic chamber is formed by intersecting two microfluidic channels. The chamber is placed on top of a substrate, with photonic crystal microcavities etched into the substrate. The chamber is imaged by a CCD camera. External electrodes are used to position the QD in the high field region of the cavity using electroosmotic flow control. To choose the right (spectrally matched) QD for the cavity, a target QD will first be steered to a categorization location it is spectrally characterized. 14

Figure 3: Feedback control of 4 electromagnets can accurately steer a single ferrofluid droplet along any desired path and hold it at any location. Here a camera, computer, amplifier, and the 4 electromagnets are connected in a feedback loop around a petri-dish containing a single droplet of ferrofluid. The camera observes the current location of the droplet; the computer computes the electromagnet actuations required to move the droplet from where it is to where it should be; and the amplifier applies the needed voltages to do so. This loop repeats at each time to steer the droplet. 17

Figure 4: The physics of electroosmotic actuation. A schematic side view through a micro-fluidic channel is shown. The minus signs represent the fixed charges at the solid/liquid interface, circles (+ or -) show ions naturally found in the liquid (e.g. in water). These ions accumulate to shield the surface charges forming a thin Debye layer that has a predominant charge (here mostly positive). The electric field moves this layer and it drags the fluid in the channel by viscous forces. Charges in the interior of the channel remain essentially balanced (only a small fraction of the charge goes to the surfaces) and so they create no net fluid motion effect. (Figure reused with permission from Dr. Friedrich Schoenfeld, Germany.).....24

Figure 5: Electroosmotic micro-flow modes for an 8-electrode device. The above figure shows the 1st, 3rd, 5th, and 7th modes computed from the model stated above (also see [82, 125]). The two example neutral particles A and B (shown as black dots above) will then experience the velocities shown by the arrows. (Figure repeated with permission from [82].).....30

Figure 6: This figure illustrates a scenario in which particles come close to each other. The voltages needed to steer particles are shown on the right side. The horizontal lines in the graph are the maximum and minimum available voltage. 35

Figure 7: This figure illustrates the path representation as a parametric curve. The straight line represents the initial path and the dashed curved line represents the optimized path. Black squares represent the design variables which are changed dynamically by the optimization method in an effort to minimize the total cost of the path. 36

Figure 8: This figure shows the initial paths and the required voltages for steering two particles on crossing paths. The bottom of the figure shows the power optimal paths and the reduced voltages.....38

Figure 9: This figure shows the initial paths and the required voltages for steering three particles on crossing paths. The bottom of the figure shows the power optimal paths and the reduced voltages.....39

Figure 10: This figure represents the grid for multi-particle paths. Each particle is at one of the vertices of the grid and the motion of the particles is constrained along the grid. As an example the path of two

particles is shown here. Collision of the two particles is restricted by not allowing them to share the same space at the same time. 41

Figure 11: This figure illustrates the method for obtaining all possible paths for two particles moving three steps ahead. The possible combinations of the motion for one step are shown on the left. The branch and bound method for a three step path is illustrated on the right. The cost of a path is the sum of the individual costs of that path. The algorithm searches the lowest all final nodes (here at t=2) for the lowest cost. The lowest cost node defines the end node for the power optimal paths. 42

Figure 12: This figure show the power optimal path for three particles computed using the branch and bound method. The initial and final positions of the particles (A, B, C) are depicted by the subscripts 'start' and 'end'. The path for each individual particle is illustrated by solid, double and dashed lines. 43

Figure 13: This figure illustrates the combination of the particle identification method with the Kalman filter. 51

Figure 14: Schematic of the experimental setup: A CCD camera images the cells in bright-field or fluorescence illumination. A cell-tracking algorithm computes the position of the chosen cell and a control algorithm then determines the needed actuation voltages which are applied through a digital-to-analog converter (DAC) and platinum electrodes to the microfluidic device. (b) Photograph of the experimental setup with zoomed view of a microfluidic device. Here the yellow round shapes are the four reservoirs, platinum wire electrodes are brought in contact with the cell buffer fluid in these reservoirs. Left corner: The connection table for connecting the electrodes with the DAC (Measurement Computing USB-3101)....56

Figure 15: The real time algorithm for finding the (x,y) positions of all the particles. A reference image is taken of the device when there are no particles in the chamber. Then, for each incoming camera image, I subtract away the reference image to create a differential image that isolates the pixels corresponding to the moving particles. The differential image is threshold to remove the effects of noise and the centroid for each particle is computed. A Kalman filter allows tracking of individual particles. 61

Figure 16: Fabrication sequence for the micro-fluidic particle steering PDMS devices. 63

Figure 17: PDMS microfluidic device assembly sequence. 66

Figure 18: Left: Photograph of a 4-channel PDMS on glass device filled with blue food coloring to clearly show the microfluidic channels and reservoirs. Each microchannel is 10 mm long, 50 μm wide close to the particle steering intersection region and 300 μm wide otherwise, and 10 μm deep. Right: Schematic of the channel intersection and the 100 μm × 100 μm cell steering control area....67

Figure 19: Left: The 8-electrode PDMS on glass device. Here the white bulb shapes are the eight reservoirs (big reservoirs are used to minimize surface tension driven pressure flows and electrochemical effects), platinum wire electrodes are brought in contact with the fluid in the reservoirs. In these wells, the 8 channels (each 7 mm long, 50 μm wide, 11 μm deep) are not visible, and a blue LED light (used to illuminate the fluorescent particles) brightly illuminates the center of the device. Right: A mask (a zoom) of the particle steering region (300 μm diameter, 11 μm deep)....68

Figure 20: Left: Electric field distribution for both devices measured on a horizontal line across the device. The electric field in the center of the optimized devise (right top) has improved by a factor of 4. 69

Figure 21: Control of a bead with significant surface charge along a figure 8. The bead has an approximate electrophoretic mobility of c = -57.3 ± 5.6 x 10^{-9} m^2 V^{-1} s^{-1}. (By comparison, the electroosmotic mobility of my PDMS devices is u = 36.5 ± 3.6 x 10^{-9} m^2 V^{-1} s^{-1}.) Left: Photograph of the micro-fluidic devices with the figure 8 path super-imposed on the image. Right: The actual path of the chosen 5 micron polystyrene bead (Polysciences Inc.) (black circle) in the feedback control experiment. Snapshots are shown at 6 equally spaced times. The bead follows the required trajectory to within three microns. 74

Figure 22: Steering of a slightly charged yeast cell along a UMD path. The cell has an approximate electrophoretic mobility of -23.3 ± 6.9 x 10^{-9} m^2 V^{-1} s^{-1}. Left: Photograph of the micro-fluidic devices with the cursive 'UMD' path overlaid on the image. Right: The actual path of the chosen 5 micron yeast cell (Red Star® Yeast) (black dot) in the feedback control experiment. Snapshots are shown at 6 equally spaced times for each letter. The yeast cell follows the required trajectory to within one micron. (This experiment was an optimized version of the Figure 21 experiment.) 75

Figure 23: Four sequential snapshots of a red blood cell being steered along an UMD path, drawing out "UMD" (University of Maryland). 75

Figure 24: A motile microbe found in river water was moved on a circular trajectory (actual trace shown in dashed white) and trapped in the center for 22 seconds until being released from control (dashed red). 76

Figure 25: A motile microbe was steered around a trajectory spelling "PCS" (Probst, Cummins, and Shapiro, respectively). The microbe position at 6 time snaps is shown by the red squares. At the end of the trajectory, the microbe was freed from control allowing it to swim away (dashed white outward trajectory) and then reclaimed to the beginning of the trajectory (dashed white return path). Bacteria viability after control was verified by visual observation of its subsequent swimming activity. 77

Figure 26: (a) A fast swimming microbe found in river water was moved to an arbitrary trapping location and trapped for 30 seconds until being released from control. Uncontrolled swimming is shown in dashed white, initial control to the trap or path is shown in green, and the controlled motion is shown in blue – as is evident, the microbe swims away after the control is turned off. (b) A worm was steered around a trajectory spelling "LOC" (for lab-on-a-chip). 77

Figure 27: Steering of 3 fluorescent beads (2.2 μm diameter, Duke Scientific) with large surface charge (electrophoretic mobility of -92.0 ± 15.6 x 10^{-9} m^2 V^{-1} s^{-1}) around 3 circles. The electroosmotic mobility of my PDMS devices is u = 36.5 ± 3.6 x 10^{-9} m^2 V^{-1} s^{-1}. In the experiment, the fluorescent beads appear as small green dots on a black background and the device geometry, which does not fluoresce, is not visible. Here, the white dots are the beads (enlarged), the blue curves are the actual trajectories that the target beads have traced out (overlaid), and the dashed white curves (also overlaid) show the geometry of the channels and the particle control chamber. Snapshots are shown at three time steps. The three beads are being steered to within an accuracy of one pixel (corresponding to less than 1 μm). The desired paths are not shown because, at this image resolution, they would perfectly underlay the actual paths. 79

Figure 28: Steering of 2 fluorescent beads around 2 circles while a 3rd bead is held stationary. The trapped bead is marked by the arrow, and is held in place by the control algorithm to an accuracy of better than one micron. Every time the bead deviates from its desired position, a flow is created that pushes the bead back towards its desired location. (The properties of the beads and the format of the figure are the same as in Figure 27.) 80

Figure 29: Steering of 3 yeast cells with small surface charge (electrophoretic mobility -23.3 ± 6.9 x 10^{-9} m^2 V^{-1} s^{-1}) around two circles and a 'UMD' path (for 'University of Maryland'). The cells do not fluoresce. In these images there is no high-pass filter before the camera and the raw images are shown. The yeast cells are visible as small black dots with a white center (the three target cells are marked with a white arrow in each image), and the white curves are the trajectories that the target cells have traced out. The three beads are being steered to within an accuracy of one pixel (corresponding to less than 1 μm). 81

Figure 30: The control algorithm can correct for large errors in particle positions. This figure shows steering of three fluorescent beads (2.2 μm diameter, Duke Scientific) around three circles. At time t=24 s, corresponding to bead positions marked A1 , A2 , and A3 , the control was turned off for 11 s, allowing the particles to drift away (primarily due to the slow parasitic flow caused by surface tension forces at the reservoirs) by up to 150 μm. The control was then turned back on at t = 35 s (B1 , B2 , and B3), and the control algorithm steered the three original beads back to their desired positions (C1 , C2 , and C3). Four time instants are shown. (a) Right before control is turned off. (b) Right before control is turned back on (the three beads have drifted away a large distance). (c) At a time when the beads are back on track. (d) Final time when the beads have completed the remainder of their three

circular paths (again to an accuracy of better than 1 μm). The two straight lines in the last image illustrate the left and right boundaries of the control region. The control voltages scale with the size of the position errors. Position errors are very large and this would lead to very large control voltages. Therefore, the control scheme has been slightly modified: the control gain per particle is scaled in such a way that the voltage remains within the allowable [-10, +10] Volt range. 82

Figure 31: This figure shows the handheld prototype with a close-up of the microfluidic channels at the center. 84

Figure 32: Illustration of the optical and electronic setup for tracking and feedback control of QDs. A CCD camera images the QD and sends the information to a tracking algorithm that uses sub pixel averaging to accurately determine the current position of the QD. The control algorithm uses this information to determine the proper voltage to apply to the electrodes in order to move the QD to its desired position. A second feedback loop moves the imaging objective in the z-direction using a piezo stage to keep the QD in focus. 87

Figure 33: Single quantum dot trajectory. (A-C) Time stamped CCD camera images of a single quantum dot being steered along the desired trajectory (full movie available in supporting online material). The white trace shows the measured path of the quantum dot up until its current location. The square magenta box shows the sub pixel averaging window used to determine the current position of the QD. The inset in panel (A) shows a close-up of the sub pixel averaging window which contains the QD near its center. (D) Plot of quantum dot position along its trajectory. The dotted black line shows the desired trajectory programmed into the controller. The actual measured QD trajectory is shown in blue. The solid red squares depict when the quantum dot blinks off. At the end of the trajectory the QD is held in place for 2 minutes. The deviation of the QD trajectory from the desired trajectory is calculated to be 152 nm. 89

Figure 34: Measurement of QD positioning accuracy. Blue points represent the measured position of the QD as it is held in a desired location by flow control for 5 minutes. The standard deviation of the blue points is calculated to be 84.3 nm. The controller is subsequently turned off and the QD is allowed to drift away for another five minutes, as shown by the red points. The drift to the right is caused by a small pressure flow in the device, a flow that is continuously corrected for when feedback control is on. To determine the vision accuracy of the system a third experiment is carried out for a QD adhered to a glass slide. The positions of the adhered QD are shown in green and have a standard deviation of 28.5 nm. 91

Figure 35: *In situ* autocorrelation measurement of a single QD. Autocorrelation measurement of a single controlled quantum dot obtained from a 15 minute integration with 1 ns binning and with exponential fits shown. From the exponential fit we determine $g^2(0) = 0.37 \pm 0.02$ and decay time $t_d = 22.73 \pm 1.07$ ns. 94

Figure 36: Device design for 3D electrokinetic tweezing. By applying voltages between channels in the top and bottom layer, an up or down electrophoretic force or electroosmotic flow component can be created at the particles location, in addition to the usual horizontal actuation. 98

Figure 37: Basic mode of electrophoretic and electroosmotic velocities in a vertical plane. The created velocities are shown at each location for the shaded vertical plane and in particular for the central particle position marked in black. 102

Figure 38: Control of one particle (black dot) on a vertical infinity path by EO actuation. The desired path of the particle is in thin black, the achieved path is in thick black, and the arrows show the EO velocity field at each time. 103

Figure 39: Two particles controlled simultaneously on two orthogonal circular paths. Horizontal and vertical paths are shown at the top and the bottom of the figure respectively. The desired path of the two particles (A and B) is in thin black, the achieved path is in thick black. The (red) arrows show the EP velocity field at each time. Arrows that show up as round dots show flow coming out of the plain. 104

Figure 40: Two nano particles (diameter 10nm) controlled simultaneously under presence of Brownian motion and 50% charge mismatch. 105

Figure 41: The magnetic field created by a single electromagnet magnet and the resulting force on a ferromagnetic particle at any location in the Petri dish. The resulting force directions, according to equation (34) below, are shown by the black arrows at each location. The magnetic field is represented by stream lines. The particle is always attracted to regions of highest magnetic field intensity, i.e. here to the right magnet.....107

Figure 42: This figure shows the simulated motion direction and the resulting error if I actuate the 2nd electromagnets with -3 Volts and the 3rd electromagnets with +2 Volts simultaneously. 114

Figure 43: This figure illustrates the set (database) of pre-computed force field modes resulting from the electromagnets. The magnetic force on the ferrofluid is represented by arrows and the magnetic field is represented by stream lines. On the left is the set of partial modes for a single magnet actuated from -10 to 10 volts and in the middle and on the right is the set modes for partial combinations of two and three magnets individually actuated from -10 to 10 volts. The modes that are visible in the figure were produced by actuating the magnets with 1V.....115

Figure 44: Figure shows the two chosen modes for optimization. These modes can be rotated to achieve motion that consists of movements of multiples of 45deg and the forces can be increased or decreased by changing the actuation voltage. 116

Figure 45: Control of a medium size 15 μL (1.2 mm radius) ferrofluid droplet slowly along a UMD path.....121

Chapter 1: Introduction

In micro-scale technologies and medical applications, there is a need to put things where they need to go (cells into testing chambers or to sensor locations, quantum dots into photonic cavities and drugs into tumors), and this is difficult to do on the micro scale. This document demonstrates two methods based on feedback control of electrokinetic and magnetic fields to steer, place, and hold objects in 2D and 3D micro-fluidic and magnetic systems.

Electrokinetic Control of Particles

The ability to steer individual particles inside micro-fluidic systems is useful for navigating particles to localized sensors, for cell sorting, for sample preparation, and for combinatoric testing of particle interactions with other particles, with chemical species, and with distributed sensors. A variety of methods are currently used to manipulate particles inside micro-fluidic systems: individual particles can be steered by laser tweezers [1-3]; they can be trapped, and steered to some degree, by dielectrophoresis (DEP) [4-7]; and by traveling-wave-dielectrophoresis (TWD) [7, 8]; held by acoustic traps [9]; steered by manipulating magnets attached to the particles [10]; and guided by a MEMS pneumatic array [11]. There is also a feedback control approach (similar to the one developed in this paper) used by Cohen [12, 13] to trap and steer a single particle, but not yet multiple particles, using electroosmotic or electrophoretic actuation.

Of these methods, laser tweezers are the gold standard for single particle manipulation. Ashkins survey article [1] provides a history of optical trapping of small neutral particles, atoms, and molecules. Current laser tweezers systems can create up to four hundred three-dimensional traps, they can trap particles ranging in size from tens of nanometers to tens of micrometers, trapping forces can exceed 100 piconewtons with resolutions as fine as 100 attonewtons, and the positioning accuracy can be below tens of nanometers [2, 14]. However, optical tweezers require lasers and delicate optics and the whole system is unlikely to be miniaturized into a hand-held format. The other methods mentioned above (DEP, acoustic traps, manipulation via attached magnets, and steering via pneumatic arrays systems) can be miniaturized into hand held formats but their steering capabilities are not as sophisticated as those of laser tweezers.

My approach uses vision-based micro-flow control to steer particles by correcting for particle deviations – at each time I create a fluid flow to move the particles from where they are to where they should be. This allows very simple devices, actuated by routine methods, to replicate the planar steering capabilities typically requiring laser tweezers. I have shown that my approach permits a PDMS device with four electrodes to steer a single cell, and a device with eight electrodes to steer up to three particles simultaneously. The method is non-invasive (the moving buffer simply carries the cells along), the entire system can be miniaturized into a hand held format (both the control algorithms and the optics can be integrated onto chips), I can steer almost any kind of visible particle (neutral partices are carried along by the

electroosmotic flow, charged particles are actuated by a combination of electroosmosis and electrophoresis), and the system is cheap (the most expensive part is the camera and microscope, and these will be replaced by an on-chip optical system for the next generation of devices).

Due to the correction for errors provided by the feedback loop, the flow control algorithm steers the particles along their desired paths even if the properties of the particles (their charge, size, and shape) and the properties of the device and buffer (the exact geometry, the zeta potential, pH, and other factors) are not known precisely. The fundamental disadvantage of my approach is its lower accuracy as compared to laser tweezers: the positioning accuracy will always be limited by the resolution of the imaging system and by the Brownian motion that particles experience in-between flow control corrections. The current optical resolution is on the order of one micron, and the particle Brownian drift during each control time step is less than eighty nanometers.

Both *feedback* and *micro*-flows are essential for particle steering capability. Feedback is required to correct for particle position errors at each instant in time. Micro-fluidics is required because macro-flows exhibit more complex dynamics, due to their momentum effects, and it is not possible to find the external actuator inputs that will reliably create macro-flows to steer particles. On the micro-scale, the Stokes equations can be inverted to determine the necessary actuation that will steer many particles at once.

Overview of Steering by Electrokinetic Feedback Control

Figure 1 shows the basic control idea for a single particle: a micro-fluidic device, an optical observation system, and a computer with a control algorithm, are connected in a feedback loop. The vision system locates the position of the particle in real time, the computer then compares the current position of the particle with the desired (user input) particle position, the control algorithm computes the necessary actuator voltages that will create the electric field or the fluid flow that will carry the particle from where it is to where it should be, and these voltages are applied at electrodes in the micro-fluidic device. For example, if the particle is currently North/West of its desired location, then a South/East flow must be created. The process repeats at each time instant and forces the particle to follow the desired path (see also [15]).

Both neutral and charged particles can be steered in this way: a neutral particle is carried along by the flow that is created by electroosmotic actuation, a charged particle is driven by a combination of electroosmotic and electrophoretic effects. In either case, it is possible to move a particle at any location to the North, East, South, or West by choosing the appropriate voltages at the four electrodes. It is also possible to use this scheme to hold a particle in place: whenever the particle deviates from its desired position, the electrodes create a correcting flow to bring it back to its target location.

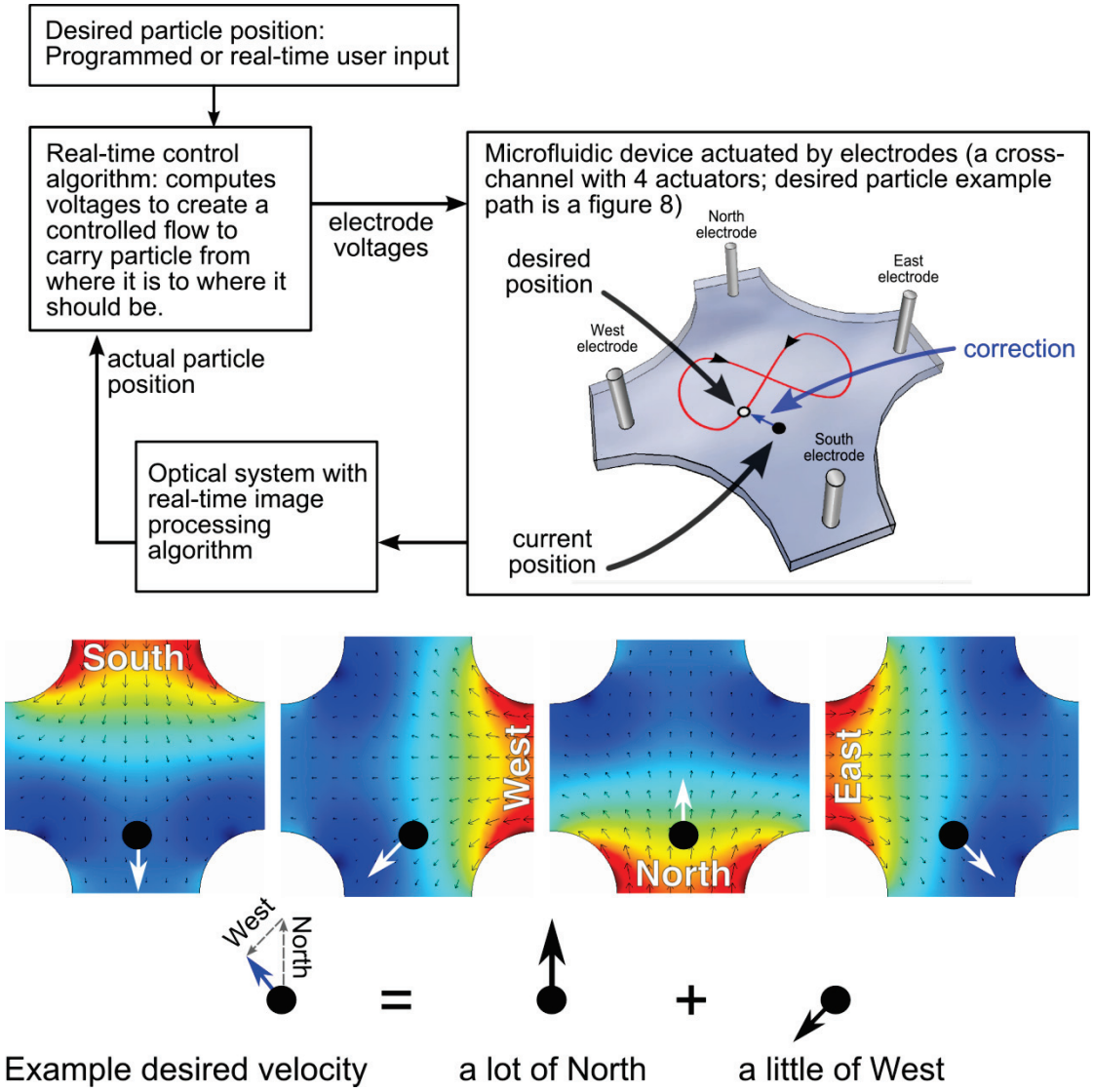

Figure 1: (Top) Feedback control particle steering approach for a single particle. A microfluidic device with routine electroosmotic actuation is observed by a vision system that informs the control algorithm of the current particle position. The control algorithm compares the actual position against the desired position and finds the actuator voltages that will create a particle buffer fluid flow, at the particle location, to steer that particle from where it is to where it should be. The process repeats continuously to steer the particle along its desired path. (Bottom) Four basic flows that can be generated by applying a voltage to each electrode individually. By actuating these four flows together correctly, it is possible to generate an electrokinetic velocity at the chosen particles location in any desired direction to always carry that particle from where it is to closer to where it should be.

Surprisingly, it is also possible to steer multiple particles independently using this feedback control approach [16]. A multi-electrode device is able to actuate multiple fluid flow or electric field modes. Different modes cause particles in different locations to move in different directions. By judiciously combining these modes, it is possible to move all particles in the desired directions.

The algorithm requires some knowledge of the particle and system properties (charged particles exhibit electrophoresis and react differently than neutral particles) but this knowledge does not have to be precise: the reason is that feedback, the continual comparison between the desired and actual particle positions, serves to correct for errors and makes the system robust to experimental uncertainties [17, 18]. Even though my experiments have sources of error, some of which are unavoidable, such as variations in device geometry, parasitic pressure forces caused by surface tension at the reservoirs, Brownian noise, and variations in zeta potentials and charges on the particles – the control algorithm still steers all the particles along their desired trajectories.

Electrokinetic Control of Biological Cells and Microbes

The ability to manipulate individual living biological cells is useful for steering and confining them to sensing locations or for directing them to chemically functionalized locations on chip. It can allow precision sample preparation steps such as extracting individual cells from heterogenous liquid samples and cell-by-cell sorting. For swimming cells, it can allow on-demand precise and fast chemotaxis and cell motility studies by repeatedly placing cells in desired locations with respect to chemical gradients or on-chip obstacles.

Single cells can be manipulated by direct physical contact or through indirect means. Biologists have been manipulating individual cells by applying suction through hollow glass micropipette tips since Barber [19] first published this technique in 1904. More recently, direct contact atomic force microscopy (AFM) [20], and robotic micro-grippers [21, 22] have been used to hold and position living cells.

In existing non-contact techniques, cells are manipulated by laser tweezers[3, 23-26], optoelectronic tweezers (OET's) [4, 27, 28], by dielectrophoresis (DEP) [5, 29, 30], electrophoresis (EP) [31-33], magnetic tweezers [34-36] or acoustic traps [37, 38]. All of these methods use external fields (optical, electrical, magnetic, or ultra sound waves) to generate actuation forces which are used to trap or steer the cells.

Laser tweezers remain the gold-standard non-contact single cell manipulation method allowing trapping and steering of single cells [3, 23, 25]. Such tweezers use focused laser beams to exert an optical gradient force upon cells and can trap cells to nanometer precision [39, 40]. Laser tweezers can manipulate cells in cell medium and long range manipulation is achieved by moving the microscope stage while keeping the laser trap position constant[41]. To avoid local heating and optically induced damage to the cells it is better to use infrared light [42-44].

However, stable optical traps require high numerical apperatures (NA > 1.2) objectives, but since these have been designed for visible light, IR transmission (and hence applied forces) can vary substantially. Additionally, optical trapping is restricted to optically homogenous and highly purified sample preparations[45]. For these reasons, it is a difficult, delicate, and expensive task to use laser tweezers as a robust method to routinely manipulate living cells in biology laboratories.

Recently, optoelectronic tweezers (OET's) have been used to manipulate and transport individual cells over long distances[4]. OET's make use of dynamic virtual electrodes, created by projected images onto a photo-conductive surface, these create a non uniform AC electric field that exerts a DEP force upon polarizable particles such as biological cells. The magnitude of the force on each cell depends on the dielectric constant of that cell versus the dielectric constant of the buffer medium and the frequency of the applied AC electric field (both of

which are the same across the entire device).

I use controlled micro flows to accurately manipulating single cells, including motile or swimming cells. This method is simple, cheap, and easy to use. It can be achieved with a 4-electrode PDMS device that can be created in less than an hour, a standard microscope and a digital-to-analog converter (DAC), and vision and computer control software. My method can position any desired cell to any desired location in a cell buffer medium and can steer it along any desired path. The overall advantage of this system is that any freely suspended cell, regardless of its size, shape, dielectric constant, or whether it is swimming or not, can be controlled by always changing the buffer flow to gently carry the cell from where it is to where it should be.

The system can also position swimming microbes to any desired location, steer them along any desired path as they continue to swim, let them go, and reposition them; The key advantage is that it is easy to correct large excursions: even if the microbe is many micrometers away from its desired location, I can create a flow to bring it back. To my best knowledge, this is the first demonstration of precision control of swimming cells on chip.

The velocity that is created at the cell location is an electro-kinetic velocity. It is the sum of electroosmotic (EO) and electrophoretic (EP) velocities. EP refers to the motion of a charged particle under an applied electric field[46, 47]. EO is the

motion of a fluid under an applied electric field[46, 47]: here the applied electric field moves the fluid and the fluid carries the cell. Both effects move any cell in the direction of the applied electric field at its location, but the magnitude of the velocity for each effect depends on the EP and EO mobility coefficients [31-33, 48, 49]. The control is insensitive to unknown or poorly known mobility coefficients. I have achieved single-micrometer steering accuracy of micro-scale particles or yeast cells even if the pH, and hence the electroosmotic zeta potential, is not controlled and if the charge on the cells varies by as much as ±50%. Thus these control algorithms allow simple and inexpensive PDMS devices to achieve precision cell control regardless of cell-to-cell property variations.

The system described here is a simple 4-electrode microfluidic device made of polydimethylsiloxane PDMS [50-53] which is reversibly bonded to a glass slide. PDMS is routinely used to make chips that handle cells and biological samples, it provides a safe environment for living cells, and it is visually transparent allowing vision-based cell control. The porous structure of PDMS provides good permeability for oxygen and carbon dioxide[51, 54]. Soft lithograpy methods for fabricating PDMS microfluidic devices are straight-forward and will allow biology laboratories to reproduce these single cell control capabilities. The necessary replica mold can be ordered from one of the microfluidics foundries[55, 56] or fabricated in a standard university clean room [51, 53, 57]. Additional features that are now standard in microfluidic devices, such as chemically functionalizing specific regions or adding barriers (for cell motility studies around

obstructions), can be incorporated into my system. Alternately the PDMS device can be layed on top of a previously optimized glass or silicon system.

Cell manipulation is carried out in a control region that is defined by the intersection of two crossing microchannels. Applying a voltage to electrodes, placed in the reservoirs at the end of the channels, generates a small electric field and thus electrokinetic forces. Figure 1 shows the four basic electric fields generated in the control region by applying a voltage to each electrode individually. By actuating these four flows together correctly, it is possible to generate an electrokinetic velocity at the chosen cells location in any desired direction to carry that cell from where it is towards where it should be. Manipulation of motile cells is achieved by creating a correction velocity that is larger than the swimming speed of the cell and thus still achieving precise steering or trapping control.

Electrokinetic actuation is gentle and suitable for manipulation of living micro-organisms[31]. Leopold et al.[33] reviews the applicability of electrokinetics to move living organisms such as viruses, bacteria, and eukaryotic cells. Ebersol et al.[58] found that the majority of tested bacteria remained viable in electric fields of even 10,000 V/m. I have minimized the electric fields used in my devices. For my ±10 V electrode actuation, the maximum electric field strength produced in my device is approximately 4,000 V/m which is reported to be safe for living cell cultures[59, 60]. By design, my microchannels are wide (300 μm) everywhere except at the orfice near the manipulation region (50 μm).

This design has several advantages. It allows device operation with low voltages and thus enables safe cell handling and reduces electrolysis at the electrodes in the fluid reservoirs[61]. The overall smaller channel dimensions minimize Joule heating due to the smaller channel cross-sectional areas (and thus the lower currents). The large electrode reservoirs create shallower fluid/air menisci and thus minimize surface tension pressures that reduce the pressure flows which acts as disturbances to cell control.

The method controls cells that are suspended in a buffer. It is not meant to control cells once they have adhered to the chip surface (although precisely directing flow above such cells might still bias their motion towards desired on-chip locations).

For some choices of buffer, e.g. diluted blood, electroosmotic actuation may not be effective (for blood this is likely due to fouling of the chip surfaces which can impede EO actuation). In that case, the issue becomes whether the target cell has enough surface charge to enable its electrophoretic actuation. If neither the fluid nor the cell can be moved by EO or EP means, then cell control cannot occur.

Currently, I can only control motile cells whose swim speed is less than approximately 10μm/s. Swimming cells contribute an added velocity independent of the applied control resulting in a positioning error. This error can be reduced by estimating the swimming velocity based on the past swim direction of the bacteria, but this method ceases to be effective when the cell changes direction faster than the

control loop operates. Manipulation of fast swimmers can be achieved by speeding up the control loop: by using a faster camera (right now I use a standard 30 Hz frame rate camera) and a faster control update to correct the position of the bacteria more often per second. I am currently optimizing methods to control such fast swimmers and I will report results for this in future publications.

Manipulation and control of nanoscopic objects such as quantum dots (QDs) are fundamental requirements for a broad range of applications in the fields of photonics, nanoelectronics, and biology. For example, precision placement of single quantum dots in the high field region of both nanophotonic[62-64] and plasmonic [65, 66] structures enables quantum information processing [67]. QDs also serve as biological tags [68] enabling *in situ* characterization of biological molecules and controlled investigation of biological processes.

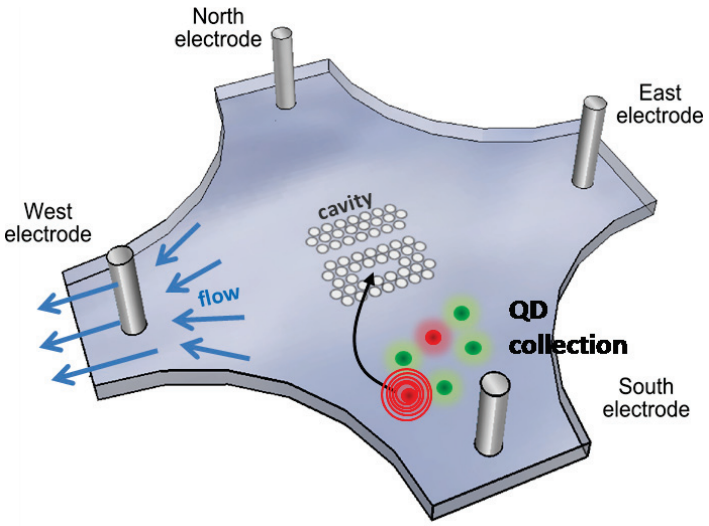

Figure 2: Illustration of the QD positioning concept. A micro-fluidic chamber is formed by intersecting two microfluidic channels. The chamber is placed on top of a substrate, with photonic crystal microcavities etched into the substrate. The chamber is imaged by a CCD camera. External electrodes are used to position the QD in the high field region of the cavity using electroosmotic flow control. To choose the right (spectrally matched) QD for the cavity, a target QD will first be steered to a categorization location it is spectrally characterized.

To date, the most notable successes of nanoparticle manipulation have been demonstrated using optical tweezers [1, 69] and optofluidic devices [70, 71]. These methods make moveable active traps, either by laser-created optical gradient forces or by dynamic virtual electrodes that exert dielectrophoretic forces on polarizable particles. However, optical and dielectric forces scale with volume, making the trapping of nanoscopic objects such as QDs extremely challenging [72]. Furthermore, these trapping forces are non-specific in that all particles are pulled in, resulting in a significant probability for capturing multiple objects. These drawbacks are highly limiting in quantum optics applications where capture of multiple particles can ruin the single photon nature of the emission, and in biological applications where objects are easily damaged by bright lasers [45].

Here I demonstrate a method to manipulate and position nanoscopic objects with nanometer precision without using traps. Instead, precision manipulation is achieved by moving the surrounding fluid. The fluid is actuated by electroosmosis where an applied electric field moves a layer of surface ions that subsequently pulls the fluid, along with any suspended objects, by viscous drag [47]. The position of a chosen object is measured in real time with a microscope and a sub-pixel imaging algorithm that provides sub-wavelength of light tracking accuracy, and flow is created to move that object from its current location to a desired position in discrete time steps. Since only the chosen object is always corrected back towards its target location, all other nearby objects are not controlled and drift away by a combination of random Brownian motion and diverging non-correcting fluid flows at their locations in the

device. This flow control approach is particularly promising for manipulation of extremely small dielectric particles, such as QDs, where trap approaches typically fail due to the small particle volume and because resonance enhancement is not possible. To demonstrate this advantage, this work focuses on the manipulation of single QDs which have an ellipsoidal core/shell structure and a diameter of 12 nm (6 nm) on the major (minor) axis.

The manipulation of nanoscopic objects is challenging due to their small size which increases Brownian motion. Quantum dots are particularly difficult to control due to their inherent blinking which makes them optically invisible for periods of time (*20*). For these reasons, previous attempts to trap QDs were limited to 2 μm precision and only 90 seconds of trapping time [73]. In addition, such demonstrations were limited to only trapping (random capture of QDs) and not positioning (moving a chosen QD from its current location to the desired location) or manipulation (moving particles along well defined paths). This approach enables me to fully manipulate nanoscopic objects in two dimensions. Any QD in the field of view can be moved from its current location to the desired location over a well defined path with nanometer precision for times exceeding one hour. In addition, since I have the ability to both position and trap in a large control area, the technique is insensitive to QD blinking. When a QD blinks off, I can wait for it to blink back on and immediately reposition it back to the correct location even if it has drifted a significant distance away due to Brownian motion.

Magnetic Control of Ferro Fluids

The ability to magnetically target anticancer agents to cancerous tissue using magnetic particles can increase local drug efficacy and reduce unwanted side effects in cancer treatment. The specific objective is to extend a clinically-tested magnetic drug-delivery method [74-76] to target tumors deep inside the body. The inability to focus particles to deep targets is a long-standing and well-recognized problem in magnetic drug delivery. This problem is addressed by dynamic controlling safe magnetic fields to focus nano-scale drug-coated magnetic particles to tumors deep inside the body.

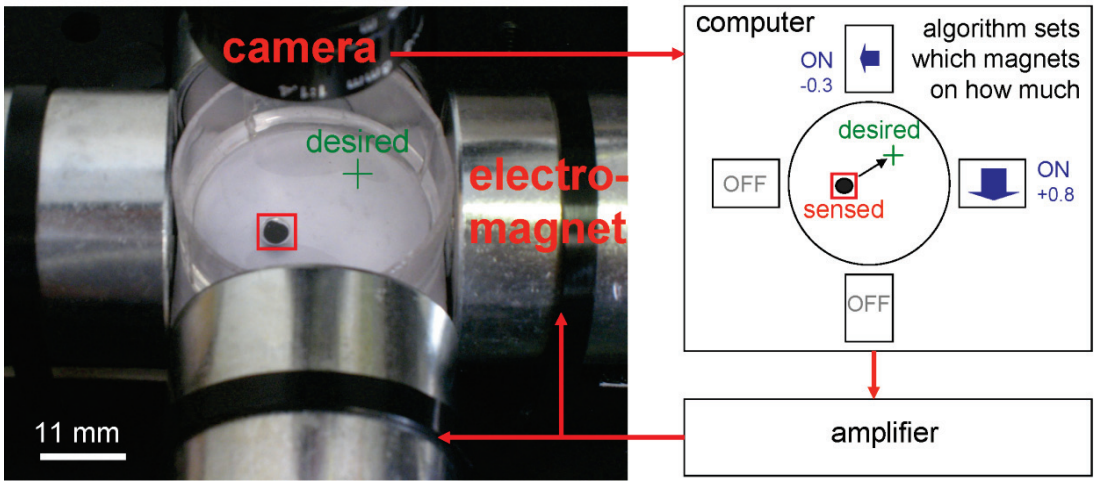

Figure 3: Feedback control of 4 electromagnets can accurately steer a single ferrofluid droplet along any desired path and hold it at any location. Here a camera, computer, amplifier, and the 4 electromagnets are connected in a feedback loop around a petri-dish containing a single droplet of ferrofluid. The camera observes the current location of the droplet; the computer computes the electromagnet actuations required to move the droplet from where it is to where it should be; and the amplifier applies the needed voltages to do so. This loop repeats at each time to steer the droplet.

I consider an initial ferrofluid control problem: the precise manipulation of a single drop of ferrofluid by four external electromagnets. Precision control is achieved by feedback: Sense the location of the droplet by a camera and imaging software and then correctly actuate the electromagnets at each time to move it from where it is to closer to where it should be (Figure 3). Repeating this magnetic correction at each time quickly forces the droplet to the desired stationary or moving target and allows me to precisely control its position over time.

Control design, the mathematical development of the algorithm that determines how to turn on the magnets to create the needed position correction at each time, is challenging. It is recognized that each magnet can only pull the fluid towards it; any single magnet cannot push a magnetic fluid [77, 78]. Mathematically, this is reflected in the quadratic dependence of the magnetic force on the applied magnetic field – reversing the magnetic field polarity does not change the created magnetic force. Further, the available pulling force drops rapidly with the ferrofluid distance from each magnet [79, 80]. This makes it difficult to move a ferrofluid droplet left when it is close to the rightmost magnet (the other three magnets must pull it from a long distance, and not over-pull it once it approaches them). The control algorithm accounts for these difficulties, both for the pulling only nature of each magnet and for the rapid drop off in magnetic force with distance, and it does so in an optimal (minimal electrical power) and smooth fashion. This is done by first finding the set, or manifold, of all electromagnet actuations that will create the desired droplet motion, and then within this manifold picking the minimum power solution.

Compared to my prior work of manipulating single [15, 81] and multiple particles [82] by electric fields and electroosmotic flows [46, 83], which can both pull and push particles, the key challenges for magnetic control of a single ferrofluid droplet are: 1) The pull only nature of the magnetic actuation. 2) The sharp drop off in magnetic force with distance from the magnet: applying a needed magnetic field when the droplet is far away can easily and dramatically over-pull the droplet as it gets slightly closer to that magnet. 3) The maximum strength constraints of the magnets which provided a hard-stop to the amount of control authority available. This makes the minimum electrical power control both reasonable and desirable. 4) The nonlinear cross-coupling between magnets (turning on two magnets at once is not the same as the sum of turning on each magnet individually). This means a control law based on single magnet actuations will have poor performance on the diagonals between magnets. My method works effectively over the entire spatial domain. 5) The related need to switch magnet actuation smoothly in time from one set of magnets to another as the ferrofluid droplet moves through its domain (my control design achieves this). And 6) the need to correct for electromagnet coil charging time delays. This is crucially important for deeper control using larger and stronger magnets that will have longer charging times.

Past work in control of magnetic particles and magnetizable objects has included magnetically assisted surgical procedures, MRI control for micro-particles and implantable magnetic robots, ferrofluid droplet levitation, magnetic tweezers, and nanoparticle magnetic drug delivery in animal and human studies. Methods to

manipulate a rigid implanted permanent magnet through the brain with a view to guiding the delivery of hyperthermia to brain tumors are presented in [84] and [85]. Here a point-wise optimization is stated for the magnetic force on the implant and example numerical solutions are shown which display jumps and singularities similar to the ones I had to overcome in this work. Based on market opportunities, the focus of this group changed to magnetically assisted cardiovascular surgical procedures and led to the company Stereotaxis (www.stereotaxis.com/). This company now uses magnetic control to guide catheters, endoscopes, and other tools with magnetic tips for precision treatment of cardiac arrhythmias and other cardiovascular interventions. Stereotaxis implant control algorithms are not disclosed in detail but are noted briefly in published patents [22-27]. Similar public domain results, with an MRI machine as the actuator, are presented by Martel et al [86-88] who also discusses manipulation of implantable magnetic robots [89-91] and magnetic guidance of swimming magnetotactic bacteria [92, 93].

In terms of feedback control of microscopic and nanoscopic magnetizable objects, in [94] a ferrofluid is levitated by feedback control of a single upright electromagnet. Here the droplet is passively attracted to the electromagnets vertical axis and active feedback is used to modulate the strength of the magnet to stabilize the drop up and down against gravity and disturbances. Two and three dimensional control of magnetic particles in microscopic devices (magnetic tweezers) is described in [36, 45, 95-99] including magnet design and feedback control methods that enable impressively precise and sensitive capabilities for manipulating magnetic microscopic

objects [100, 101]. Prior work in magnetic manipulation of therapeutic ferromagnetic nano-particles (magnetic drug delivery) has progressed to animal and human clinical trials [75, 76, 102-104]. Magnetic manipulation here is currently limited to static magnets, either held externally [105-110] or implanted [111-116] – as yet there is no active feedback control in this arena.

Compared to prior work, my research here is focused on optimal control for minimum power smooth and deep manipulation of a ferrofluid, with a view towards enabling feedback control of magnetic drug delivery to reach deeper tumors in the long term (see also [117-119]). To this end, I have developed and experimentally demonstrated a novel and sophisticated optimal control algorithm to effectively manipulate a single ferrofluid droplet by feedback control. This algorithm was explicitly designed to address the highly nonlinear and cross-coupled nature of dynamic magnetic actuation and to best exploit available electromagnetic forces.

Thesis Outline

This thesis is about theoretical and experimental challenges that I faced and solved during the course of demonstrating electrokinetic and electromagnetic manipulation of particles. In Chapter 2 I present equations governing particle motion under electroosmotic actuation, show particle steering control algorithms, particle tracking algorithms, minimum power path planning algorithms and talk about the experimental design that was used to demonstrate steering of living biological cells, swimming microbes and steering of multiple particles simultaneously. In chapter 3 I show improvements of the method toward better accuracy and demonstrate this by steering quantum dots to nanometer precision. In chapter 4 I introduce a novel method for three dimensional steering of single and multiple particles by electrokinetic actuation. The last chapter shows theoretical and experimental results for magnetic control of ferro fluids in a plane. These experimental results are a key next step towards my broader effort of precision control of magnetic drug delivery to deeper tissue targets. Several researchers have contributed to these projects. Details about the contributions are given in the final section of this chapter.

Chapter 2: Feedback Control of Particle by Micro Flows

This section describes the model of the fluid flow and particle motion in the micro fluidic device, and then shows control algorithms used to steer single and multiple particles at once. It describes the particle tracking algorithm and algorithms for creating minimum power paths. It describes experimental methods for system operation and presents experimental particle steering results.

Model of Fluid and Particle Motion

In order to create the control algorithms that steers multiple particles independently, a model is required that describes the (neutral or charged) particle motion that results from any electrode actuation. It is possible to design a control algorithm for single particle steering without reference to a model but, even in that case, a model provides valuable insight.

The microfluidic system in this thesis can actuate micro- and nano-scale objects in one of two ways. It can either move the fluid in the device by electroosmotic actuation (described next) to carry particles along, this works for both neutral and charged particles; or, if a particle is charged, then it can be actuated by an electric field which applies an electrostatic (Coulomb) force and moves the particle relative to the surrounding fluid (electrophoretic actuation) [46, 83].

Particles often acquire a surface charge through weak chemical interactions with the surrounding fluid. Thus, charged particles are the norm rather than the exception but the amount of charge can vary depending on the chemistry of the object and the surrounding medium.

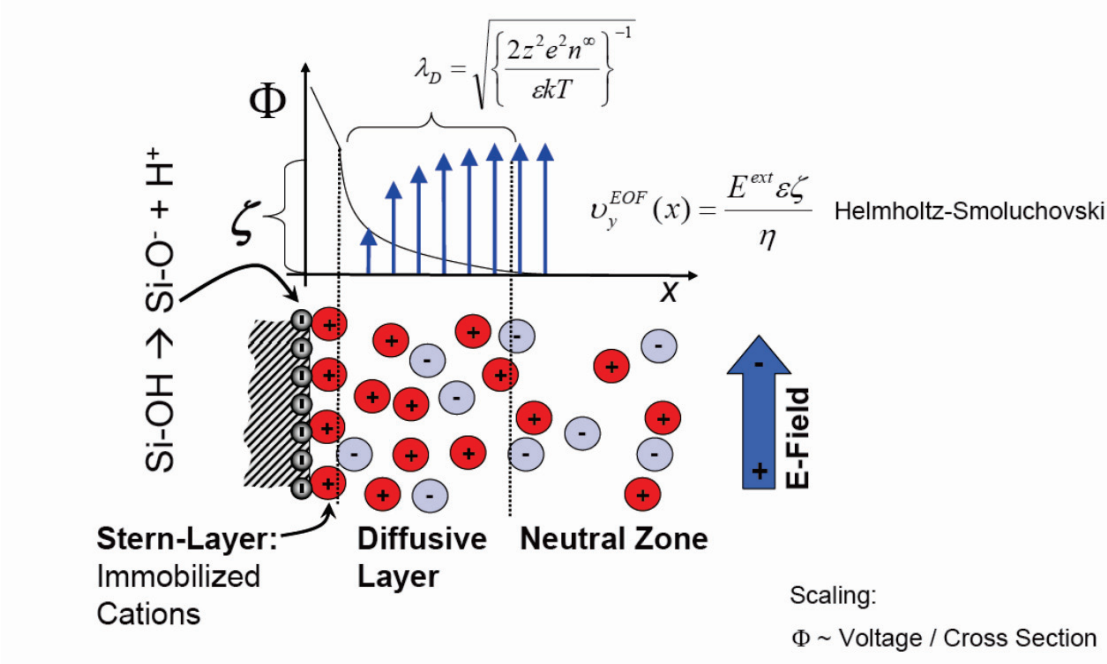

Figure 4: The physics of electroosmotic actuation. A schematic side view through a micro-fluidic channel is shown. The minus signs represent the fixed charges at the solid/liquid interface, circles (+ or -) show ions naturally found in the liquid (e.g. in water). These ions accumulate to shield the surface charges forming a thin Debye layer that has a predominant charge (here mostly positive). The electric field moves this layer and it drags the fluid in the channel by viscous forces. Charges in the interior of the channel remain essentially balanced (only a small fraction of the charge goes to the surfaces) and so they create no net fluid motion effect. (Figure reused with permission from Dr. Friedrich Schoenfeld, Germany.)

Electroosmotic actuation of flow is routine in micro-fluidic devices, e.g. [120-122]. Here an applied electric field electrophoretically moves a thin layer of charges that form naturally at the fluid/device interface. Typically, these charges are ions present in the liquid that migrate to the solid/liquid boundary to shield stationary charges

formed there, for example, by weak acid/base chemistry occurring at the interface (the same type of chemical mechanisms also lead to charge formation on the surfaces of particles). Which charges (positive or negative) and how much they accumulate inside the liquid immediately adjacent to the device surfaces depends on the chemistry of the liquid and solid materials, on the pH, the amount and type of dissolved ions, surface treatments, and many other factors. The electric field applied by the electrodes moves these free charges (the Debye layer) in one predominant direction. This thin moving layer of charges then drags the rest of the fluid along by viscous forces, the electroosmotic actuation. (Charges in the interior of the fluid do not cause a net fluid motion. Since there is essentially an equal number of positive and negative ions (only a small fraction of ions of one type are taken away into the Debye layer) the interior charges create an equal and opposite electrical forces on the fluid in the channel center, their only net effect is to move through the fluid and heat it.) A more detailed description and analysis of the physics of electroosmotic actuation can be found in [46, 83]

In electroosmotic flow the fluid is dragged by moving charges that are actuated by the applied electric field. In a planar devices this means that the flow will follow the electric field that is active at the floor and ceiling of the device. The electric field I apply is uniform in the vertical direction but it can have complex patterns in the horizontal (x,y) plane. The resulting micro-flow will exhibit these same complex horizontal patterns. It is possible to show this rigorously starting from the Navier Stokes equations, as in [123], the end result is that the fluid velocity follows the

applied electric field essentially instantaneously (with a micro-second time constant) Thus, see also [83],

$$\vec{V}(x,y,z,t) = (\varepsilon\xi/\eta)\vec{E}(x,y,t) = -(\varepsilon\xi/\eta)\nabla\varphi(x,y,t) \quad (1)$$

where $\vec{V}$ is the electroosmotic fluid velocity, $\vec{E}$ is the applied electric field which is uniform in the vertical direction, ϕ is the electric potential as created by the actuators, ε is the permittivity of the liquid, η is its dynamic viscosity, and ξ is the zeta potential (essentially the voltage) at the liquid/solid interface [46, 83]. Electric fields are governed by Laplace's equation, the electrostatic limit of Maxwell's equations [124], with boundary conditions at the electrodes set by the voltages that I apply there.

In the above it is ξ which quantifies the amount of charge that is contained in the Debye layer. Since this value depends on the details of the surface chemistry and cannot be predicted *a-priori*, it is usually inferred from experiments by applying a known electric field and measuring the resulting flow velocity. The chemistry that happens at the solid/liquid interface is complicated and so the above discussion of electroosmotic actuation should be understood as a first order simplified explanation. The underlying chemical principles of electroosmosis are still not well understood, however, that does not prevent me from using it to precisely control microscopic and nanoscopic particles as I show in the remainder of this chapter.

Neutral particles are carried along by the created electroosmotic flow. In addition, these particles experience Brownian motion. When the particles are comparable in size to the channel height, as for example the yeast cells that are ~ 5 μm in diameter compared to the 11 μm high channels I used in [82], the particles bounce and bob inside the channels. When the particles are small, e.g. the nanoscopic quantum dots, then they diffuse in all three directions. In either case, I only control their motion in the xy plane leaving their motion to be free in the z direction.

Thus, in the plane, the particle positions are governed by $\dot{\vec{P}}_j = \vec{V}(\vec{P}_j) + \vec{w}$ where $\vec{w}$ is Brownian noise and $\vec{P}$ is the vector of particle x and y positions. The electric potential is described by Laplace's equation $\nabla^2\phi = 0$ with Dirichlet boundary conditions at the electrode boundaries $\phi(\partial D_j) = u_j$ where ∂D_j denotes the liquid/electrode interface location and u_j is the jth applied voltage. Insulating Neumann conditions hold at other surfaces. The solution of Laplace's equation is linear in the applied voltages so

$$\dot{\vec{P}} = \vec{V}(\vec{P}) + \vec{w} = c\vec{E}(\vec{P}) + \vec{w} = -c\nabla\varphi(\vec{P}) + \vec{w} = -c\sum_{j=1}^{n} \nabla\varphi_j(\vec{P})u_j + \vec{w} \qquad (2)$$

where $c = \varepsilon\xi/\eta$ is the electroosmotic mobility, φ_j is the solution to Laplace's equation when electrode j has a unit applied voltage and all other electrodes are at zero voltage, and $\vec{u}$ is the time-varying vector of applied voltages. Note that the

velocities of the particles is in the direction of the locally applied electric field and so depends on where they are with respect to the electric potential $\phi(x,y)$. For the same set of voltages, two different particles in two different locations can be actuated in different directions. In summary, the equations to be controlled for *m* neutral particles are linear in the control and nonlinear in the particle positions, they are

$$\dot{\vec{r}} = A(\vec{r})\vec{u} + \vec{w} \tag{3}$$

where $\vec{r} = (x_1, y_1, x_2, y_2, \ldots, x_m, y_m)$ is the position vector for the planar location of the *m* particles of interest and the *A* matrix contains spatial information about the electric fields originating from each electrode.

If the particles are charged then there is an added electrostatic force that also points with the electric field – either along it for a positively charged particle or directly opposite it for a negatively charged particle. This can be incorporated into the *A* matrix by modifying the mobility coefficient for each particle. Variations in the electroosmotic zeta potential and the amount of charge on the particles can change these mobility coefficients, but the control algorithm is robust to these variations – the control basically sets the direction of particle motion at the location of each particle, so long as the sign of the mobility coefficient for that particle does not flip (a rare occurrence) the control works. To further improve performance, I usually identify the mobilities of the particles of interest before starting an experiment by applying a known electric field and observing their resulting velocity through the vision system.

My particle steering experiments in [82] function to 1 μm precision even though the polystyrene particle and cell mobilities in that case are only known to within ±50%. The quantum dot experiments show 57 nm accuracy even though the charge on the QD also varies.

Particle Steering Control Algorithms

Figure 1 shows the basic control idea for a single particle: a 4-channel micro-fluidic device, an optical observation system, and a computer with a control algorithm, are connected in a feedback loop. The vision system locates the position of the particle in real time, the computer then compares the current position of the particle with the desired (preprogrammed or user input) particle position, the control algorithm computes the necessary actuator voltages that will create the electric field, or the fluid flow, that will carry the particle from where it is to where it should be, and these voltages are applied at electrodes in the micro-fluidic device. For example, if the particle is currently South/East of its desired location, then a North/West flow is created. The process repeats at each time instant and forces the particle to follow the desired path.

It is also possible to steer multiple particles independently using micro flow control [125]. A multi-electrode device is able to actuate multiple fluid flow or electric field modes. Different modes cause particles in different locations to move in different directions. By judiciously combining these modes, it is possible to move all the particles in the desired directions. I note here that this kind of flow control, where I

control the fluid so precisely that I can hold or steer multiple objects at once in different locations, is not possible in macro-scale fluid dynamics. Here I am exploiting the linear nature of the electrostatic equations and Stokes flow (the nonlinear fluid momentum terms, the 'Navier' part, are negligible on the micro-scale) to be able to invert the problem to achieve control. I certainly would not be able to invert a high Reynolds number or turbulent flow in the same fashion since it would amplify small changes in actuation to large errors in particle motion.

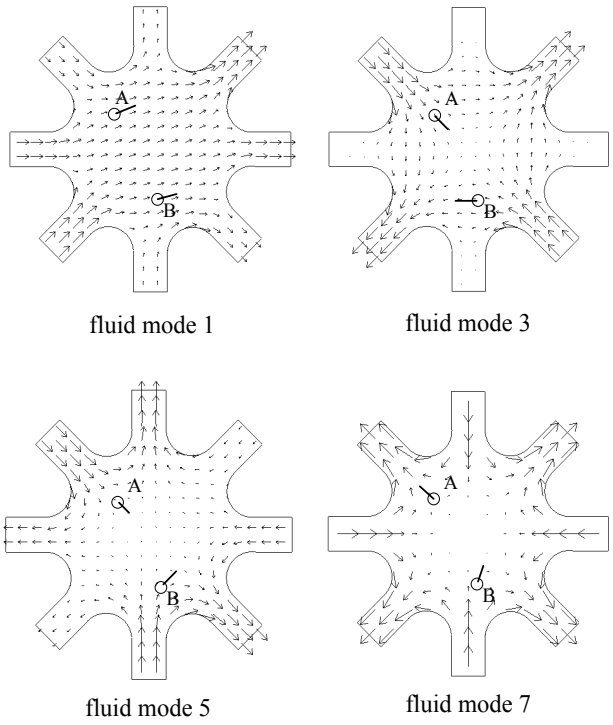

Figure 5: Electroosmotic micro-flow modes for an 8-electrode device. The above figure shows the 1st, 3rd, 5th, and 7th modes computed from the model stated above (also see [82, 125]). The two example neutral particles A and B (shown as black dots above) will then experience the velocities shown by the arrows. (Figure repeated with permission from [82].)

The control algorithm relies on inversion of the flow and electric fields predicted by the model. An eight-electrode device, as in Figure 5, can create 8 independent electric/fluid modes (one of the 8 modes has negligible influence so only 7 degrees of freedom remain). Four of these seven modes are shown above. The key point is that the different modes force particles at different locations in different directions (see particles A and B in Figure 5): by intelligently actuating a combination of modes, I can force all the particles towards the right locations at each instant in time. Since each particle has two degrees of freedom (an x and a y position), an eight-electrode device can precisely control up to 3 particles (particle degrees of freedom 3 x 2 = 6 ≤ 7 actuation degrees of freedom).

In its simplest incarnation, the control algorithm works as follows (details in [125]). I define a desired correction velocity vector between where all the particles of interest are observed to be versus where I would like them to be at the current time

$$\dot{\vec{r}}_{correction} = g(\vec{r}_{desired} - \vec{r}_{observed}) \tag{4}$$

here g is the control gain. The task is now to choose the voltages at the electrodes to create a velocity as close to this desired correction velocity as possible. Since there is a linear relation between the control and the velocity (I know the particle positions since the camera can see them), and since this velocity is achieved essentially instantaneously as soon as I apply the voltages, I can solve a static linear problem to determine the needed set of electrode voltages. Specifically, I solve a least squares

problem to find the set of actuator voltages that will create velocities at all the particles of interest as close as possible to the desired correction velocities. The other particles (the particles not of interest) are actuated in some random way that depends on the electric fields they will see at their locations. This gives the feedback control

$$\begin{aligned} \vec{u}^{*} &= \left[A^{T}(\vec{r})A(\vec{r}) \right]^{-1} A^{T}(\vec{r})\dot{\vec{r}}_{correction} \\ &= k\left[A^{T}(\vec{r})A(\vec{r}) \right]^{-1} A^{T}(\vec{r})\left(\vec{r}_{desired} - \vec{r}_{observed} \right) \end{aligned} \tag{5}$$

For the case where there are more actuation than particle degrees of freedom ($n\text{-}1 \geq 2m$) the A matrix typically has full row rank (unless two particles are at the same location) and the above least squares answer achieves the desired velocity with minimum control effort (with minimum $\left\| \vec{u} \right\|_2$) [126]. For cases where I try to control more particle degrees of freedom than I have actuators, the experimental performance rapidly degrades to unusable. For example, 4 particles (8 degrees of freedom) can be controlled badly by 8 electrodes (7 degrees of freedom), but 5 particles cannot. Since it is possible to fabricate devices with many electrodes, the real limit to the number of particles that can be controlled is the condition number of the matrix A as discussed below.

I pre-compute the electric fields that make up the matrix A ahead of time; this means I can use a lookup table to determine A for any particle positions $\vec{P}$ seen by the camera. I then compute the pseudo-inverse $(A^{T}A)^{-1}A^{T}$ in real time, in milliseconds, as the control proceeds.

(Note: A^T is known as the pseudo inverse of matrix A [29]. The pseudo inverse of a matrix is a more general form of the commonly known "inverse" for a matrix. A linear system of equations y = Ax where A is full rank, has infinitely many solutions if A is fat, has one solution if A is square, and has no solution if A is thin. $A^T y$ gives the least norm solution to the linear equation if B is fat, gives the unique solution if B is square (here A^T reduces to A^{-1}), and gives the least-squares solution if A is thin).

It is convenient to carry out this calculation in the coordinate system of the fluid modes of Figure 5 (the singular values modes of the matrix A evaluated on a fine grid of points). The dominant (lower spatial frequency) modes are the ones that are better conditioned: at the higher spatial modes very high voltages are required to create small fluid velocities leading to poor conditioning. Thus I truncate the matrix A onto these first modes and compute the pseudo inverse above for that well conditioned matrix. It is in fact this conditioning that sets how many particles I can control at once. For the experimental image sensing and actuation errors I can robustly access just over the first ten or so modes which means I have been able to control up to 5 particle simultaneously in experiments. There are also other issues, such as a limit to the voltage that can be applied at the electrodes (too high a voltage causes electrolysis[127] a chemical reaction that creates bubbles, and must be avoided).

The control works robustly across the entire control region – so long as I have done the singular value mode conditioning above there are no regions or combinations of

particle locations where I cannot reliably pseudo-invert A. The only time the inversion fails is if two particles are right on top of each other but I am trying to move them in different directions (this is physically impossible since I have to create two different fluid flow directions at the same location).

Minimum Power Path Planning Algorithms

The number of controllable particles and the proximity of individual particles to each other is limited by actuation constraints. There is a limit to the voltage that can be applied at the electrodes (too high a voltage causes electrolysis a chemical reaction that creates (reactive ions, ph change etc) bubbles, and must be avoided). I have treated this actuation limit in two ways: (1) by turning down the control gain per particle as I approach this limit, (2) more rigorously, by phrasing a constrained optimization problem to calculate optimal paths that minimize the actuation effort when steering multiple particles. Path planning algorithms can be used to calculate trajectories for multiple particles even in the presents of constrains and uncertainties.

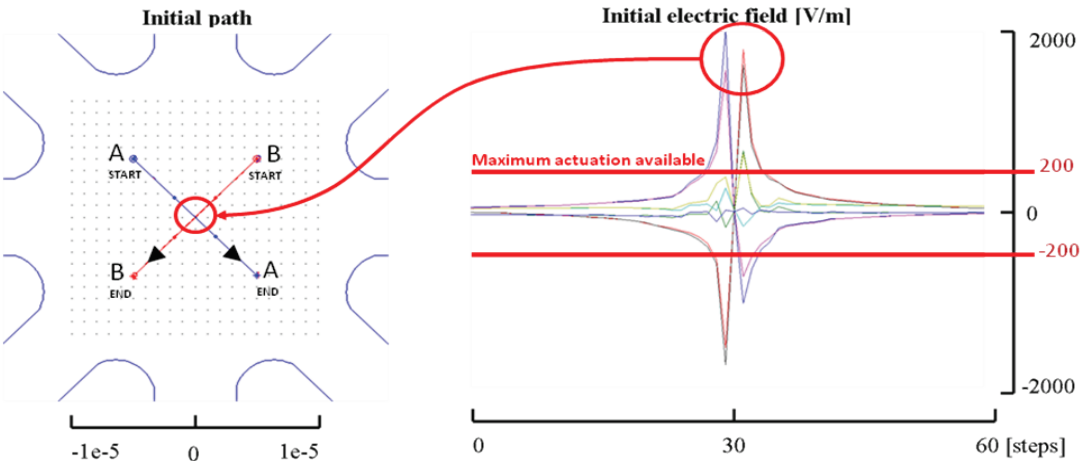

Figure 6: This figure illustrates a scenario in which particles come close to each other. The voltages needed to steer particles are shown on the right side. The horizontal lines in the graph are the maximum and minimum available voltage.

Path planning is the method for finding trajectories for a desired movement from an initial state to a final state. Here I present two methods for generating (numerically) minimum power paths. The first method is based on direct search techniques used in parametric design optimization problems [128]. The second method is based combinatorial search techniques (exhaustive enumeration) often used for the purpose of path planning in robotics[129]. The goal is to use these two methods to approximate the theoretical global optimal trajectory and to deliver fast results which are feasible for real–time implementation.

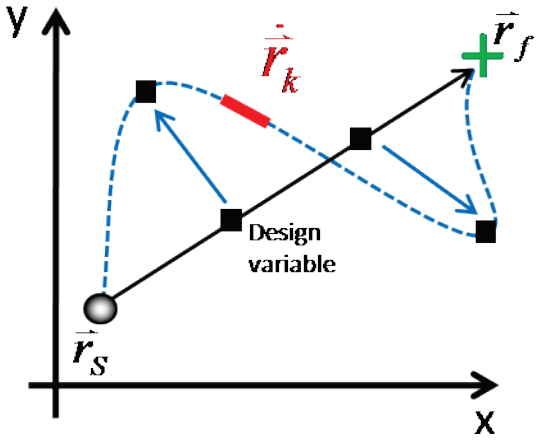

Figure 7: This figure illustrates the path representation as a parametric curve. The straight line represents the initial path and the dashed curved line represents the optimized path. Black squares represent the design variables which are changed dynamically by the optimization method in an effort to minimize the total cost of the path.

For the purpose of calculating optimal trajectories subject to actuation constrains for multiple particle steering I use a standard design optimization method. In general, a trajectory can be defined by two points in a plane. Between these two defining points, it is the job of the optimization method to determine the optimal trajectory. The trajectory for the particles consists of two categories of design parameters. Two fixed points in space define the initial and the final position of the particle and a set of free

points define waypoints the particle has to pass on its way to its final position (the end of the path). The full trajectory is represented by a spline function which connects all points on the path. The cost associated with the path is the total energy it takes to move the particle along the path.

In order to solve the trajectory planning problem numerically, I discretize the equations I found for the control law earlier in this chapter

$$u_k = A(\vec{r}_k)\dot{\vec{r}}_k \tag{6}$$

Here $\dot{\vec{r}}$ is the particle velocity for one path segment and u is the voltage needed to move a particle on this path segment.

Position constrains on $\vec{r}$ can be expressed as

$$\begin{aligned} &\vec{r}_{\min} \le \vec{r}_k \le \vec{r}_{\max} \\ &\vec{r}_0 = \vec{r}_0 \\ &\vec{r}_F = \vec{r}_F \end{aligned} \tag{7}$$

Voltage constrains on $u = [u_1, ..., u_n]'$ can be expressed as

$$\vec{u}_{\min} \le \vec{u}_k \le \vec{u}_{\max} \tag{8}$$

For a solution that is both energy and time optimal, the objective function is defined as

$$J(r) = \sum_{k=0}^{N-1} R\left\|\vec{u}_k\right\| + \sum_{k=0}^{N-1} Q\left\|\vec{r}_k - \vec{r}_F\right\| \tag{9}$$

where R and Q are positive weight factors. The first term represents the energy cost and the second term represents the arrival cost which is the key to a minimum time conditioning of the cost function.

A set of calculated optimal trajectories for two and three particles is shown in Figure 8 and Figure 9 respectively. A collision of the particles has been avoided and the amplitude of the applied voltages has been reduced by a factor of 10 for two particles and by a factor of 5 for three particles.

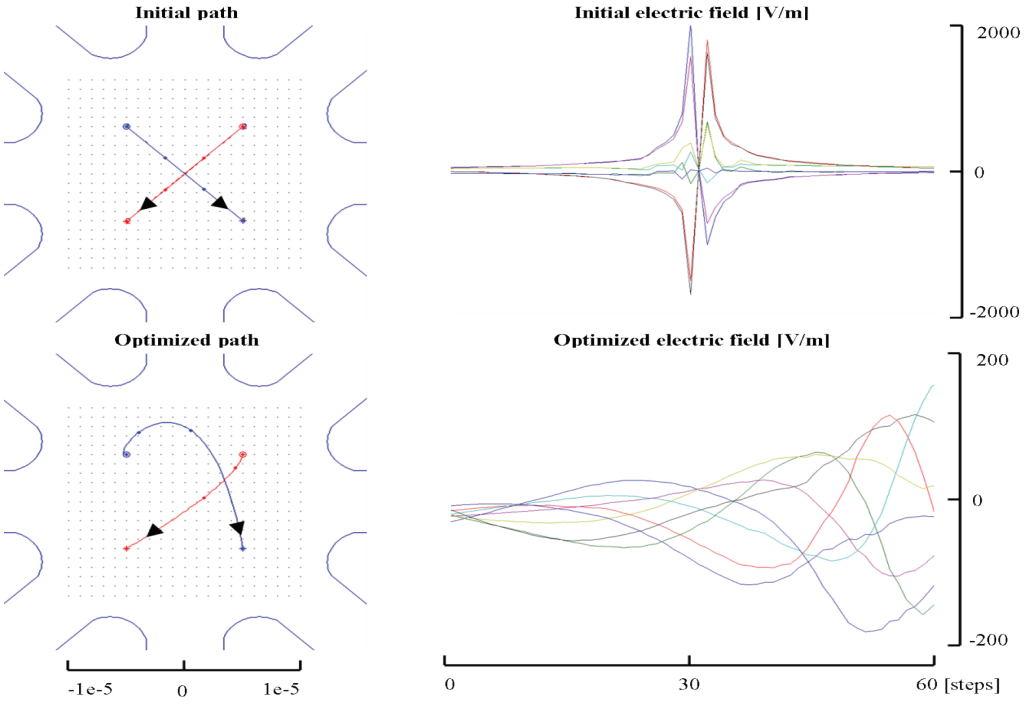

Figure 8: This figure shows the initial paths and the required voltages for steering two particles on crossing paths. The bottom of the figure shows the power optimal paths and the reduced voltages.

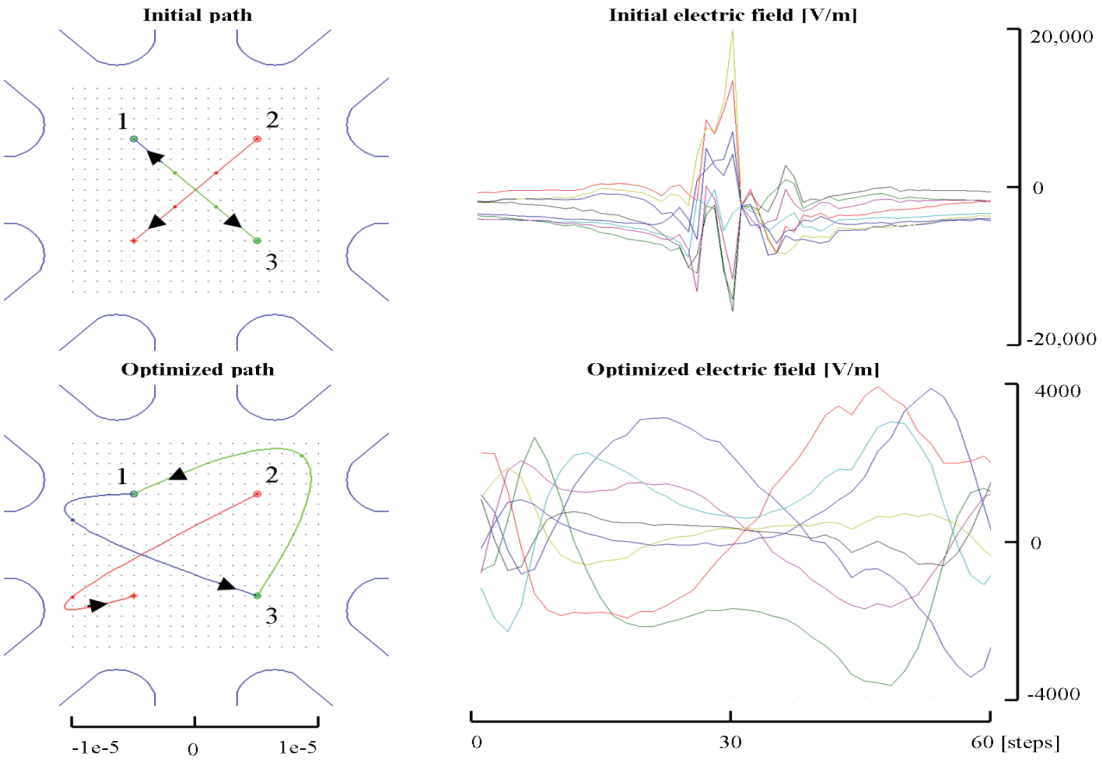

Figure 9: This figure shows the initial paths and the required voltages for steering three particles on crossing paths. The bottom of the figure shows the power optimal paths and the reduced voltages.

Due to the nonlinearity of the problem the search method described here will often reach local minima which are not necessarily the global optimal minima of the theoretical optimal trajectory. Unfortunately, the nonlinearity of the problem worsens when more particles are involved in the control. Other methods, such as genetic algorithms can deliver better solutions but these methods still have the potential to be trapped in local minima.

Discrete optimization methods do not have this limitations but this comes at the cost of higher computational efforts. In the next section I describe how a discrete optimizations method, also known as branch and bound method can be used to find global optimal paths.

In general, discrete optimization techniques can be categorized into three techniques: (a) exhaustive enumeration, (b) branch and bound method (BB) and (c) dynamic programming (DP). Exhaustive enumeration method explores all possible path combinations. Here I use the branch and bound method to calculate optimal trajectories for multiple particles. BB is based on partial enumeration where only parts of all possible path combination are explored to save computational resources. The third method, dynamic programming, offers an elegant way to find optimal solutions but requires more computational resources for higher dimensional problems.

Let's take a look how the branch and bound method can be used to generate optimal paths. Consider a rectangular grid of points (nodes) and two particles that are placed on this grid (Figure 10). Each particle can move from its current node to an adjacent node. The motion is restricted to free nodes only, meaning that particles cannot move to nodes that are occupied, i.e. by another particle.

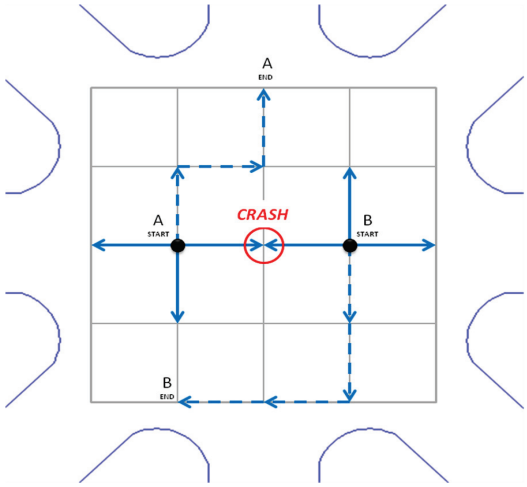

Figure 10: This figure represents the grid for multi-particle paths. Each particle is at one of the vertices of the grid and the motion of the particles is constrained along the grid. As an example the path of two particles is shown here. Collision of the two particles is restricted by not allowing them to share the same space at the same time.

A possible solution path is defined by a series of adjacent nodes $\{\vec{r}_0,...,\vec{r}_F\}$, where r_0 is the initial position and $\vec{r}_F$ is the final position the particle reaches after travelling on the solution path.

The optimization criterion can be stated such as finding the lowest cost path

$$J = \min \sum_{k=0}^{N-1} J_k(\vec{r}_k, \vec{r}_{k+1}) \tag{10}$$

where J represents the cost for the entire path and $J_k(\vec{r}_k, \vec{r}_{k+1})$ represents the cost for a single path segment, in other words the cost moving from r_k to r_{k+1}.

The branch and bound search algorithm expands possible paths from the start to the end. The expansion process for two particles is illustrated in Figure 11. Here, particles are allowed to move in four directions (East, West, South, North) or stand still.

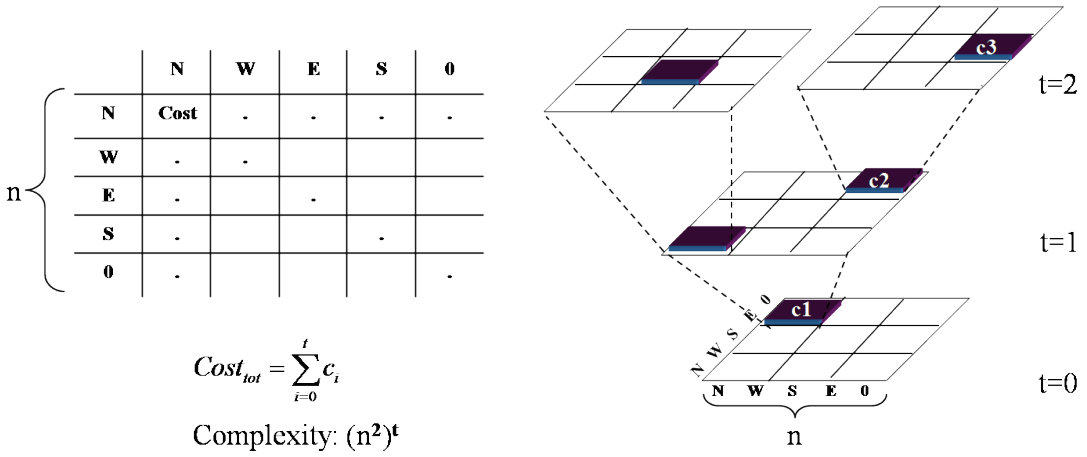

Figure 11: This figure illustrates the method for obtaining all possible paths for two particles moving three steps ahead. The possible combinations of the motion for one step are shown on the left. The branch and bound method for a three step path is illustrated on the right. The cost of a path is the sum of the individual costs of that path. The algorithm searches the lowest all final nodes (here at t=2) for the lowest cost. The lowest cost node defines the end node for the power optimal paths.

The path with the lowest cost is the (numerically) optimal path. However, if particles can only move to adjacent nodes the path will consist only of movements of multiples of 45deg, 90deg. This is a drawback for finding paths that are close to the theoretical optimal paths. Better solution paths can be achieved when particles are allowed to move on a finer range as is shown in Figure 12.

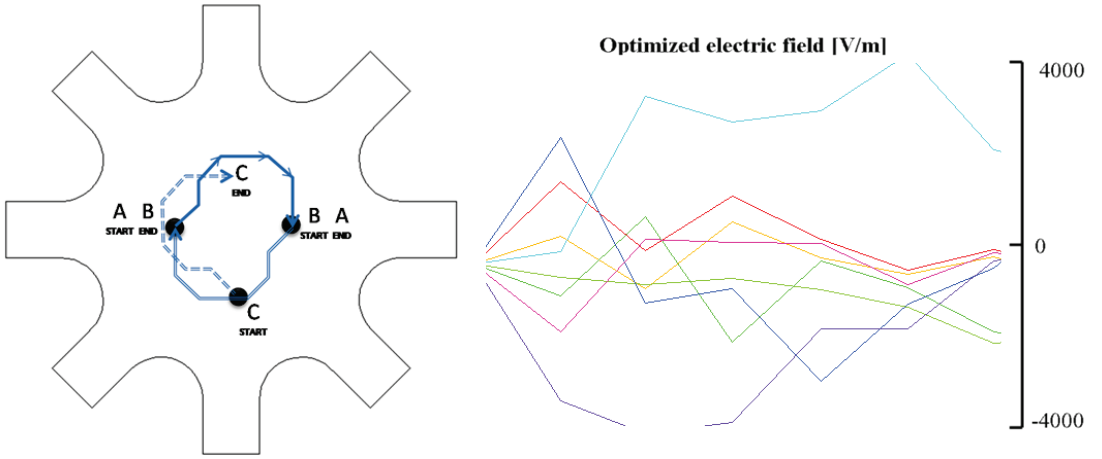

Figure 12: This figure show the power optimal path for three particles computed using the branch and bound method. The initial and final positions of the particles (A, B, C) are depicted by the subscripts 'start' and 'end'. The path for each individual particle is illustrated by solid, double and dashed lines.

The limitations of this approach can be summarized in two major points. First, optimality is restricted due to discretization and second, the solution can become computational expansive for big optimization problems.

Due to the grid structure, paths are found that are more expansive than the theoretical optimal path. Even though the density of the grid can be increased to achieve a better approximation, the search space increases accordingly and makes the search slow and requires lots of memory.

To reduce the computational effort, for both methods mentioned, it is necessary to reduce the problem size. One way to do this is to use a receding horizon frame work. Instead of calculating the complete optimal trajectory (from $\vec{r}_0$ to $\vec{r}_F$) it is possible to break the problem down to sub problems of smaller size with less time steps N. Now, a problem where $\vec{r}_0$ and $\vec{r}_F$ are located far from each other can now be solved piece

wise with fewer steps in each sub problem. The first sub problem starts at $\vec{r}_0$ and only N time steps of the path are calculated into the future. Then, the last step from the first sub problem is used as the initial state of the second problem and so on until the desired destination $\vec{r}_F$ is reached.

Since each sub problem is open ended, meaning that the sub problem doesn't reach the destination, I need to add an additional term to the objective function to motivate each sub problem and eventually the overall path to get closer to the final destination over time. An additional cost, the terminal cost with weight factor P, enters the objective function

$$J = \sum_{k=0}^{N-1} R\left\|\vec{u}_k\right\| + \sum_{k=0}^{N-1} Q\left\|\vec{r}_k - \vec{r}_F\right\| + P\left\|\vec{r}_N - \vec{r}_F\right\| \tag{11}$$

Particle Tracking Algorithm

To control particles by visual feedback control it is essential to have a system that can visually track particles. Particle tracking is a method that follows the motion of individual particles in subsequent images. The algorithm follows two simple steps:

(a) Particle identification

(b) Particle tracking

Several particle identification methods are available today. Two major ones are centroiding (calculating the center of mass) and Gaussian fit. Both algorithms achieve nm accuracy in low noise environments. The overall precision of both algorithms depends mainly on the shape of the particle and the noise and resolution of the imaging system.

Most particle tracking algorithms use cross correlation of subsequent images. The cross correlation methods determine the change in particle position by comparing an image to a subsequent image. The correlation fails if the two images do not have any similarity or in other words, if the particles moved to far between frames; this is the case when the camera is operated at slow frame rates.

I use a method that is capable of tracking individual and multiple particles regardless of how fast the camera acquires images. The system is based on the well known Kalman filter (predictive filter) [130]. For my purposes the Kalman filter predicts the

future position of the particles based on the particle dynamics and past measurements which are incorporated into the position estimation. The Kalman filter does not identify the particle but can aid to the identification step by predicting where the particle will be in the next image frame. A centroiding or Gaussian fit algorithm identifies the particles in the neighborhood of the predicted region. The particle that is closest to the predicted position is marked as the particle of interest. With this method it is possible to track individual particles through a cloud of particles.

The Kalman filter was first published in 1960 and has been used for control and prediction of dynamic systems. When controlling a system, a Kalman filter can provide valuable information that cannot be directly measured by estimating the values of the state from indirect and noisy measurements. It provides a discrete optimal solution, mainly for linear systems, to calculate an a priori and a posteriori prediction.

System and Measurement Model for Particle Tracking

The Kalman filter is used to predict the object locations in subsequent frames based on the particle location determined by the particle identification algorithm. For this, it is important to choose accurate system and measurement models. This includes a state vector and a state transition matrix which represent the system dynamics and a measurement vector and its relation to the system state which describes how the states of the system are measured.

The motion of the particles can be modeled according to the kinematic model of an accelerated object, i.e. a particle subject to a non uniform electric field. In the simplest case (1D), this system can be described with three state variables: position, velocity and acceleration

$$\begin{aligned} \textit{Position}: &\quad x_{k+1} = x_k + h\dot{x}_k + \frac{1}{2}h^2\ddot{x}_k \\ \textit{Velocity}: &\quad \dot{x}_{k+1} = \dot{x}_k + h\ddot{x}_k \\ \textit{Acceleration}: &\quad \ddot{x}_{k+1} = \ddot{x}_k \end{aligned} \tag{12}$$

where the parameter h correspond to the time interval and k is the time index. To use equations (12) , new variables are introduced to transform the governing higher order ODEs into coupled sets of first order differential equations

$$\begin{bmatrix} x_{k+1}[1] \\ x_{k+1}[2] \\ x_{k+1}[3] \end{bmatrix} = \begin{bmatrix} 1 & h & \frac{h^2}{2} \\ 0 & 1 & h \\ 0 & 0 & 1 \end{bmatrix} \cdot \begin{bmatrix} x_k[1] \\ x_k[2] \\ x_k[3] \end{bmatrix} \tag{13}$$

The measurement equation, which provides information for the position of the particles, is given by

$$z_k = \begin{bmatrix} 1 & 0 & 0 \end{bmatrix} \cdot \begin{bmatrix} x_k[1] \\ x_k[2] \\ x_k[3] \end{bmatrix} \tag{14}$$

From the two equations above I get the transition and measurement sensitivity matrices

$$\Phi = \begin{bmatrix} 1 & h & \frac{h^2}{2} \\ 0 & 1 & h \\ 0 & 0 & 1 \end{bmatrix} \quad and \quad H = \begin{bmatrix} 1 & 0 & 0 \end{bmatrix} \tag{15}$$

In the general case, the components of the state vector are uncorrelated which allows me to describe the covariance matrix Q with a diagonal matrix,

$$Q = \begin{bmatrix} q_{11} & 0 & 0 \\ 0 & q_{22} & 0 \\ 0 & 0 & q_{33} \end{bmatrix} \tag{16}$$

Q contributes to the overall uncertainty of the estimate based on the level of the model and input noise covariance.

The measurement covariance matrix R is a scalar in the 1D case and its value is set to a few pixels as this is sufficient representation of the noise coming from the vision setup I use. R is a reference of how much to trust the measurements. A high R indicates that the measurement isn't very accurate. When R is smaller the Kalman filter output will follow the measurements more closely and accept more information from them

Object tracking in image frames is at least two-dimensional but can be higher dimensional as well. For instance tracking a particle in three dimensions as it moves away or towards the observing position adds at least one additional dimension. The additional dimension can be the size of the particle as it changes when the particle moves out of focus. The time interval *h* is set to 1 because all calculations have equal timing. Predictions in the 'far' future can be done by setting *h* greater than one.

For linear system and measurement models with additive Gaussian noise the Kalman filter is an optimal solution in that it provides, at every time k, an estimation based on all previous measurements, so that the expected value of the weighted error is minimal. The Kalman filter is a recursive process. At every time k, the same operations are executed, based only on the results of the previous time step. Therefore, the computation complexity remains the same for every step, which is an important property for real time applications.

Particle Identification Algorithm

I chose the centroiding algorithm for particle identification. The centroiding algorithm finds the center of mass of the particles in the region of interest (ROI). The ROI contains both, the particle and the background, and is a matrix of intensities *I*. In the simplest case the algorithm is given by

$$P_x = \sum_{i=1}^{n}\sum_{j=1}^{m}(x_i I_{ij}) / \sum_{i=1}^{n}\sum_{j=1}^{m} I_{ij} \qquad (17)$$

Where x is the coordinate of a pixel on the x-axis, and I_{ij} is the intensity of that pixel. P_x is the resulting center of the particle on the x-axis. P_y is calculated the same way. Both coordinates are then sent to the Kalman filter.

The background noise in the image contributes to the error in the measurement and biases the centroid position to the center of the image. To get rid of the background noise it is necessary to set a threshold. A threshold is a value that a pixel has to exceed to be counted to the image. Values below the threshold level are set to zero and values above are either unchanged or set to 1 (or the highest value of the pixel).
If the threshold is too low, much of the noise stays in the image. If the level is too high, the particle is not represented well enough so that it can be identified. Because the environment is not known a fixed threshold doesn't deliver satisfying results. Therefore, I have used dynamic threshold to determine the right threshold level for each frame based on the histogram of the current image.

The Kalman filter does not detect the particles in the image, but it can support any particle detection algorithm. A combination with a process that finds objects in image frames can provides the base for a good tracking algorithm. The iteration for a frame is based on two steps:

1. Based on the predicted position, find the particle in the tracking window in the current frame.
2. Provide the measured position to the Kalman filter to estimated the current state and calculate a prediction for the next frame.

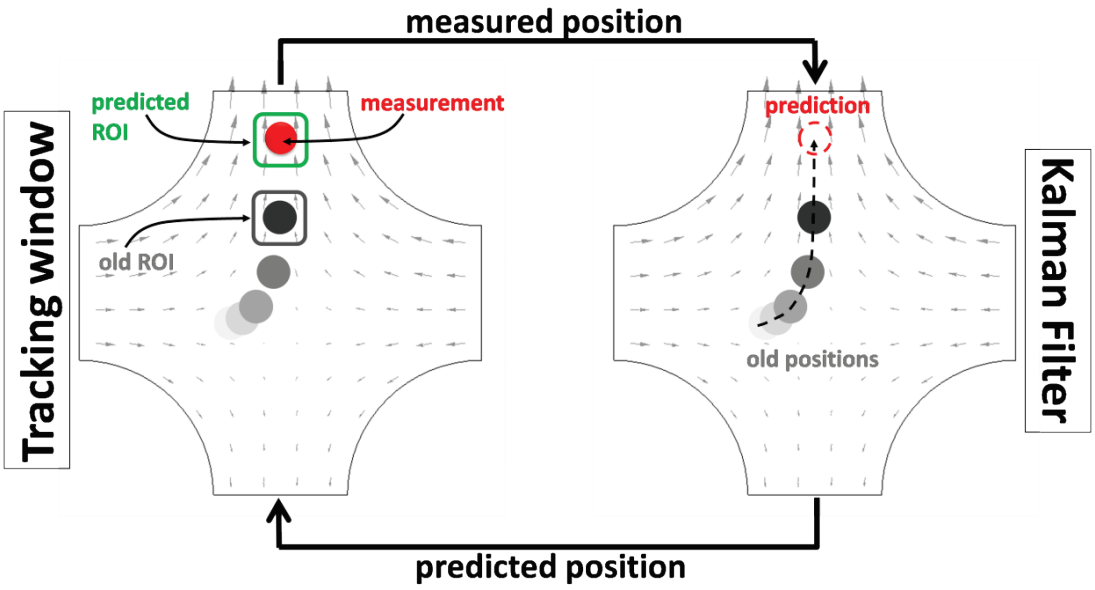

Figure 13: This figure illustrates the combination of the particle identification method with the Kalman filter.

Experiments showed that in many situations, especially at low frame rates, the Kalman tracker yields better results as if only using simple tracking algorithms. Kalman prediction allows particles to accelerate. In situations, where two tracked objects overlap, the Kalman tracker is able to resolve the indistinctness by predicting the objects positions in the next frame, resulting in a more robust tracking.

Tracking Multiple Particles

Tracking more than one particle requires more consideration. How can individual particles, with similar features, be detected and tracked in an image sequence? How can they be tracked if they are not visible for a short moment? What has to be done when one particle occludes another? What if two particles share the same path? What if they split from this path again into separate paths?

When tracking an individual particle that moves through a cluster of multiple particles with the same features, the tracker has to decide with particle is the particle that was tracked in the previous frames. To find the particle of interest in every image frame, the algorithm chooses the particle that is closest to the predicted position. This allows tracking the same particle, even if more than one particle appears in the ROI.

Multiple particles can occlude each other and consequently share the same space. This would lead to wrong detection in conventional image processing algorithms.

During the occlusion only one object would be detected instead of two. This occlusion problem is solved by assigning individual tracker to each particle.

Once an object is detected, the Kalman tracker will follow it from frame to frame. However, there are several situations, in which the algorithm will fail to keep track. If nothing is done to detect such situations, it may result in an undesired behaviour. Therefore, in different situations each tracker is put in one of the following modes: 'tracking', 'lost' or 'occluded'. Initially, all tracker start in the mode '*lost*'. A tracker is put into tracking state to follow a particle. During tracking, several situations may occur in which tracking is aborted or the tracker is put into one of the other states.

If there are no local maxima near, the tracker will follow random maxima that are caused by noise in the image. Characteristically, this results in a jumping behaviour of the tracker, which is a behaviour that particles in fluids would not have. This behaviour is detected by monitoring the velocity of the tracked particle and compares it to a velocity threshold level. The tracker is put into 'lost' mode if the velocity exceeds the velocity threshold level.

If the particle is moving and is lost because of bad circumstances, e.g. when it passes an area with similar grey distribution, then the particle identification fails. However, due to the Kalman filter it is still possible to get predictions for the objects position in a few subsequent frames. Tracking is not aborted, and the tracker is put into a '*blind tracking*' mode and the predicted position is used as the measurement for updating

the Kalman filter. If the object can be found again during blind tracking, the tracker is put back into '*tracking*' mode. Otherwise, blind tracking is stopped after a certain number of frames and the tracker is put into the '*lost*' mode.

Experimental Design and Methods

This section describes the materials used in the experiment, the actuation method, and the vision system that is used to track the particles in real time.

System Setup

The basic system to manipulate micro- and nano-scale objects by flow or electrical control consists of a micro-fluidic device, a microscope and a camera to observe the location of objects inside the device in real time, actuating electrodes powered by a digital to analog converter, and a control algorithm on a standard personal computer. The micro-fluidic device is made out of a soft polymer (polydimethylsiloxane (PDMS)) and is fast and easy to fabricate. It can be laid on top of other devices, e.g. on top of a glass device with patterned chemical features, on top of a silicon device with other MEMS capabilities, or on top of a photonic crystal for the quantum dot placement project. Details on system setup are given in [82] and [131] with the latter providing a step-by-step protocol, and a web link to the control and vision software, to allow any other laboratory to reproduce my single particle manipulation capabilities. More advanced capabilities, to manipulate swimming cells, to steer and

trap multiple particles at once, and to place single quantum dots to nanometer precision on chip are described in [82, 132, 133].

NOTE: The experimental setup can be reasonably altered if necessary (e.g. different microscope, camera, DAC etc.)

Figure 14 shows a schematic of the experimental setup. It consists of three main components: a microfluidic device, a control and actuation system to create the desired flow fields, and a vision system to locate the cells. The microfluidic device is placed on the inverted microscope (Nikon Eclipse TS100). Here conventional transmitted light illumination is used to view the cells and a CCD camera (Guppy F-033B) is used to capture images from the microscope. Other imaging modalities, such as fluorescence imaging, are also possible. Actuating platinum electrodes are held in place by removable adhesive putty (UHU tac). These are placed in each of the macroscopic reservoirs and connected to a digital-to-analog converter (DAC) (see connection table). A maximum voltage of ±10 V is used for electrokinetic actuation. Most of the applied potential falls across the narrow section (orifice) of the channels generating the highest electric fields in that region only. Electric fields in the cell control region are estimated to remain below 4 kV/m. The needed actuation voltage on the electrodes is calculated by the flow control algorithm and sent to the digital-to-analog converter (DAC). The cell tracking algorithm allows tracking of individual cell in a field.

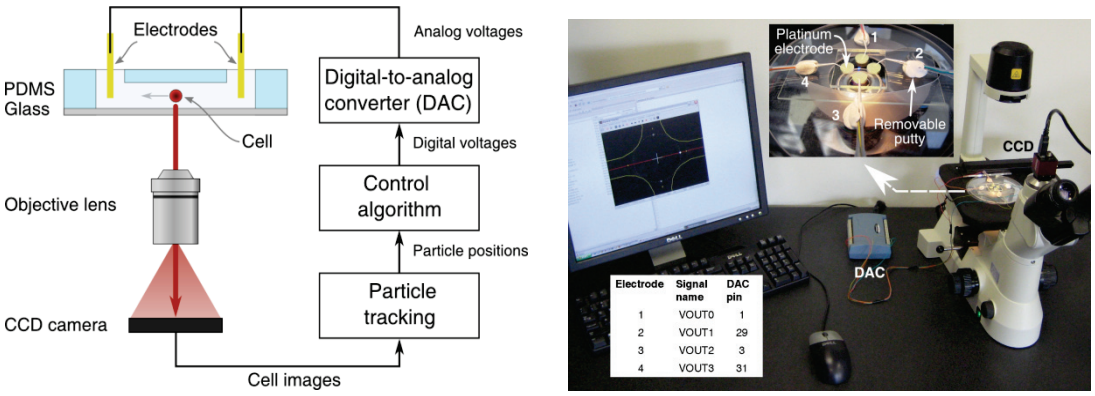

Figure 14: Schematic of the experimental setup: A CCD camera images the cells in bright-field or fluorescence illumination. A cell-tracking algorithm computes the position of the chosen cell and a control algorithm then determines the needed actuation voltages which are applied through a digital-to-analog converter (DAC) and platinum electrodes to the microfluidic device. (b) Photograph of the experimental setup with zoomed view of a microfluidic device. Here the yellow round shapes are the four reservoirs, platinum wire electrodes are brought in contact with the cell buffer fluid in these reservoirs. Left corner: The connection table for connecting the electrodes with the DAC (Measurement Computing USB-3101)

Materials used

This method is meant to manipulate a wide variety of user-selected particles and cells. Below I have used: polystyrene beads, yeast cells, human adult red blood cells and micro organisms from lake water

For bead steering experiments I used deionized water (J.T. Baker HPLC grade) with resistivity 1.25 MΩ-cm (measured using a Keithley 2400 Source Meter) and pH of 6.0 ±0.25 (as measured by Fisher Liquid Universal pH Indicator [pH measurement range 4 – 10]). Ultra-pure deionized water is expected to have a pH of 7.0 and resistivity of 18.0 MΩ-cm, but exposure to carbon dioxide in air typically results in a lowered pH of 5.7 and resistivity of about 1.0 MΩ-cm [134]. The beads are

Polysciences brand polystyrene beads (diameter 5 μm ± 0.975 μm standard deviation) or Duke Scientific fluorescent polystyrene beads (diameter 2.2 μm ± 0.11 μm). Bead solution was added to deionized water to achieve bead concentrations that would yield just a few beads in the control chambers.

For steering of cells, baker yeast (Red Star, Giant Food) were incubated for 24 hours in sugary water (30 mg glucose per ml). To make a single-cell suspension, the yeast solution was filtered using a 10 μm polyester filter (Fisher Scientific). This filtered yeast solution was added to the deionized water at 10 mg/ml. To prevent cell adhesion to solid surfaces, channels were filled with 20 mg/ml BSA (Bovine Serum Albumin) (Sigma-Aldrich), left for 30 minutes, and flushed 5 times with ethanol. I also added 1 mg/ml BSA to the buffer solution to prevent cells from sticking to each other and to replenish anti-stick surface coatings during the particle steering experiments. I have also used adult blood (1 μl) that was drawn from my fingertip and was diluted in 1 ml of phosphate buffered saline (PBS) buffer solution (pH 7.2). Microorganisms were collected from the surface of stones in a nearby lake and stream using cotton tipped applicators.

Kremser et al. [33] provides useful information on electrophoretic mobilities of a variety of microbes in various buffers. (The mobility for each microbe says how effectively that organism can be electrophoretically actuated by controlled electric fields. Electroosmotic actuation of the buffer fluid provides an additional actuating velocity.)

Electroosmotic Flow Actuation and Particle Velocities

Platinum electrodes inserted into the four or eight reservoirs actuate the fluid flow. The voltage on the electrodes is set by the control algorithm and is then passed to an operational amplifier (APEX) which had 17 available channels. For the two experiments, 4 and 8 out of the 17 available amplifier channels were used with a range of ±30 volts and ±10 volts respectively (the eight electrode device had shorter channels and required less voltage). The resulting electric fields create electroosmotic flow in the device and the flow velocity is given by [46, 83]

$$\vec{V}(x,y) = \frac{\varepsilon\varsigma}{\eta}\vec{E}(x,y) \qquad (18)$$

where $\vec{E}$ is the local electric field, it varies in the x,y directions and is uniform in the vertical z direction, ε is the permittivity of the liquid, η is its dynamic viscosity, and ζ is the zeta potential at the liquid/solid interface. I measured the value of the electroosmotic mobility by a current monitoring technique (as in [135]), and found $\vec{V}/\vec{E} = u = 36.5 \pm 3.6 \times 10^{-9}$ m^2 V^{-1} s^{-1} which is in good agreement with values of 36 x 10^{-9} m^2 V^{-1} s^{-1} and 40 x 10^{-9} m^2 V^{-1} s^{-1} reported for PDMS/glass channels at neutral pH [135, 136]. The zeta potential ς followed from equation (1) above which, for water at 25 ^{o}C, yielded $\varsigma = 46.9 \pm 7.6$ mV.

Particles are carried along by the electroosmotic flow, but charged particles also experience electrophoretic velocities. In the literature, electrophoretic mobilities have been reported for 50 nm to 1 μm diameter latex beads (c = -45 to –79 x 10^{-9} m^2 V^{-1} s^{-1}), for bacteria (-3.3 to –45 x 10^{-9} m^2 V^{-1} s^{-1}), yeast (-11 to –31 x 10^{-9} m^2 V^{-1} s^{-1}), endothelial cells (-7.4 x 10^{-9} m^2 V^{-1} s^{-1}), erythrocyte cells (-10.3 x 10^{-9} m^2 V^{-1} s^{-1}), and lymphocyte cells (-25.3 x 10^{-9} m^2 V^{-1} s^{-1}) [137, 138], [31-33], [139], [140], [140], [141]. Beads and cells acquire a surface charge depending on their surrounding pH, temperature, the concentration of the particles, and the type of impurities in the medium [83, 142].

No rigorous control of pH, temperature, concentration, and impurities was performed in these simple devices and this makes it difficult to determine electrophoretic mobilities reliably. (Recall that the steering algorithm does not need an accurate measurement of the particle mobilities. It works even if the mobilities are only known to within ±50 %.) During the steering experiments, the net particle mobilities are first measured on-line.

I have also measured mobilities independently off-line using devices with longer (5.6 cm) channels and applying a lower electric field (48.3 V across 5.6 cm versus 10 V across 1.4 cm [reservoir to reservoir 1.4 cm and reservoir to control chamber 0.7 cm]) to limit, and keep the particles further away from, regions of electrochemistry. The 5.0 micron polystyrene beads had a net (electroosmotic plus electrophoretic) mobility of $m = u+c$ = -20.8 ± 2.0 x 10^{-9} m^2 V^{-1} s^{-1}, the 2.2 micron beads had m= -55.5 ± 12.0

x 10^{-9} m^2 V^{-1} s^{-1}, and the yeast cells had m= -13.2 ± x 3.3 x 10^{-9} m^2 V^{-1} s^{-1}. This then gives a measurement of the electrophoretic mobility c as $m - u$.

Vision System to Locate Particles in Real Time

The same vision system was used for both single and multiple particle tracking. It included a 40x magnification transmitted-light microscope (Nikon TS100); a 40 frames-per-second, 480 by 640 gray-scale pixel camera (Vision Components, VC2038E DSP, Ettlingen, Germany); and a digital-signal-processing (DSP) unit located inside the camera that evaluated the particle-tracking algorithm (described below). For steering of the fluorescent 2.2 μm beads in the 8 electrode devices, the vision system further included a bright 1 Watt LED light source (465 nm (blue), Luxeon), and a high-pass filter before the camera (480 nm and up, Chroma Technology Corporation), so that the beads, which emit light at 510 nm (green), were seen more clearly as green on black.

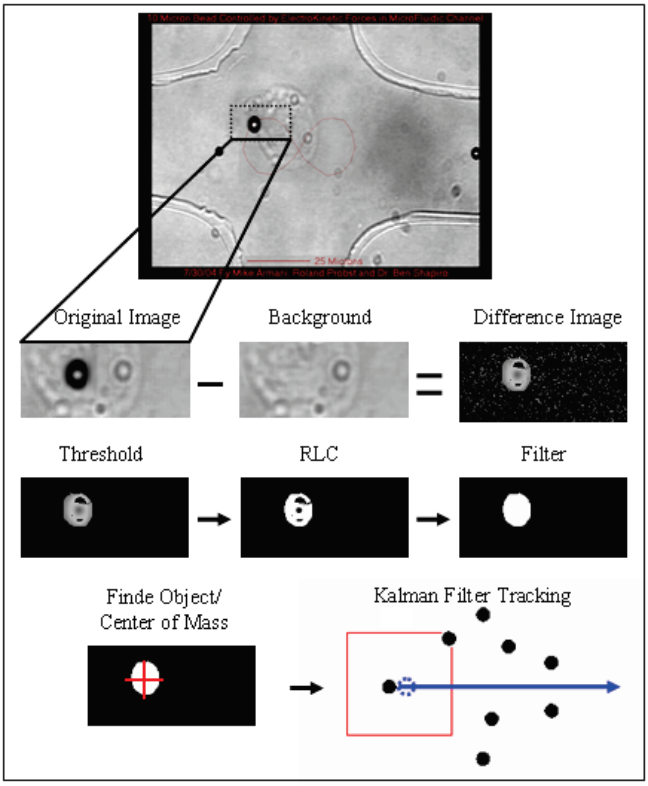

Figure 15: The real time algorithm for finding the (x,y) positions of all the particles. A reference image is taken of the device when there are no particles in the chamber. Then, for each incoming camera image, I subtract away the reference image to create a differential image that isolates the pixels corresponding to the moving particles. The differential image is threshold to remove the effects of noise and the centroid for each particle is computed. A Kalman filter allows tracking of individual particles.

The image-processing algorithm runs on the DSP unit in the camera and tracks the location of all particles of interest. It is a combination of an algorithm that finds all particles in an image frame and an algorithm that tracks individual particles (see Figure 15). A search window surrounds each particle that will be controlled. The algorithm compares the image in the window to a reference image with no particles resulting in a difference image. This image data is converted to run-length-code (RLC), threshold, filtered, and operated on by an algorithm that finds the center of mass of each particle. Before sending these positions to the controller, an algorithm,

based on a Kalman filter [130] determines whether each computed position belongs to the same particle or to an unrelated neighboring particle. The Kalman filter works by predicting the future position of all particles based on current predicted velocities that are estimated by prior particle position and the time between frames. The filter allows the tracking of individual particles through swarms of other particles.

This image processing and tracking software was coded in C and then compiled into fast assembly routines for the camera. The method finds the position of all the particles in the field of view in less than 25 milli-seconds and passes those (x,y) positions to the control algorithm.

Device Fabrication

The microfluidic device is fabricated by standard replica molding of PDMS and attached to a microscope glass slide. PDMS bonds to glass naturally by weak van der Waal forces and creates a reversible bond and water tight seal. The device has four large (8 mm diameter) fluid reservoirs which also serve as electrical access ports to the channels. Molds are designed in AutoCAD and fabricated in a clean room or ordered from a microfluidic foundry[55, 56].

The micro-fluidic devices were fabricated using the soft lithography steps described in [143]. Figure 16 shows the fabrication sequence for the PDMS device of that was used to steer a single particle by electroosmotic flow control.

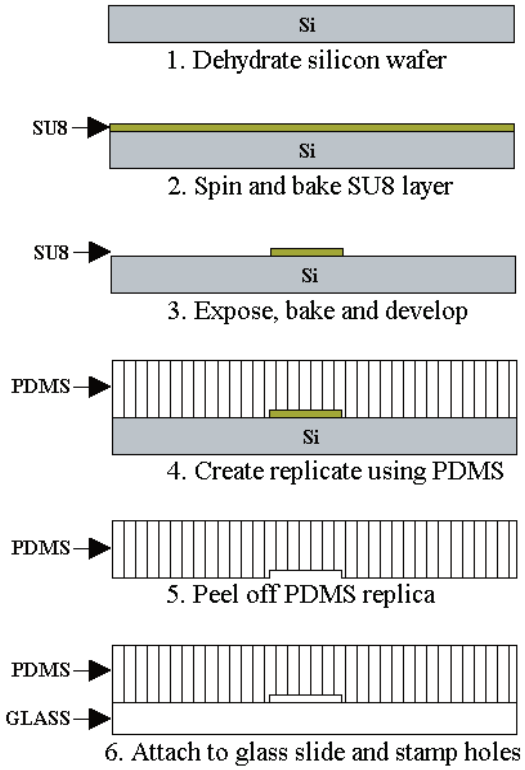

Figure 16: Fabrication sequence for the micro-fluidic particle steering PDMS devices.

The masks for the device were designed using AutoCAD. Chromium/glass masks were then obtained from Berkeley MicroLab (which used a GCA Mann 3600 Pattern Generator and mask developer to produce 5 inch wafers with features accurate to 10 nm).

An SU8 master template was created on a silicon wafer. The 100 mm silicon wafers were obtained from UniversityWafer. The wafers were baked at 200°C for one hour to dehydrate the wafer; 4 ml of SU8-5 (Microchem) was deposited on the polished side of the wafer and was spin coated at 500 RPM for 5 seconds and then 1100 RPM

for 30 seconds. This was followed by a soft-bake (95 ^{o}C for 30 min.), UV exposure (650 mJ/cm^2), post-bake (95 ^{o}C for 30 min), and development in SU8 developer (Microchem). The wafer was rinsed in liberal amounts of isopropanol, methanol, and deionized water and blow-dried with nitrogen.

Below are step by step instructions for fabricating a four electrode device.

1| Mix approximately 30 ml of PDMS polymer with the catalyst according to the manufacturers recommendations[144]. Usually, the weight ratio is 10:1 PDMS prepolymer to catalyst. Mix well for about 1 minute, or until the mixture is cloudy with bubbles.

CRITICAL: If PDMS is not mixed well it will not cure completely and will leave a residue on the master mold. If this happens, mix PDMS with slightly more catalyst (e.g. 10:3), pour onto the master mold, and continue to follow the steps below. After curing, this PDMS layer will remove any residue, leaving a clean and reusable master mold.

2| Place the master mold in a Petri dish and pour the PDMS mixture over the master - aim for a 3 mm thickness.

NOTE: Additional PDMS may be mixed and added over the master as desired. Thicker layers of PDMS are easier to handle, but take longer to cure.

3| Place the PDMS mixture and master mold into a vacuum chamber to remove bubbles that formed during mixing, or cover and let sit for 30 minutes.

4| Place the Petri dish on a leveled laboratory hotplate and cure for 1 hour at 60 ºCelsius or as recommended by the manufacturer.

NOTE: Faster curing (~10 minutes) can be achived at higher temperatures (150 ºCelsius). Please use a custom made aluminum petri dish as suggested in [50].

CRITICAL: Perform the next steps on a clean surface and use rubber gloves to reduce fingerprints and dust particles which easily adhere to PDMS and glass. Disturbances such as hair and dust on the PDMS surface will prevent complete sealing to the glass slide.

5| Using an X-acto knife or other blade, gently cut out the cured PDMS device from the master mold. Slowly peal off the device, being careful not to touch the bottom surface of the PDMS containing the channels.

6| Place the PDMS piece, channel side up, onto a clean cutting surface.

7| Apply matte finish Scotch tape to the bottom surface of the PDMS device to cover the channels. Use a hole punch (8 mm diameter) to punch out the four reservoirs through the Scotch tape.

NOTE: The channels and reservoirs will become clearly visible under Scotch tape and on top of a dark surface. The locations of the reservoirs are marked by

triangles arranged radially at the end of each microchannel.

8| Remove the Scotch tape from the hole punched PDMS device and apply a new piece of tape. Peel this piece of tape off to remove remaining residues and particles from the PDMS surface.

9| Gently lower the PDMS device, channel side down, onto a glass microscope slide.

CRITICAL: Allow the PDMS to adhere to the glass surface by itself. Do not push down. Excessive applied pressure may cause the channels to collapse, making them impossible to fill.

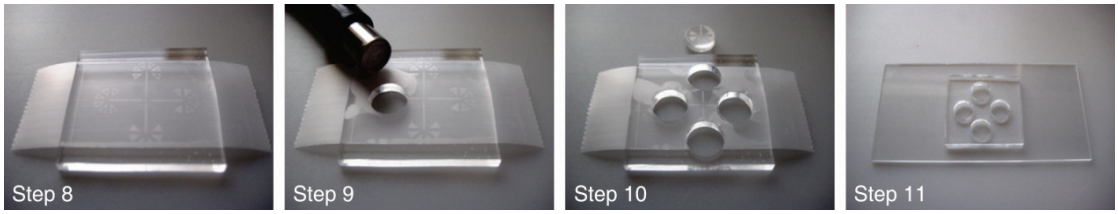

Figure 17: PDMS microfluidic device assembly sequence.

A photograph of the 4 electrode PDMS device and a schematic view of the cross-channel particle-control region are shown in Figure 18. The small 10 μm channel depth and the large reservoir geometry of the device were chosen to minimize the effect of parasitic surface-tension-driven pressure flows, which act as flow errors, compared to the desired electroosmotic flow control velocities.

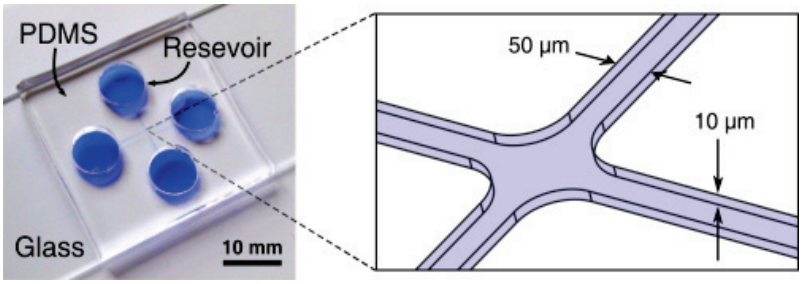

Figure 18: Left: Photograph of a 4-channel PDMS on glass device filled with blue food coloring to clearly show the microfluidic channels and reservoirs. Each microchannel is 10 mm long, 50 µm wide close to the particle steering intersection region and 300 µm wide otherwise, and 10 µm deep. Right: Schematic of the channel intersection and the 100 µm × 100 µm cell steering control area.

The fabrication of the 8 electrode devices was similar to the 4 electrode devices but with modifications based on lessons learned from steering a single particle.

The size of the reservoirs was increased and the electrodes were moved further away from the entry of the channel into the reservoir to decrease the effect of electro-chemical phenomena (such as electrolysis and acid/base fronts that originate at the electrodes [145]) on flow in the channels. To fit the larger 8-reservoirs geometry I used a 4 inch diameter Pyrex glass wafer instead of the 3 by 1 inch microscope glass slides. PDMS reservoirs were fabricated, as opposed to stamped, by including the reservoir shapes in the SU8 master template thereby creating more repeatable device geometries. Access holes to the reservoirs were still created by stamping. The channels lengths were shortened to 7 mm so that a lower voltage would create the same electric field and flow velocity in the central control chamber.

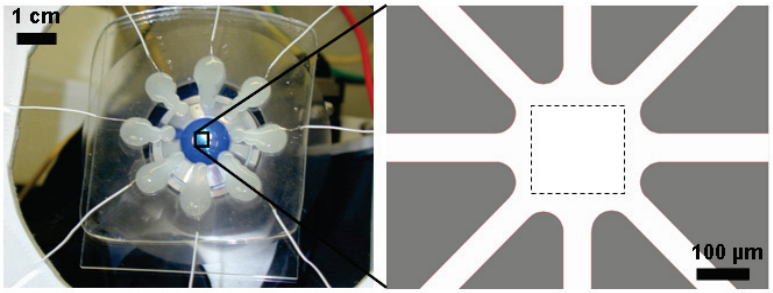

Figure 19: Left: The 8-electrode PDMS on glass device. Here the white bulb shapes are the eight reservoirs (big reservoirs are used to minimize surface tension driven pressure flows and electrochemical effects), platinum wire electrodes are brought in contact with the fluid in the reservoirs. In these wells, the 8 channels (each 7 mm long, 50 µm wide, 11 µm deep) are not visible, and a blue LED light (used to illuminate the fluorescent particles) brightly illuminates the center of the device. Right: A mask (a zoom) of the particle steering region (300 µm diameter, 11 µm deep).

Maximizing Actuation Strength in Control Area

Pressure flow in the system limits performance because it decreases the strength of fluid modes that are required for control of multiple particles. If I increase the number of particles the controller utilizes more fluid modes. The higher modes need more actuation per unit velocity and in an actuation restricted system that means slower and slower possible control as the number of particles/modes go up. To increase the electric field in the control area, I decreased the ratio of control area diameter to channel diameter. The improved design is shown in Figure 20.

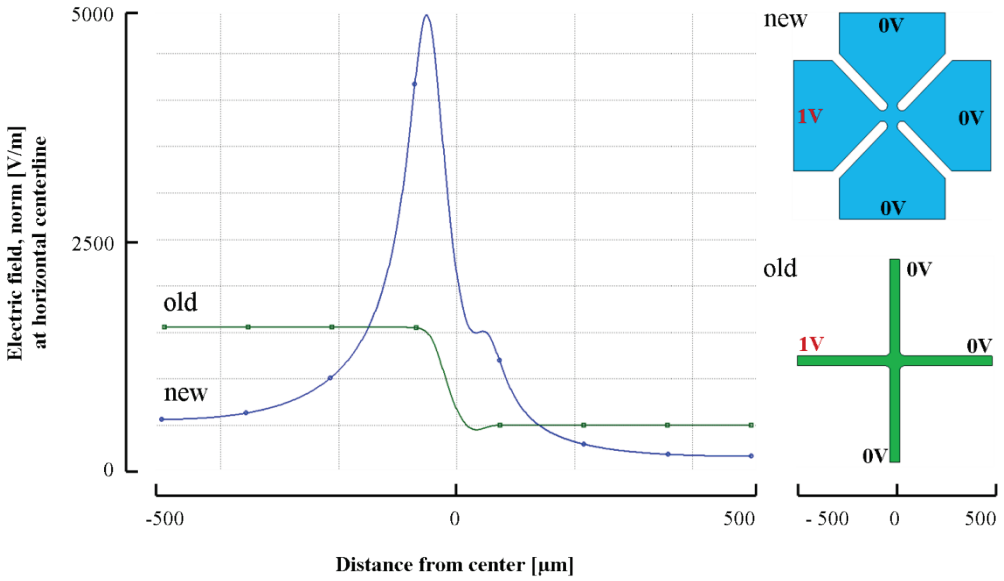

Figure 20: Left: Electric field distribution for both devices measured on a horizontal line across the device. The electric field in the center of the optimized devise (right top) has improved by a factor of 4.

Design Conditions for Living Cell Control

Keeping cells in a viable state is the main goal for future use of these cells in biotechnological applications. Therefore, I designed the system to minimize damaging effects on viable cells such as (a) electric field interaction, (b) Joule heating and (c) reactive ion generation at the electrodes. The device can generates low and safe electric fields to minimize harm to viable cells. As a consequence, these electric fields do not generate any appreciable Joule heating and the voltages at the electrodes are kept below the electrolysis threshold for water.

The device manipulates cells by either electroosmosis (EOF) or electrophoresis (EP). I recommend passivating the surface of the microfluidic cannels to prevent EOF and

to use EP for viable cell manipulation. Electrophoretic manipulation of cells has been performed since the 1920s[146]. Electrophoretic mobility of individual cells are routinely determined by conventional cell electrophoresis without damaging viable cells [147] and an extended database of hundreds of electrophoretic studies of eycaryotic cells over the past 40 years has been published by J. Bauer [146]. I use electric field strengths that are below the value reported in these cell electrophoretic studies. For instance, my device can generate a 10V/m field to move human myocytes with a velocity of 1.1μm/s as described in [148].

I minimize reactive ion generation at the electrodes by using actuation voltages below the voltage needed to electrolyze water (~1.25V). Consequently, less or ideally reactive species are generated at the electrodes and no bubbles occur. To further improve the design, it is recommended use non-gassing platinum, palladium or reversible Ag/AgCl electrodes. More advanced electrokinetic devices even used salt-gel-bridges [149] or ion exchange membranes [150, 151] to separate the electrodes from the cell buffer medium.

In general, capillary electrophoresis permits higher electric fields thanks to the efficient dispersion of Joule heat in narrow cannels. Simulations (COMSOL) show no appreciable increase of the buffer temperature at electric fields generated in the device. The temperature was estimated to increase by 0.05 Kelvin in the narrow section of the device. Experimental studies on Joule heating in similar devices has been conducted by Ross et al [152]. In their studies, the electric fields were 10.000

times higher (100kV/m) than the electric fields I intend to use for cell manipulation. Even at those extreme conditions the temperature increased by only 15 degrees Celsius after 25s.

Experimental Sequence

With the devices and vision system as described above, I now describe the experimental sequence to achieve particle steering. I first pressed the micro-channel PDMS layer on a microscope glass slide or a Pyrex wafer and filled the channels with methanol to make the channels hydrophilic. A drop of ethanol at one channel entry filled the entire structure. I then filled the reservoirs with deionized water using a pipette (1000 uL adjustable volume, Eppendorf) and allowed the water to mix with the ethanol. The water/methanol solution wicks from the reservoirs into the chamber to fill the entire device. Ethanol evaporates faster than water and so I placed the device on a hot plate, at 40°C for 30 minutes, to preferentially evaporate the methanol. Then all reservoirs were once again filled with deionized water to fill the device. This filling procedure was reliable and eliminated air bubbles.

Next I placed the device onto the inverted microscope and positioned it with the x-y stage to center the control chamber into the camera image plain. I inserted platinum electrodes into the reservoirs by hand and introduced particles into the system through one of the eight reservoirs. A voltage was applied on an opposing electrode to create an electroosmotic flow that moved the particles into the control region.

Before carrying out a particle steering experiment, I need to find the net mobility of the particles (electroosmotic plus electrophoretic), and provide that number to the model, so that the multi-particle steering algorithm, which operates on the model, has an approximately correct net mobility parameter. I measure the net particle mobility ($m = c+u$) on-line by applying a constant 10 V actuation at one electrode, while all the other electrodes are set to zero, and measuring the resulting velocity of one particle in the straight channel leading away from the activated electrode. Typical measurements for the bead and cell net velocities yield mobilities m = -16 to -35 x 10^{-9} m^2 V^{-1} s^{-1} for the 5.0 μm beads, m= -32 to - 60 x 10^{-9} m^2 V^{-1} s^{-1} for the 2.2 μm beads, and m = -20 to -40 x 10^{-9} m^2 V^{-1} s^{-1} for the yeast cells. The more uncertain on-line measurements largely overlap the off-line measurements (see Section IV-B) for the 5.0 μm beads and the 2.2 μm beads, but the two measurement techniques provide different results for the yeast cells. The results from the on-line measurements are used in the control algorithm because they provide a measure of the mobility of the particles in the control chamber, as opposed to mobilities of particles in a different device.

To carry out the particle steering control, I choose (by labeling particles within the vision algorithm by user directed mouse clicks) particles of interest from the numerous particles floating in the control region, and assign desired paths to these chosen particles. The vision system tracks each of these particles individually, and the control algorithm creates spatially- and time-varying flow fields that steers all these chosen particles along their desired paths. The vision system images and the control

electrode voltages are updated every 0.20 and 0.033 seconds for the single and multi-particle steering experiments respectively (in the older, single particle setup the camera and software were not yet synchronized).

Experimental Results

Here I show experimental results for steering of single and multiple, charged and close to neutral, particles and steering of biological cells along various desired trajectories.

Steering a Single Particle

Figure 21 shows the steering of a charged bead along a figure 8 in the 4-electrode device. The surface charge on the bead leads to an approximate electrophoretic mobility of $-57.3 \pm 5.6 \times 10^{-9}$ m^2 V^{-1} s^{-1}. The precise surface charge on the bead is not known (it depends in a complicated way on the pH, temperature, concentration and type of impurities in the surrounding medium), and is not required by the control algorithm.

The experiment of Figure 21 was performed before I had optimized the 4-electrode single particle steering device; as a result the particle steering accuracy is poor. For the field of view used in the single particle experiments, each pixel in the camera corresponds to a distance of 917 nm in the x direction and 687 nm in the y direction.

The deviation between the actual and desired path in Figure 21 is about 3 pixels, hence the steering accuracy here is about 3 microns.

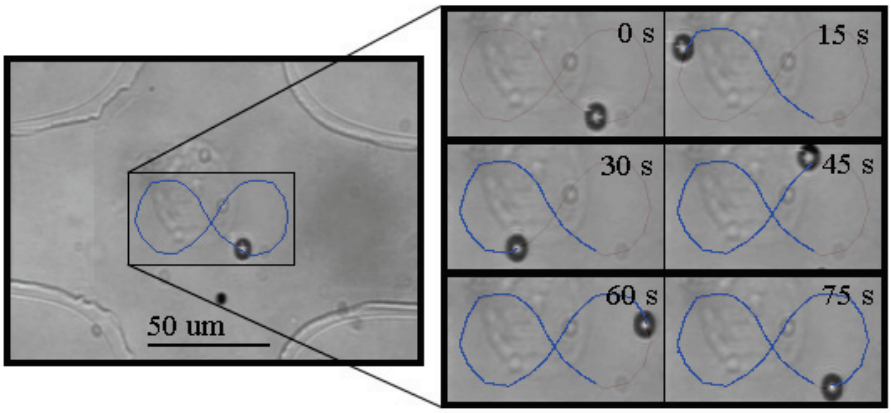

Figure 21: Control of a bead with significant surface charge along a figure 8. The bead has an approximate electrophoretic mobility of c = -57.3 ± 5.6 x 10^{-9} m^2 V^{-1} s^{-1}. (By comparison, the electroosmotic mobility of my PDMS devices is u = 36.5 ± 3.6 x 10^{-9} m^2 V^{-1} s^{-1}.) Left: Photograph of the micro-fluidic devices with the figure 8 path super-imposed on the image. Right: The actual path of the chosen 5 micron polystyrene bead (Polysciences Inc.) (black circle) in the feedback control experiment. Snapshots are shown at 6 equally spaced times. The bead follows the required trajectory to within three microns.

Steering Biological Cells

Figure 22 shows the steering of a 5 micron diameter yeast cell along a UMD path. Yeast cell electrophoretic mobilities have been reported to vary between –11 to –21 x 10^{-9} $m^{-2}V^{-1}s^{-1}$ [139]. The yeast cell is less charged than the polystyrene bead but it is still not perfectly neutral. Again, the exact charge or mobility of the cell is not important in terms of control and here the chosen cell was steered to an accuracy of one camera pixel (better than one micron) without using precise charge or mobility information. This experiment was an optimized version of the one in Figure 21.

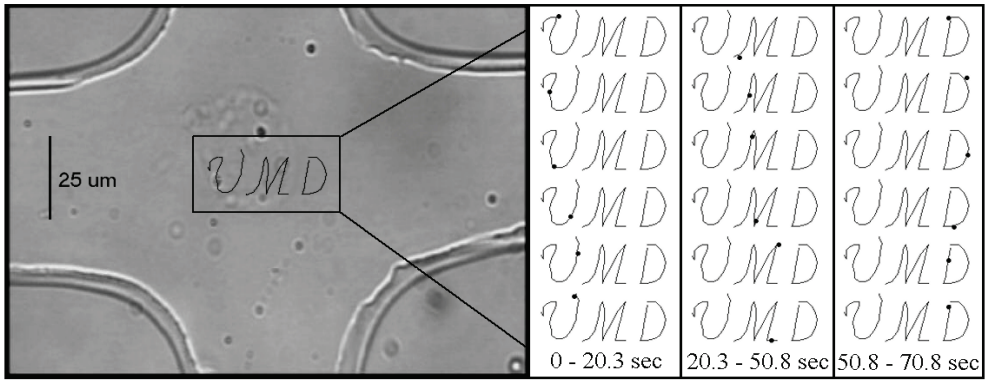

Figure 22: Steering of a slightly charged yeast cell along a UMD path. The cell has an approximate electrophoretic mobility of -23.3 ± 6.9 x 10^{-9} m^2 V^{-1} s^{-1}. Left: Photograph of the micro-fluidic devices with the cursive 'UMD' path overlaid on the image. Right: The actual path of the chosen 5 micron yeast cell (Red Star® Yeast) (black dot) in the feedback control experiment. Snapshots are shown at 6 equally spaced times for each letter. The yeast cell follows the required trajectory to within one micron. (This experiment was an optimized version of the Figure 21 experiment.)

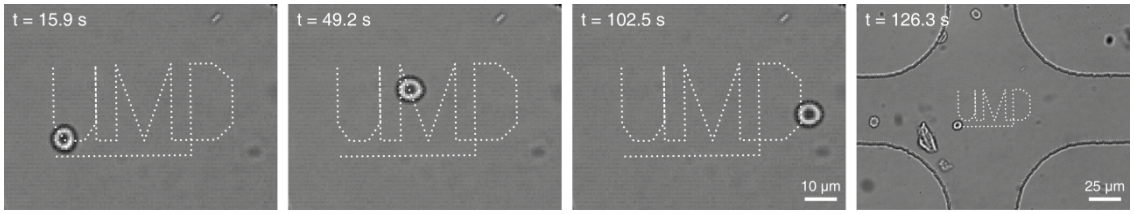

Figure 23: Four sequential snapshots of a red blood cell being steered along an UMD path, drawing out "UMD" (University of Maryland).

The simple 4-electrode polydimethylsiloxane (PDMS) on glass system, that has been optimized for robust operation and live cell compatibility, has achieved control of visible slow microbes. The existing system can control microbes whose swim speed is approximately < 10 μm/s though faster microbes that have predictable swim directions can also be controlled. Visibility of small microbes is limited by the magnification and quality of the microscope. However, the control approach described here will work for any suspended cells whose location can be visualized in real time, either by regular white light microscopy or by fluorescent means.

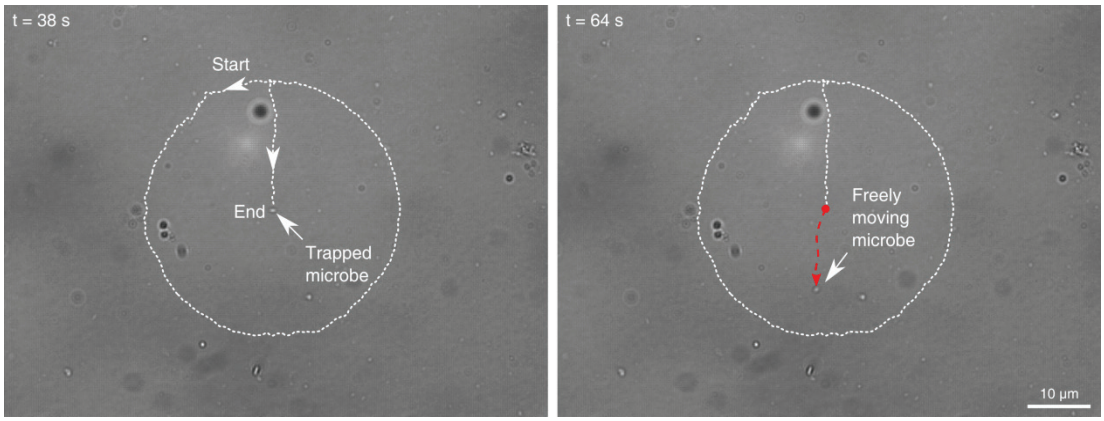

Figure 24: A motile microbe found in river water was moved on a circular trajectory (actual trace shown in dashed white) and trapped in the center for 22 seconds until being released from control (dashed red).

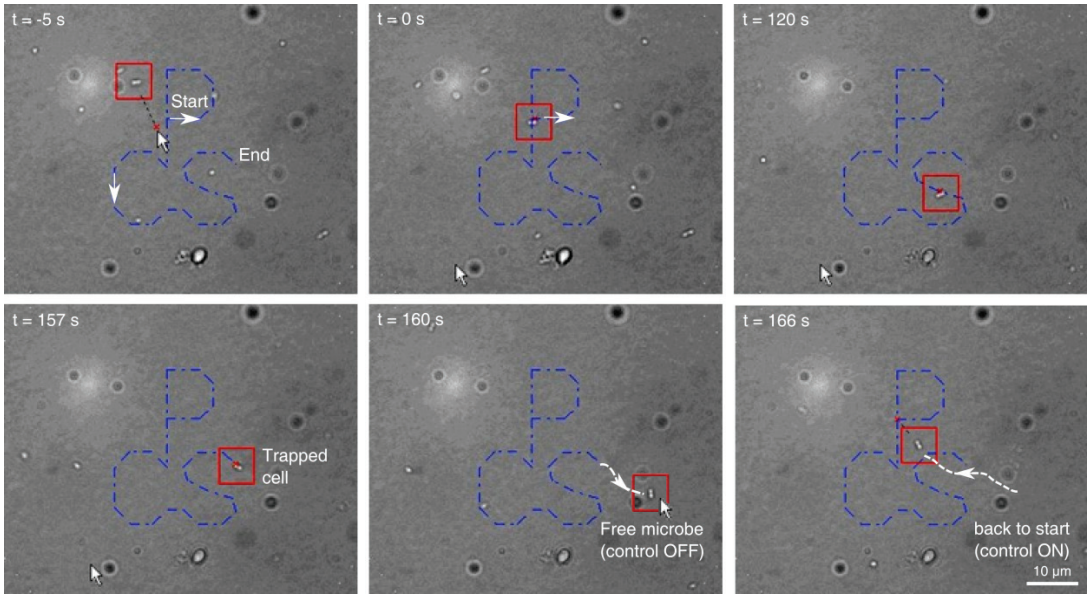

Figure 25: A motile microbe was steered around a trajectory spelling "PCS" (Probst, Cummins, and Shapiro, respectively). The microbe position at 6 time snaps is shown by the red squares. At the end of the trajectory, the microbe was freed from control allowing it to swim away (dashed white outward trajectory) and then reclaimed to the beginning of the trajectory (dashed white return path). Bacteria viability after control was verified by visual observation of its subsequent swimming activity.

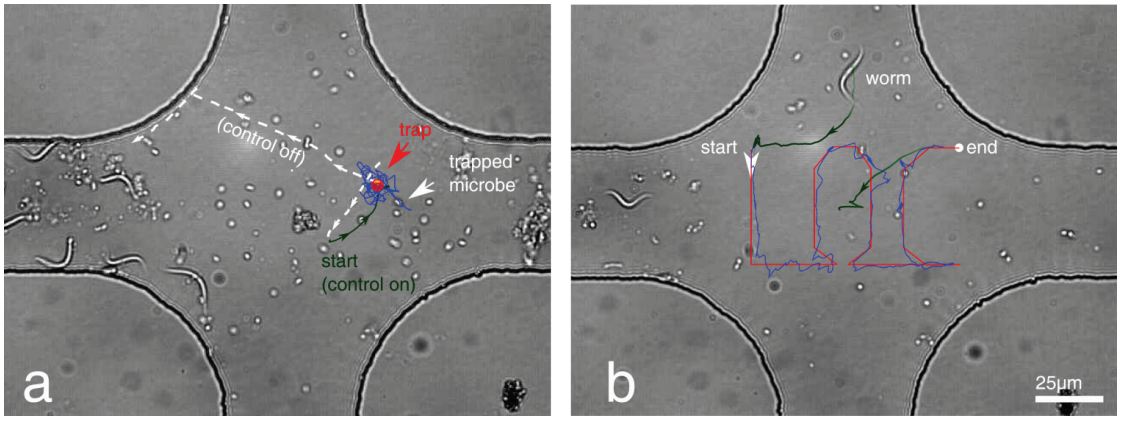

Figure 26: (a) A fast swimming microbe found in river water was moved to an arbitrary trapping location and trapped for 30 seconds until being released from control. Uncontrolled swimming is shown in dashed white, initial control to the trap or path is shown in green, and the controlled motion is shown in blue – as is evident, the microbe swims away after the control is turned off. (b) A worm was steered around a trajectory spelling "LOC" (for lab-on-a-chip).

Figure 26 shows results for steering and trapping motile microbes found in river water along a 'LOC' path (for lab-on-a-chip). During control, electrode actuation did not exceed ± 10 volts which generated electric fields < 4 kV/m in the cell control region. Such fields are considered safe for cell manipulation, as reported by Zimmerman[59] and Weaver et al.[60] for cell cultures and by Ebersol et al.[58] who found that the majority of tested microbes remained viable in electric fields of even 10 kV/m. Here we see that the microbes swim away after control has been turned off clearly showing that they are still alive and functioning.

Electrokinetic feedback control is a simple and powerful way to control cells that allows standard micro-fluidics systems (here a PDMS on glass device, four electrodes, a microscope, and a computer) to robustly steer living and swimming cells. The success of the control depends on whether the microbe can swim away faster between control actuations than the actuation can bring it back, which depends both on its swim speed and its swim patterns. So far, the system has been limited to control of slow microbes by the 30 Hz control rate which is in turn limited by the frame rate of the current camera.

Faster hardware will allow me to control more often per second and will thus give the microbe less time to escape between control corrections. I also plan to develop smarter control algorithms that will detect and exploit the properties of the specific microbe I am trying to control. A microbe that swims quickly in small circles is easy to control because it does not escape far between control updates. But for a microbe

that swims quickly but turns rarely, it makes sense to use that microbe past swim direction as a predictor of its future location and to then apply a control that will direct the microbe back from where it will be (instead of from where it is) to the target location.

Steering Multiple Particle

The 8-electrode device has 7 degrees of freedom (one mode has negligible contribution) and can precisely steer up to 3 particles (each particle has 2 degrees of freedom). Figure 27 shows the simultaneous steering of three polystyrene beads along three circular paths.

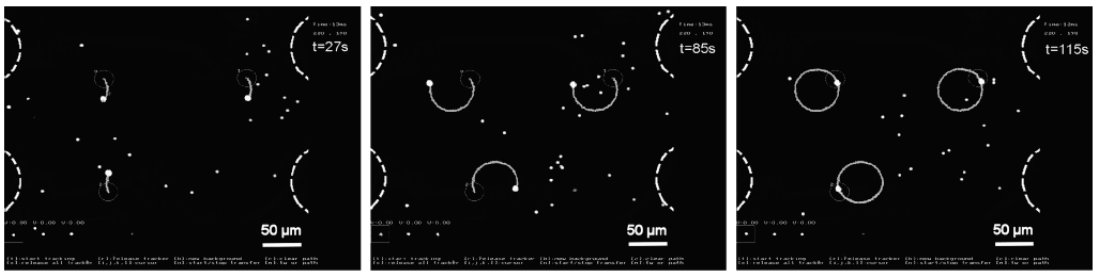

Figure 27: Steering of 3 fluorescent beads (2.2 µm diameter, Duke Scientific) with large surface charge (electrophoretic mobility of -92.0 ± 15.6 x 10^{-9} m^2 V^{-1} s^{-1}) around 3 circles. The electroosmotic mobility of my PDMS devices is u = 36.5 ± 3.6 x 10^{-9} m^2 V^{-1} s^{-1}. In the experiment, the fluorescent beads appear as small green dots on a black background and the device geometry, which does not fluoresce, is not visible. Here, the white dots are the beads (enlarged), the blue curves are the actual trajectories that the target beads have traced out (overlaid), and the dashed white curves (also overlaid) show the geometry of the channels and the particle control chamber. Snapshots are shown at three time steps. The three beads are being steered to within an accuracy of one pixel (corresponding to less than 1 µm). The desired paths are not shown because, at this image resolution, they would perfectly underlay the actual paths.

The control algorithm can trap particles by forcing a particle to move back to its desired position whenever it deviates away due to external forces. This can be done even while other particles are being steered along their paths.

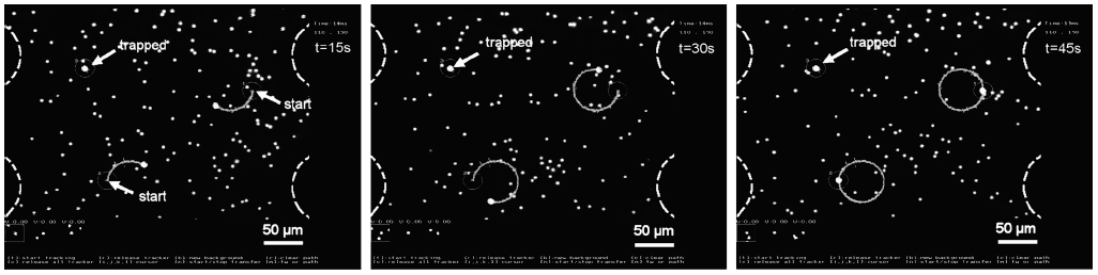

Figure 28 shows the steering of two beads along two circular paths while a third bead is controlled to stay at a fixed location. The better than 1 µm trapping accuracy is set by the optical resolution of the vision system.

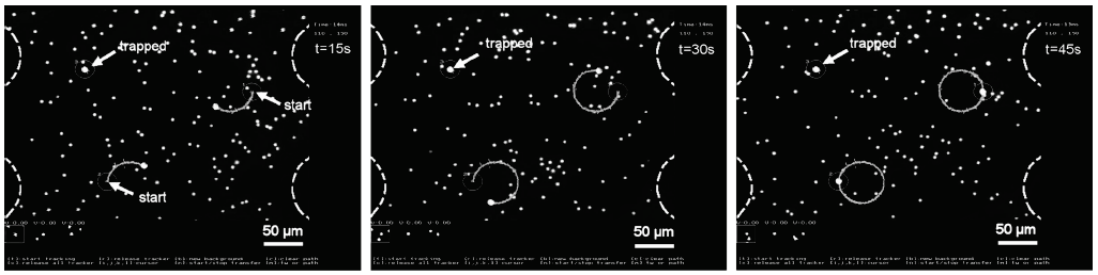

Figure 28: Steering of 2 fluorescent beads around 2 circles while a 3rd bead is held stationary. The trapped bead is marked by the arrow, and is held in place by the control algorithm to an accuracy of better than one micron. Every time the bead deviates from its desired position, a flow is created that pushes the bead back towards its desired location. (The properties of the beads and the format of the figure are the same as in Figure 27.)

Both neutral and charged particles can be steered. I did not have access to particles that remained perfectly neutral when immersed in water, but Figure 29 displays the motion of three yeast cells, which acquire less surface charge than the beads, being steered along two circles and a 'UMD' path.

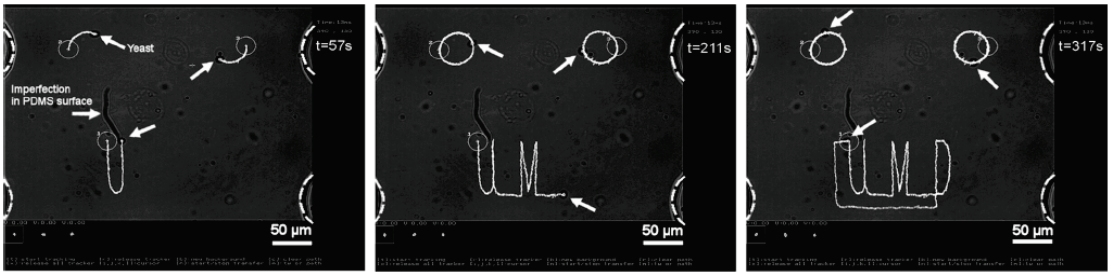

Figure 29: Steering of 3 yeast cells with small surface charge (electrophoretic mobility -23.3 ± 6.9 x 10^{-9} m^2 V^{-1} s^{-1}) around two circles and a 'UMD' path (for 'University of Maryland'). The cells do not fluoresce. In these images there is no high-pass filter before the camera and the raw images are shown. The yeast cells are visible as small black dots with a white center (the three target cells are marked with a white arrow in each image), and the white curves are the trajectories that the target cells have traced out. The three beads are being steered to within an accuracy of one pixel (corresponding to less than 1 µm).

The steering control algorithm can correct for large errors, it can steer chosen particles to their desired locations even if they are initially far away. Here the control has been turned off for 5 seconds until the beads have drifted away a considerable distance, the control is then turned back on and the algorithm drives the original three beads back to their desired paths. By creating way points from original to desired particle locations, I can create a globally stable control scheme, which can correct for initial particle position errors of any size, but this has not been done yet.

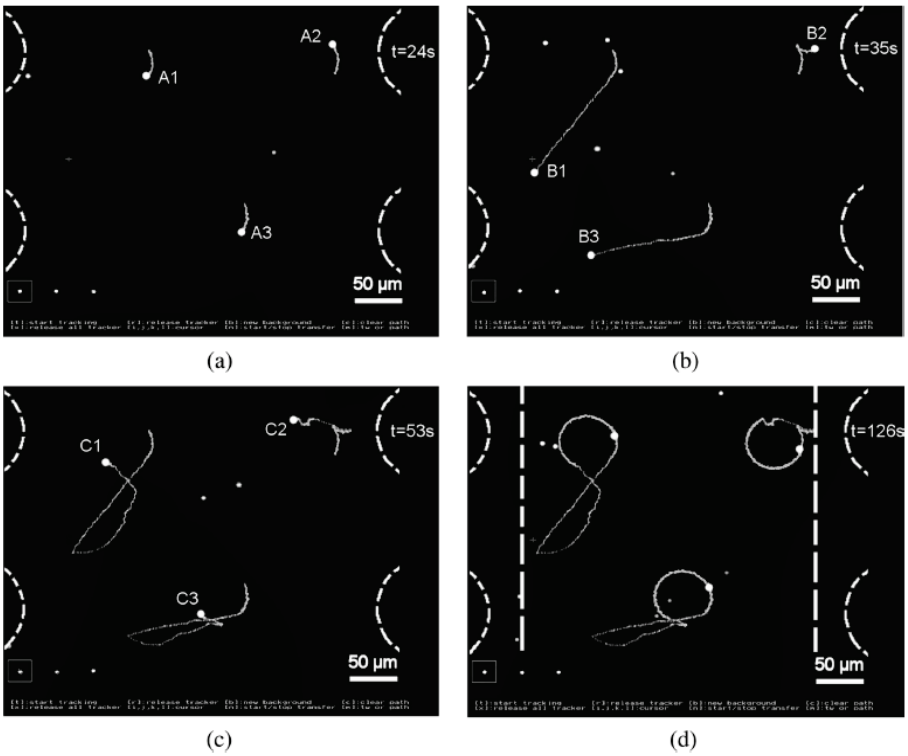

Figure 30: The control algorithm can correct for large errors in particle positions. This figure shows steering of three fluorescent beads (2.2 µm diameter, Duke Scientific) around three circles. At time t=24 s, corresponding to bead positions marked A1 , A2 , and A3 , the control was turned off for 11 s, allowing the particles to drift away (primarily due to the slow parasitic flow caused by surface tension forces at the reservoirs) by up to 150 µm. The control was then turned back on at t = 35 s (B1 , B2 , and B3), and the control algorithm steered the three original beads back to their desired positions (C1 , C2 , and C3). Four time instants are shown. (a) Right before control is turned off. (b) Right before control is turned back on (the three beads have drifted away a large distance). (c) At a time when the beads are back on track. (d) Final time when the beads have completed the remainder of their three circular paths (again to an accuracy of better than 1 µm). The two straight lines in the last image illustrate the left and right boundaries of the control region. The control voltages scale with the size of the position errors. Position errors are very large and this would lead to very large control voltages. Therefore, the control scheme has been slightly modified: the control gain per particle is scaled in such a way that the voltage remains within the allowable [-10, +10] Volt range.

Steering Accuracy

The spatial accuracy of particle steering is determined primarily by the field of view associated with a single camera pixel. In the single particle experiments, one camera pixel corresponded to a spatial displacement of 917 nm in the x direction and 687 nm in the y direction (the pixels are rectangular). In the multi-particle experiments, a

slightly smaller field of view was used, and one pixel corresponded to 625 nm and 468 nm distances respectively. Both the single and multiple particle algorithms steer the particles to within one pixel of their desired paths. This single pixel deviation corresponds to a maximum spatial error of 0.917 μm and 0.625 μm for the single and multi-particle steering experiments respectively.

The other sources of errors are much smaller. There is an error due to the finite control update time. Control inputs are updated every 0.20 seconds (for the older single particle experiments) and every 0.033 seconds (for the multi-particle experiments). During this control update time *dt* the particle can deviate away from its desired location due to Brownian motion. The deviation amount δ_B is predicted by [83]

$$\delta_B = \sqrt{\frac{kTdt}{3\pi\eta a}} = \sqrt{\frac{1.3807\times10^{-23} JK^{-1}\times 300K\times 0.033s}{3\times 3.14\times 0.001 Ns/m^2\times 2.5\times10^{-6} m}} = 7.6\times10^{-8} m = 76nm \quad (19)$$

where k is the Boltzmann constant, T is the ambient temperature, dt is the time interval, η is the dynamic viscosity of water, and a is the particle radius. During this control update time there is also an error created because an old control actuation is being applied to a slightly new particle position. This creates a position error δ_C that is bounded by the maximum particle velocity (V < 5 μm/s) times the update control time interval *dt*, the resulting error $\delta_C \le V \times dt$ is less than 0.25 micrometers.

Miniaturization

In order to develop cell-based sensors that may be operated without requiring the support infrastructure of a cell biology lab, it is important that the vision system for cell steering (the imaging sensor, image processing algorithms, and controller) have the same dimensions as the actuation system. The existing macro-scale camera will eventually be replaced with an on-chip contact imager, which is a conventional image sensor used for direct imaging of objects in the near field without the need for intervening optics. To demonstrate system integration and portability I have built a handheld device prototype that can be used to manipulate biological cells in micro fluidic networks. This compact device consists of a conventional USB web cam, single lens optics and micro fluidic channels. A conventional laptop with matlab software runs image processing and control algorithms to generate appropriate control signals that are applied through a DAQ card into the micro fluidic device. An operator can use the mouse to choose a biological cell that is visible in the image plane and drag it to a desired position. With a 2.5 mm ball lens I was able to design an optical system that is as flat as 0.6". Smaller ball lenses lead to even smaller dimensions.

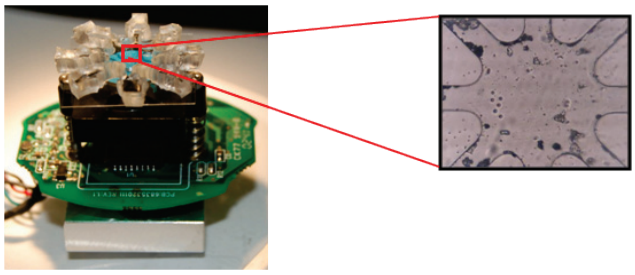

Figure 31: This figure shows the handheld prototype with a close-up of the microfluidic channels at the center.

Chapter 3: Manipulating Quantum Dots to Nanometer Precision

This chapter demonstrates positioning of single quantum dots by control of the surrounding fluid flow and show that this technique can be used to hold a nanoparticle in place well enough to take *in situ* characterization measurements.

Experimental Design Advancements

This section covers experimental advancements required to control quantum dots. Figure 32A illustrates the device and operation principle used to manipulate single QDs using flow control. The device is composed of two microfluidic channels that intersect each other at a 90 degree angle. This design is first patterned into polydimethylsiloxane (PDMS) and then adhered to a glass slide cover to form the microfluidic channels. The control region is located at the intersection of the two channels and is approximately 5 μm in height and 100 μm x 100 μm in size, though it can easily be made larger. Electroosmotic flow actuation is created by electrodes placed in four fluid reservoirs at the ends of the channels. The two channels are subsequently filled with a water-based fluid containing CdSe/ZnS QDs (Qdot® 655 nm ITK™ amino), along with a mixture of 1.25 wt% of an associating polymer (RM-825, Rohm and Haas Co.)[154] and 0.55 wt% of a zwitterionic betaine surfactant [155].The associating polymer is used to increase the viscosity of the fluid to 0.23 Pa-s by hydrophobic clustering [156] in order to decrease QD Brownian motion, while the surfactant is used to enhance fluid actuation. The colloidal QDs are illuminated

with 532 nm light at an intensity of 250 W/cm^2 and imaged using an inverted confocal microscope.

Control is achieved by imaging the photoluminescence of single QDs on a CCD camera and these images are used to create a feedback signal that provides the precise flow needed to correct the position of the QD. In order to achieve nanometer scale precision it is necessary to overcome the granularity of the pixel spacing and the diffraction limit of the imaging system. These limits are overcome by incorporating sub pixel image processing algorithms that can accurately determine the position of the QD from its image to much higher resolution than that of the imaging optics [157]. The combination of image processing and control enables me to select any QD within the 100 μm control region and position it with nanometer accuracy without applying high power optical fields.

The entire tracking system with the feedback control loop is depicted in Figure 32. Images are acquired from the CCD camera at a 20 Hz frame rate and then processed in real time using a centroid algorithm to precisely determine the position of the QD. The control algorithm then calculates the voltages needed to move that QD to its desired location by decomposing the needed displacement vector into its vertical and horizontal fluid modes as illustrated in Figure 32(C). The necessary voltages are then applied to each of the four electrodes to move the QD as desired. Platinum electrodes are used to minimize unwanted electrochemistry effects in the fluid. Although the target QD is controlled in the plane, the QD can still drift slowly in the third

dimension causing it to go out of focus and thus degrade the accuracy of the vision-based control. To correct this, the imaging objective is mounted on a piezo stage and a second Newton-bracketing feedback control algorithm uses the variance of the QD image as its metric to track the QD in the z direction, thus keeping it in focus. This improves control accuracy in the xy plane.

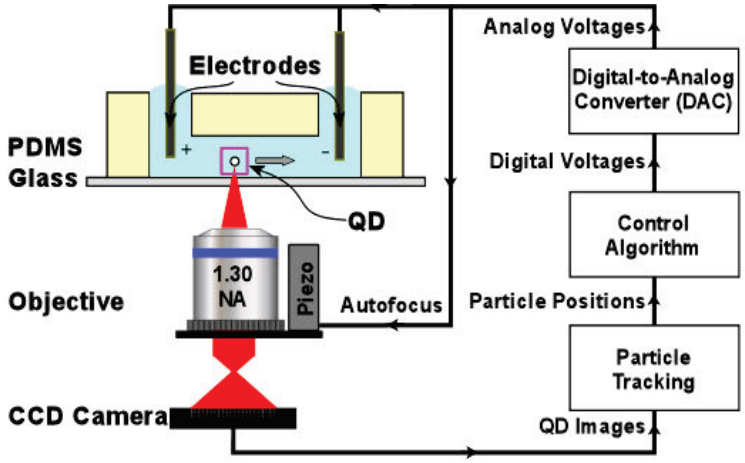

Figure 32: Illustration of the optical and electronic setup for tracking and feedback control of QDs. A CCD camera images the QD and sends the information to a tracking algorithm that uses sub pixel averaging to accurately determine the current position of the QD. The control algorithm uses this information to determine the proper voltage to apply to the electrodes in order to move the QD to its desired position. A second feedback loop moves the imaging objective in the z-direction using a piezo stage to keep the QD in focus.

Steering a Single Quantum Dot

The ability to accurately manipulate QDs in two dimensions is shown in Figure 33. A single QD is selected from the 100 μm control region which contains approximately 10 QDs. A small area around the QD, denoted by the box, defines the 16 x 16 pixel

tracking window used to calculate the QD position via the centroid algorithm. Panels a-c show the position of a single QD at several different times as it is controlled along a well-defined path. The inset to Figure 33(A) shows a close up of the tracking window. The desired position was progressed along the fixed trajectory at a speed of 2 μm/s while the control algorithm continuously adjusted the applied voltages to move the QD towards this moving target. In order to determine whether the QD had blinked off, a threshold camera intensity was selected. When the camera signal fell below this threshold, all voltages were switched to zero and the controller halted to wait for the QD to begin re-emitting. While waiting for the QD to resume photon emission, the tracking region was temporarily expanded to three times its size to ensure that Brownian motion would not carry the QD out of the detection window before it began re-emitting. The full trace of the QD position is shown in Figure 33(D) and is overlaid on the desired trajectory. The times when the QD blinks 'off' are shown in red. Analysis of the position data found that the QD was held to within a standard deviation of 152 nm from the desired trajectory.

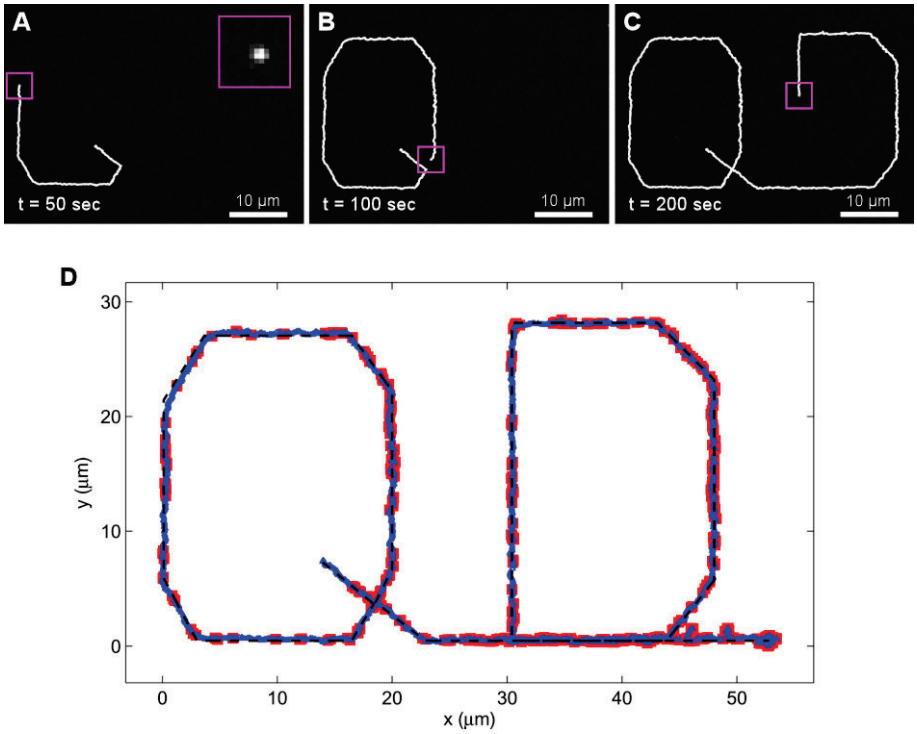

Figure 33: Single quantum dot trajectory. (A-C) Time stamped CCD camera images of a single quantum dot being steered along the desired trajectory (full movie available in supporting online material). The white trace shows the measured path of the quantum dot up until its current location. The square magenta box shows the sub pixel averaging window used to determine the current position of the QD. The inset in panel (A) shows a close-up of the sub pixel averaging window which contains the QD near its center. (D) Plot of quantum dot position along its trajectory. The dotted black line shows the desired trajectory programmed into the controller. The actual measured QD trajectory is shown in blue. The solid red squares depict when the quantum dot blinks off. At the end of the trajectory the QD is held in place for 2 minutes. The deviation of the QD trajectory from the desired trajectory is calculated to be 152 nm.

To determine the positioning accuracy of the control method, a single QD was once again selected and moved to a specified location near the center of the control region. The QD was held in that position by feedback control and monitored for a 5 minute time span. The feedback control was subsequently turned off and the QD was allowed to freely drift by Brownian motion for another 5 minute measurement interval. Figure 34 shows the measured position of the trapped and free QD as blue and red dots respectively. To determine the inherent vision accuracy of the centroid algorithm, a

third measurement was taken on a single QD that was adhered on the surface of a glass slide. The measured positions of the adhered QD are shown as green points in the figure. From the standard deviation of the green points one can determine the position accuracy of the centroid algorithm to be 28.5 nm. From the standard deviation of the blue points, it appears that the QD was trapped to within 84.3 nm accuracy.

To investigate the trapping time, a second QD was positioned and trapped for 1 hour. From the position data it was found that this QD was held with 110 nm accuracy. The slight degradation in position accuracy was due to the fact that by the end of the 1 hour, the QD was emitting much less brightly and blinking significantly more due to oxygen contamination and photo bleaching. The increase in blinking served to reduce the position accuracy because the QD was able to drift for a longer distance before re-emitting. In fact if one correct for this excessive blinking by removing the first second worth of data points during which a QD is being actively returned to position following having been blinked of for more than 10 seconds I recover a more reasonable standard deviation of 86.8 nm. This degradation is due to oxygen contamination and can be reduced by incorporating oxygen scavenging chemicals in the solution. At no time during the 1 hour period where multiple QDs inadvertently trapped by the controller. Such trapping times for single QDs have not been demonstrated using other trapping methods. For comparison, the non-specific trap created by an optical tweezers will trap additional quantum dots on a timescale of 5-10 minutes (*9*).

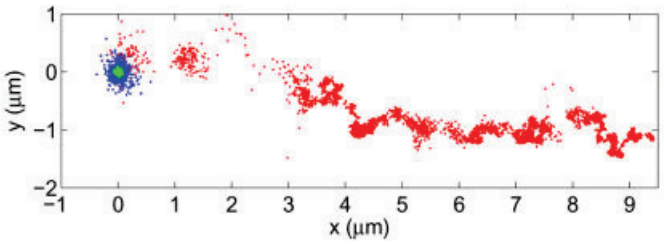

Figure 34: Measurement of QD positioning accuracy. Blue points represent the measured position of the QD as it is held in a desired location by flow control for 5 minutes. The standard deviation of the blue points is calculated to be 84.3 nm. The controller is subsequently turned off and the QD is allowed to drift away for another five minutes, as shown by the red points. The drift to the right is caused by a small pressure flow in the device, a flow that is continuously corrected for when feedback control is on. To determine the vision accuracy of the system a third experiment is carried out for a QD adhered to a glass slide. The positions of the adhered QD are shown in green and have a standard deviation of 28.5 nm.

Positioning Accuracy

The positioning accuracy of the control is fundamentally limited by the Brownian motion of the particle and the accuracy of the vision sensing, determined mainly by shot noise. The variance of the QD position is thus limited by

$$\sigma^2 = \sigma_{diff}^2 + \sigma_{vision}^2 \tag{20}$$

where $\sigma_{diff}^2 = 2D/F$ is the noise due to diffusion and $\sigma_{vision}^2 = \lambda^2 F/4R$ is the imaging noise in the shot noise limit[158]. In these expressions, D is the diffusion coefficient, F is the camera frame rate, λ is the emission wavelength of the QD, and R is the detected photon flux. For a spherical particle the diffusion coefficient is given by

$$D = K_B T / 6\pi\mu a \tag{21}$$

where T is the fluid temperature, μ is the fluid viscosity, and a is the particle radius. From this expression one can see that the variance in particle position scales inversely with particle radius through the diffusion coefficient. This is in contrast to optical traps where the trapping accuracy scales inversely with radius cubed.

As the frame rate is decreased, uncertainty due to shot noise is also decreased because more photons are collected, but uncertainty due to Brownian motion increases because the QD has more time to diffuse between successive control updates. This tradeoff leads to an optimal positioning accuracy of

$$\sigma_{opt} = \sqrt{\lambda}\left(2D/R\right)^{1/4} \tag{22}$$

which is achieved at an optimal camera frame rate of $F_{opt} = \sqrt{8DR/\lambda^2}$. The QD emission rate R was determined with the use of an avalanche photodiode to be 70,000 cps, and the diffusion coefficient was determined by dynamic light scattering to be 7×10^{-14} m^2/s. Using an emission wavelength of λ = 655 nm, the predicted optimal position accuracy was determined to be 23.3 nm, which is achieved at a camera frame rate of 515 Hz. However, the feedback system works at a slower frame rate of 20 Hz due to the limited speed of the camera and data acquisition system. When using a 20 Hz frame rate the positioning accuracy is determined to be 84 nm, which is in excellent agreement with the 84.3 nm positioning accuracy measured earlier for the 5 minute holding experiment.

Autocorrelation Measurement of a Single QD

To ensure that the system controls a single QD, and to demonstrate that one can characterize the single photon nature of the emitter while simultaneously performing control, Chad Ropp carried out an autocorrelation on a dynamically positioned QD. A 25-75 beam splitter was used to deflect 75% of the light away from the camera and into a Hanbury-Brown-Twiss (HBT) type autocorrelation measurement composed of a 50-50 beamsplitter and two avalanche photodiodes. The remaining 25% was sent onto the camera for positioning the QD. To reduce uncorrelated background counts the autocorrelation setup has been gated to accumulate data only when the QD was not blinked off using the intensity threshold from the CCD camera image. The results of the autocorrelation measurement are shown in Figure 35. The autocorrelation integration was taken over 15 minutes and yielded an estimated $g^2(0) = 0.37 \pm 0.02$ and decay time $t_d = 22.73 \pm 1.07$ ns. This clear signature of anti-bunching demonstrates that the system indeed controlls a single QD. The measured decay time is comparable with previously measured values [159]. This result ensures that one can use the QD as a single photon source for integration with nanophotonic structures while simultaneously positioning it with flow control.

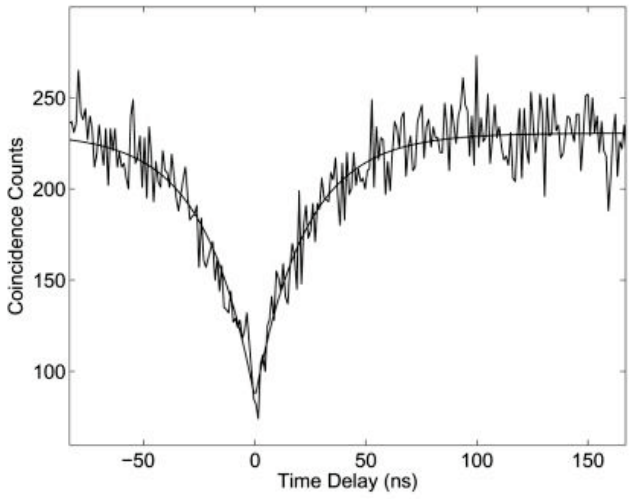

Figure 35: *In situ* autocorrelation measurement of a single QD. Autocorrelation measurement of a single controlled quantum dot obtained from a 15 minute integration with 1 ns binning and with exponential fits shown. From the exponential fit we determine $g^2(0) = 0.37 \pm 0.02$ and decay time $t_d = 22.73 \pm 1.07$ ns.

Chapter 4: Three Dimensional Electrokinetic Tweezers

Microfluidic electrokinetic tweezing systems have been restricted to manipulation in only 2 spatial dimensions. Here I demonstrate a control algorithm and a simple and novel device design that can manipulate particles in 3 dimensions by either electrophoretic forces (for particles that acquire a surface charge) or by 3D electroosmotic manipulation (for uncharged particles).

Introduction

Vision-based electrokinetic feedback control has allowed simple microfluidic devices to manipulate microscopic and nanoscopic objects on chip [12, 15, 81, 82, 133]. Electrokinetic manipulation, which includes electrophoretic[162] and electro-osmotic[163, 164] actuation, does not require lasers and does not rely on the dielectric properties of the particles to be manipulated. It thus allows control of essentially any visible objects [82, 133, 165]. EK tweezing has enabled on-chip individual manipulation of one and multiple cells[82], including the steering and trapping of live swimming cells[132]. The favorable scaling of electroosmotic actuation (drag forces scale with particle size[47] rather than with particle volume as do optical forces[72]) has further allowed control of nanoscopic particles to nanometer precision[133, 166], the best reported precision to date for any method. Recent theoretical work has also shown that EK manipulation can also control the orientation of objects in addition to their position[167] by modulating the shear

around them to cause object rotations. However, all of these prior results have been restricted to control in two spatial dimensions only.

Here I show a novel and simple device design, along with the associated control algorithms, that can extend EK control capabilities to the third dimension. The device design, theory, and numerical results I present here are a pre-requisite to subsequent experimental demonstrations, as has been the case for all prior theory developments[125, 153, 167, 168] that subsequently led to experimental demonstrations for control of cells[125], swimming bacteria[165], and quantum dots[82, 132, 133, 165, 169].

As in[170], I place actuating electrodes above and below to create force components in the vertical direction. However, my design (Figure 36) can further create both electrophoretic and electroosmotic vertical forces (the latter is more challenging since EO flow actuation is fundamentally along microfluidic channels and has been restricted to planar flows in planar devices[162]) allowing 3D control of both charged and neutral particles. This design incorporates all the lessons learned from prior experimental work: it places the electrodes far away from the control region to prevent the generation of bubbles by electrolysis from interrupting the control; it has a flat and clear control region to provide easy and distortion free optical access as will be needed for horizontal and vertical position sensing[171, 172] and its layered design is both straight-forward to fabricate and creates significant electrophoretic and electroosmotic vertical force components. For this new device design, I state a 3D

first-principles physical model for EP forces and EO flows based on my understanding of the physics from prior work[82, 125], and I then develop algorithms for and demonstrate 3D control of one and two particles in simulations.

I first briefly summarize how electrokinetic tweezers work in two spatial dimensions[82, 125] before showing how to extend the method to work in the third dimension. As shown in Figure 1, a micro-fluidic device, a vision system (microscope, camera, and particle detection software), and a control algorithm are connected in a feedback loop. The vision system identifies the location of each particle in real time, the control algorithm then compares the current position of a target particle with its desired position. If the two positions differ then the actuating electrodes create the right electrokinetic velocity (at the particles location) to move it from where it is to where it should be. This velocity can either be created by an electric field to move a charged particle relative to the buffer (EP actuation), or by an electroosmotic (EO) actuation of the flow that will carry a neutral particle along, or by a combination of both. The whole feedback loop repeats at each time to continually move any target particle from its actual position closer to its desired location, thus either trapping it (continually putting it back to a stationary desired location) or steering it (continually moving it to a new desired location).

Device Design

Instead of one planar layer, the device for 3D control consists of three layers which can be fabricated by replica molding of PDMS as described in Jo et al.[173] and

Zhang et al.[174]. The top and bottom layer contain the micro channels and the middle layer has a through hole which connects them. In this intersection the flow coming from a top channel can move into a lower channel and vice versa. Therefore, any object located in the intersection can experience a sink or lift force if the actuation is applied from a top to a bottom electrode or vice versa. This can move a particle in the 3rd dimension using either electrophoretic or electroosmotic actuation.

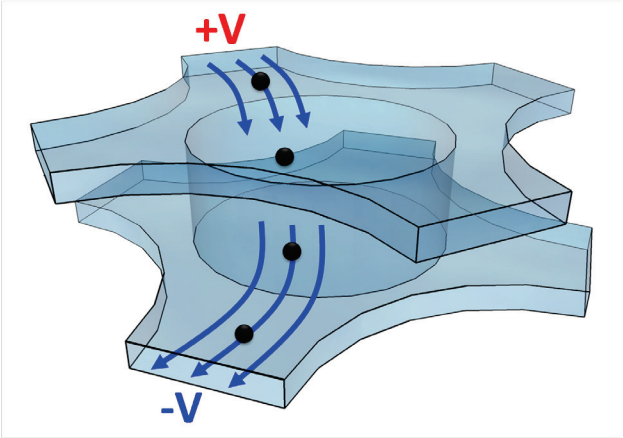

Figure 36: Device design for 3D electrokinetic tweezing. By applying voltages between channels in the top and bottom layer, an up or down electrophoretic force or electroosmotic flow component can be created at the particles location, in addition to the usual horizontal actuation.

Governing Equations

I first describe the physics of 3D electrophoretic particle actuation in a quiescent fluid (no electroosmotic flow yet). As is the case in planar control experiments, when a small charged particle sees an electrostatic force it quickly achieves an equilibrium electrophoretic velocity in the direction of the applied electric field at its location [125, 175, 176]. The EP velocity of the particle in an electrolyte can be characterized by its zeta potential ζp and is given by the Helmolz-Smoluchowski relation[47]

$$(23) \qquad \vec{v}_{ep} = \mu_{ep}\vec{E} = \frac{\varepsilon_0 \varepsilon_r \zeta_p}{\eta}\vec{E}$$

where μ_{ep} is the electrophoretic mobility of the particle, η is the dynamic viscosity of the liquid, εr is the relative dielectric constant of the liquid and $\varepsilon 0$ is the dielectric constant in vacuum. The 3D electric field $\vec{E} = -\nabla\Phi$ I create in the device is described by Laplace's equation subject to boundary conditions set by the voltages I apply at the 8 electrodes. Since Laplace's equation is linear I can write the net actuated electric field as a superposition of the fields produced by each electrode alone

$$(24) \qquad E(x,y,z,t) = -\sum_{i=1}^{8} \nabla\Phi_i(x,y,z)V_i(t)$$

where Φ_i denotes the electric potential when electrode i is turned on to a unit voltage (Vi = 1) and all the other electrodes are set to a zero voltage. The dynamics for a charged particle anywhere in the control chamber is now given by

$$(25)\,(\dot{x},\dot{y},\dot{z}) = \vec{v}_{ep} + \vec{w} = -\mu_{EP}\sum_{i=1}^{8} \nabla\Phi_i(x,y,z)V_i(t) + \vec{w}(t)\,.$$

Meaning, the particles next location is determined by the applied 3D electric field at its current location and by thermal Brownian noise[47] (which is given by dw=sqrt(kT/6πηa)) for a spherical particle of radius a, where k is the Boltzmann constant, T is the ambient temperature, dt is the time interval and η is the dynamic viscosity of water).

The physics for electroosmotic actuation of neutral particles is more complex but highlights the same essential features: the particle motion is linear in the applied voltages but the created velocity, including up and down actuation, varies nonlinearly with the particles location. In EO actuation, each solid/liquid interface has a thin Debye layer that moves under the applied electric field and drags the adjacent fluid along by viscous forces[47]. Thus the flow at each solid interface of the device follows the local electric field

$$(26) \qquad \vec{v}_{eo}\big|_I = \mu_{eo}\,\vec{E}\big|_I = \frac{\varepsilon_0 \varepsilon \xi_I}{4\pi\eta}\vec{E}\big|_I,$$

where v_{eo} is the fluid velocity at the liquid/solid interfaces (denoted by |I). Reynolds numbers in my devices are small (Re ~ 5 × 10-5) and so in the interior of the device the fluid flow is governed by Stokes equations[47]

$$(27) \qquad \nabla \cdot \vec{v}_{eo} = 0, \quad \eta \nabla^2 \vec{v}_{eo} = \nabla p\,.$$

Here p is the pressure and the two equations state the conservation of mass and momentum. Equation (26) above acts as a boundary condition for the Stokes equations where the electric field is as given previously in equation (24). For small chamber or slow control it is appropriate to neglect the momentum of the fluid (as is usually done[125]) but fluid (and even particle) momentum effects can be readily added into both the model and the control design. Since both the electric field and

Stokes equations are linear, I can still write the final fluid velocity as a superposition of EO velocities due to each electrode

$$(28) \qquad \vec{v}_{eo} = \sum_{i=1}^{8} \vec{v}_{eo}^{\,i}(x,y,z)\ V_i(t)$$

where $\vec{v}_{eo}^{\,i}(x,y,z)$ is the 3D EO flow velocity caused by turning on electrode i to a unit voltage and setting all the other voltages to zero. The dynamics of a neutral particle anywhere in the control region is therefore

$$(29)\ (\dot{x},\dot{y},\dot{z}) = \vec{v}_{eo} + \vec{w} = \sum_{i=1}^{8} \vec{v}_{eo}^{\,i}(x,y,z)\ V_i(t) + \vec{w}(t)$$

The motion of a charged particle in the presence of EO flow is the sum of EP and EO contributions

$$(30)\ (\dot{x},\dot{y},\dot{z}) = \sum_{i=1}^{n} \left[\vec{v}_{eo}^{\,i}(x,y,z) - \mu_{EP}\nabla\Phi_i(x,y,z)\right] V_i(t) + \vec{w}(t)$$

Equations (25),(29), or (30) are the mapping for charged or neutral particles, with or without electroosmotic flow, from electrode actuations to particle motion.

Figure 37 illustrates an electroosmotic and electrophoretic actuation mode for the case when all bottom electrodes are turned on positive and all top electrodes negative

Side-by-side, at each location, I show the velocity a particle would experience at that location.

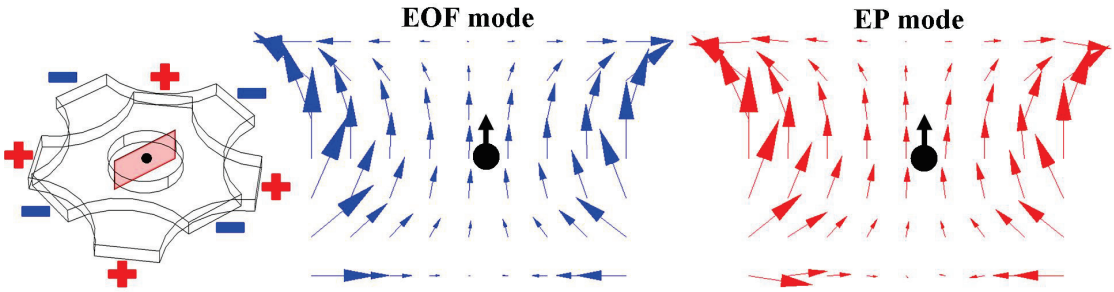

Figure 37: Basic mode of electrophoretic and electroosmotic velocities in a vertical plane. The created velocities are shown at each location for the shaded vertical plane and in particular for the central particle position marked in black.

Controller Design

Control design for 3D manipulation is mathematically identical to control design for 2D multi-particle control[82, 125] except that I now need to consider an additional actuation degree of freedom per particle to account for motion in the third dimension. For the location of each particle, I have a linear map (according to either equation (23) (for EP actuation) or equation (28) (for EO actuation) or the sum of them both) from the electrode voltages to the resulting 3-dimensional particle velocities. As before, this map is inverted by a pseudo-inverse (least squares) method to find the voltages that will best achieve the desired velocities and these are the voltages that the feedback controller applies at each time [82, 125, 165]. Simulation results are shown for a single particle being controlled by EO along a vertical infinity sign (Figure 38) and two particles being controlled at once by EP along two circles in orthogonal planes (Figure 39). Finally, control of two nanoscopic particles (where Brownian motion is significant) is shown along two orthogonal and self-intersecting circles, and

here I also show a case where the charge on the particles is not known to within ±50% (meaning, the control algorithm believes the particles have the wrong charge by 50%). As observed in experiments[82], the control is robust to this kind of error and manipulation is achieved to within 2 μm.

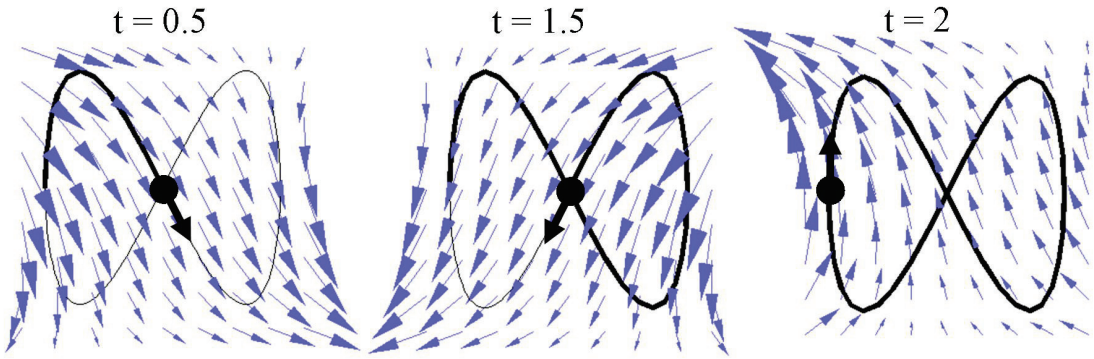

Figure 38: Control of one particle (black dot) on a vertical infinity path by EO actuation. The desired path of the particle is in thin black, the achieved path is in thick black, and the arrows show the EO velocity field at each time.

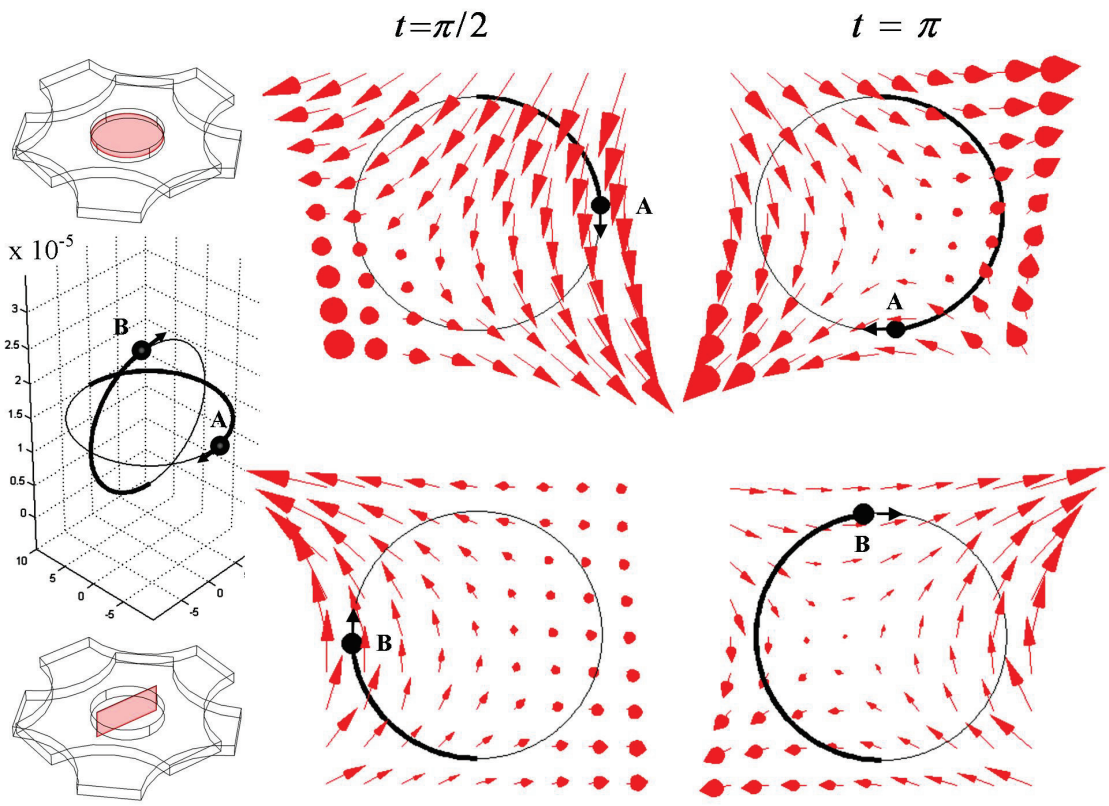

Figure 39: Two particles controlled simultaneously on two orthogonal circular paths. Horizontal and vertical paths are shown at the top and the bottom of the figure respectively. The desired path of the two particles (A and B) is in thin black, the achieved path is in thick black. The (red) arrows show the EP velocity field at each time. Arrows that show up as round dots show flow coming out of the plain.

Accuracy and Image Sensing

For manipulation of micro scale particles[82], control precision is set by the amount of Brownian motion and the resolution of the imaging which was ~ 1 μm in the xy plane as set by the pixel size of the camera. In Ropp et al.[133] we show EO manipulation of a 6nm diameter quantum dot on a trajectory to 120 nm accuracy and trapping to 45 nm accuracy, here we used sub-pixel averaging to sense xy position to 20 nm accuracy and a measure of defocusing to sense the z position. Recent results have shown an ability to measure xyz location of microscopic and nanoscopic objects to 20 nm [177] accuracy.

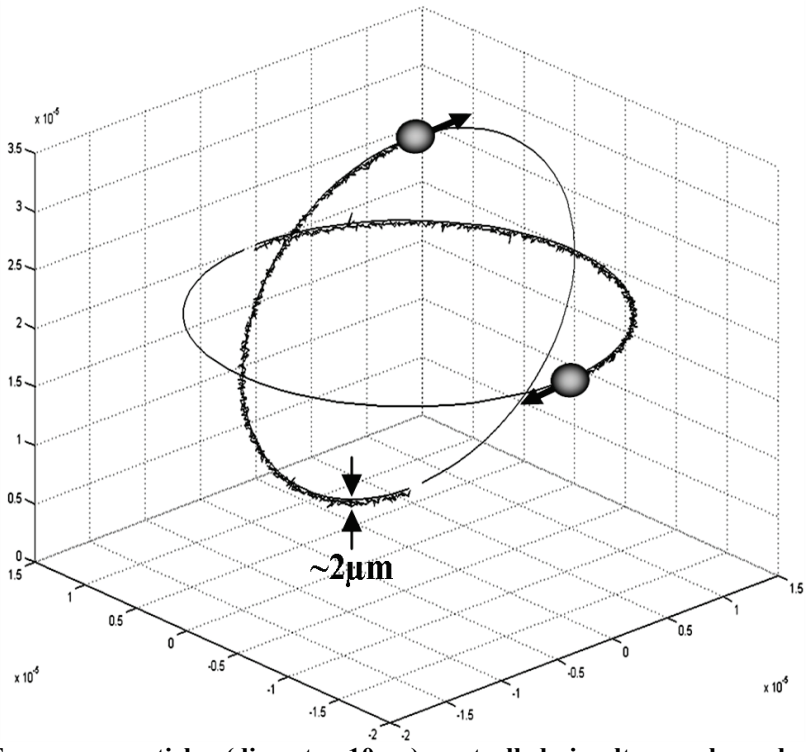

Figure 40: Two nano particles (diameter 10nm) controlled simultaneously under presence of Brownian motion and 50% charge mismatch.

Chapter 5: Magnetic Control of Ferro-Fluids

This chapter is concerned with precisely manipulating a ferrofluid by external magnets at a distance, and it considers the simplest typical example problem: control of a single droplet of ferrofluid in the plane by 4 electromagnets.

The following two sections describe a model of the magnetic force field and ferro fluid motion in the device, then discusses a simple control algorithm used to steer a ferro fluid droplet.

Model of Magnetic Fields and Ferro Fluid Motion

Magnetic fields are described by Maxwell's equations [124]. In this case, I am changing magnetic fields slowly (compared to radio frequencies) thus the magneto-static equations are appropriate. These are

$$\nabla \times \vec{H} = \vec{j} \tag{31}$$

$$\nabla \cdot \vec{B} = 0 \tag{32}$$

$$\vec{B} = \mu_o \left(\vec{H} + \vec{M} \right) = \mu_o \left(\vec{H} + \chi \vec{H} \right), \tag{33}$$

where $\vec{B}$ is the magnetic field [in Tesla], $\vec{H}$ is the magnetic intensity [Amperes/meter], $\vec{j}$ is the current density [A/m^2], $\vec{M}$ is the material magnetization [A/m], χ is the magnetic susceptibility, and $\mu_o = 4\,\pi \times 10^{-7}$ N/A^2 is the permeability of a vacuum. These equations hold true in vacuum and in materials (in air and liquid), for permanent magnets (magnetization $\vec{M} \neq 0$) and for electromagnets (current $\vec{j} \neq 0$). For the simple petri dish surrounded by four electromagnets configuration these equations can be readily solved using Comsol.

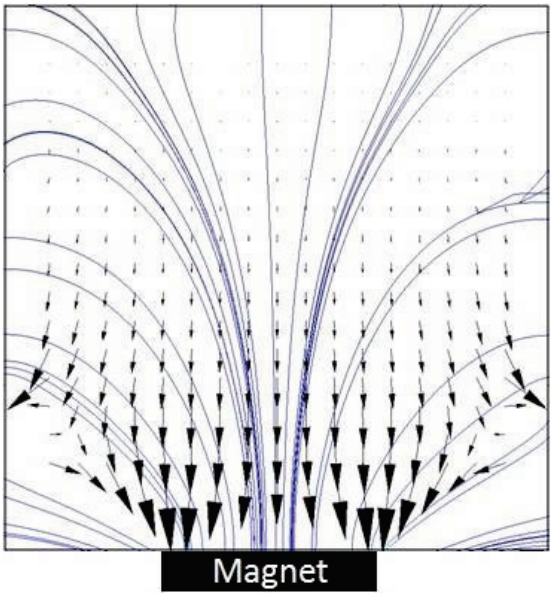

Figure 41: The magnetic field created by a single electromagnet magnet and the resulting force on a ferromagnetic particle at any location in the Petri dish. The resulting force directions, according to equation (34) below, are shown by the black arrows at each location. The magnetic field is represented by stream lines. The particle is always attracted to regions of highest magnetic field intensity, i.e. here to the right magnet.

The force on a single ferro-magnetic particle is then [119, 178-180]

$$\vec{F}_M = \frac{2\pi a^3}{3} \cdot \frac{\mu_0 \chi}{1+\chi/3} \nabla \left\| \vec{H} \right\|^2 = \frac{4\pi a^3}{3} \cdot \frac{\mu_0 \chi}{1+\chi/3} \left(\frac{\partial \vec{H}}{\partial \vec{x}} \right)^T \vec{H}, \qquad (34)$$

where a is the radius of the particle [m], ∇ is the gradient operator [with units 1/m], and $\partial \vec{H} / \partial \vec{x}$ is the Jacobian matrix of $\vec{H}$ with respect to the position vector $\vec{x} = (x, y, z)$. The first relation states that the force on a single particle is proportional to the gradient of the magnetic field intensity squared – i.e. a ferro-magnetic particle will always experience a force from low to high applied magnetic field; it will be attracted to any single on magnet regardless of its polarity. The second relation, which is obtained by applying the chain rule to the first one, is more common in the literature and clearly shows that a spatially varying magnetic field ($\partial \vec{H} / \partial \vec{x} \neq 0$) is required to create a magnetic force.

If the applied magnetic field is sufficient to magnetically saturate the particle, then $(\partial \vec{H} / \partial \vec{x})^T \vec{H}$ in equation 0 is modified to $(\partial \vec{H} / \partial \vec{x})^T \vec{M}_{sat}$ where $\vec{M}_{sat}$ is the saturated magnetization of the particle. Since $\vec{M}_{sat}$ lines up with $\vec{H}$, this does not change the direction of the force, only its size. In this case, the applied magnetic field never reaches the saturation limit of the particles and so equation (34) is correct as stated for any single magnetic particle.

When a magnetic force is applied, a single particle will accelerate in the direction of that force until it sees an equal and opposite fluid (Stokes) drag force. Since the Stokes force is [181-183]

$$\vec{F}_S = -6\pi a\,\eta\,\vec{v}, \tag{35}$$

where $\vec{v}$ is the velocity of the particle relative to the fluid. The nano-particles come suspended in a solution of deionized water. During experiments, I place them on top of a layer of high viscosity mineral oil (to keep the particles suspended and limit particle interactions with the bottom of the petri dish although the ferrofluid does still sink slowly and eventually does touch the petri dish surface). Thus, the relevant surrounding fluid is the mineral oil and it has a viscosity of η = 0.0576 kg /(m s). Now, setting equation (34) equal to equation (35) and solving for the velocity, I get

$$\vec{v}_{ss} = \frac{a^2}{9\eta}\frac{\mu_0\chi}{1+\chi/3}\,\nabla\left\|\vec{H}\right\|^2 = k\,\nabla\left\|\vec{H}\right\|^2, \tag{36}$$

where $k = a^2\mu_0\chi/9\eta(1+\chi/3)$ is the magnetic drift coefficient ($k \approx 1.6\times10^{-20}$ m^4 /A^2 s for the 100 nm diameter particles). This steady state velocity is achieved very quickly. For my particles it is predicted to be achieved in nanoseconds (the time constant is computed from Newton's second law by comparing the nanoparticle mass times acceleration versus the velocity dependent Stokes drag force).

I manipulate a single droplet of ferrofluid, which is composed of very many ferro-magnetic nano-particles held together by surface tension and magnetic interactions. The net force on the droplet, and hence its resulting velocity, is still in the direction of $\nabla \| \vec{H} \|^2$. The issue now is the magnitude of that velocity due to particle-to-particle interactions. Analogously to equation(36) , I define *k'* as the magnetic drift coefficient for the entire ferro-fluid droplet

$$\vec{v}_{droplet\_ss} = k' \nabla \left\| \vec{H} \right\|^2 \tag{37}$$

To quantify *k'* I measured droplet velocities under the action of a single magnet for two droplet volumes of 5 and 7.5 μL and compared them to theoretical predictions. The predicted motion best matched the observed motion, for the majority of the droplets trajectory, when $k' \approx 3.5 \times 10^{-13}$ m^4 /A^2 s and $k' \approx 4.2 \times 10^{-13}$ m^4 /A^2 s for the two droplet sizes respectively. However, the speed of the motion was under-predicted at the end of the trajectory when the droplet quickly snapped to the edge of the petri dish within the high-field region of the turned on external magnet.

Four scenarios were considered to understand and qualitatively explain the difference between the magnetic drift coefficient predicted for a single particle and that inferred for the ferrofluid droplet: 1) the motion of a single nanoparticle, 2) the motion of a chain of particles held together by magnetic particle-to-particle interactions, 3) the motion of an agglomerate of particles held together by magnetic particle-to-particle and chain-to-chain interactions, and 4) the motion of a rigid ferromagnetic bead the

size of the droplet (corresponding to the case where all the particles in the droplet are held together and all act as one mass). Overall, the third option best explained the observed *k'* values. Options 1 and 4 dramatically under-predicted and modestly over-predicted *k'* respectively. The force on single chains of particles (second option), including a chain of the entire length of the droplet, was also not enough to account for the measured *k'* values. Only the third option could explain the measurements and was consistent with prior studies on particle-to-particle interactions which show that particles can form chains and superstructures that dramatically increase the net magnetic force compared to the net viscous drag [184-188]. This explanation is also compatible with my finding that the magnetic drift coefficient varies and is greatest when the droplet is in the high field region near the on magnet: the higher magnetic field increases chaining and superstructures.

Note that control performance is insensitive to the value of *k'* – it continues to work even if I do not know *k*' accurately and do not account for its variation with the local magnetic field strength. This is because the control always applies a velocity to move the droplet from where it is *towards* where it should be – it only needs to set the direction correctly, the magnitude of the velocity is not critically important since another correction will occur at the next time step. Further, the variation in *k'* is only appreciable at the edges of the petri dish closest to the external magnets; *k'* is close to constant for the majority of the petri dish interior.

Based on the above, I now state the motion of the droplet as a function of the actuation of the four magnets – this is information I need to know in order to design the magnets control law. Let $\vec{H}_1(x,y)$, $\vec{H}_2(x,y)$, $\vec{H}_3(x,y)$, and $\vec{H}_4(x,y)$ be the magnetic fields in the *xy* plane, across the petri dish, when each magnet is turned on with a 10 Volts. The first magnetic field $\vec{H}_1(x,y)$ is shown in Figure 41 as computed by Comsol, the other three $\vec{H}_k$ are 90 degree rotations of $\vec{H}_1$. Let u_1, u_2, u_3 and u_4 be the applied voltage of each of the four magnets. Then, by the linearity of the magneto-static equations, the time-varying magnetic field that I apply is given by

$$\vec{H}(x,y,t) = u_1(t)\vec{H}_1(x,y) + u_2(t)\vec{H}_2(x,y) + u_3(t)\vec{H}_3(x,y) + u_4(t)\vec{H}_4(x,y) \quad (38)$$

Together with equation (37) this is the model for droplet motion as a function of the applied control. It is a nonlinear differential equation which depend on the droplets location since the magnetic field applied by each magnet varies in space across the petri dish. The dynamics is *quadratic* in the current control vector $\bar{u}$ because the force depends on the gradient of the magnetic field *squared*. This means the droplets motion depends on both single magnet actuation and on $u_i u_j$ cross terms – the velocity created by turning on two magnets at the same time is not the sum of the velocities created by each magnet alone. My control is explicitly designed to account for this quadratic nature of the dynamics.

Ferro Fluid Steering Control Algorithms

My control operates by continuously directing the ferrofluid droplet from where it is measured to be towards where it should go (Figure 42). With this approach I can both hold the ferrofluid at a target location (the control continually puts it back) and I can steer the droplet along desired trajectories (the control is always moving the droplet towards its next desired location).

At each time I cycle through a set of pre-computed velocity modes (Figure 43) and compute the displacement error vector between the droplets desired and resulting position $\vec{e} = \vec{r}_f - \vec{r}_{k+1}$ and I actuate the four magnets to create a droplet velocity $\dot{\vec{r}} = \vec{r}_{k+1} - \vec{r}_k$ that minimizes this error vector so that the droplet moves towards its target location. The task of the control algorithm is to decide how to best actuate the four magnets to achieve the needed velocity to minimize the error vector.

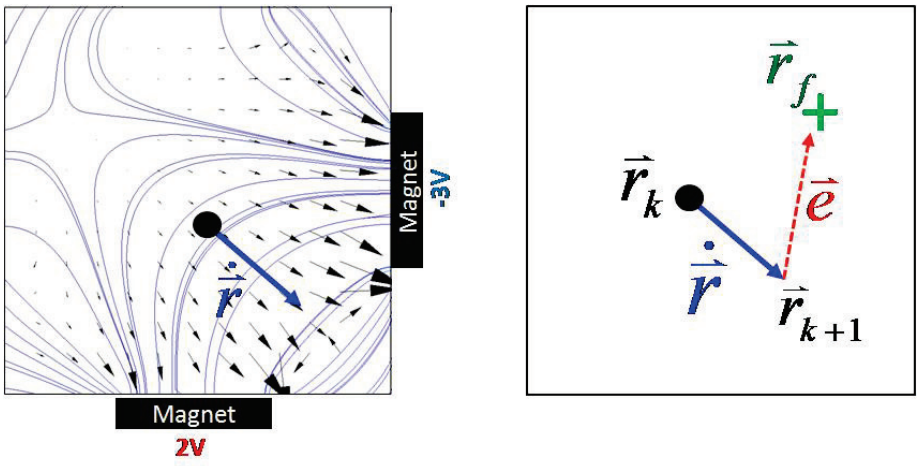

Figure 42: This figure shows the simulated motion direction and the resulting error if I actuate the 2nd electromagnets with -3 Volts and the 3rd electromagnets with +2 Volts simultaneously.

The momentum of the ferrofluid is negligible. This means the droplet has no ability to continue to travel if there is no applied force and it reacts immediately to any newly applied force. Thus the droplets velocity is always in the direction of the magnetic force that I apply (this further means the droplet can execute sharp turns as I show in the results section). The task of the controller to create the needed droplet velocity can be phrased as creating a magnetic force in the right direction at the droplets current location: the two only differ by a constant c, i.e. $\vec{v} = c\vec{F}_{mag}$. Although the droplet has no momentum, the electromagnets do. Their actuation cannot be changed sharply (due to coil charging time-constants) and my control takes this into account and compensates for it.

The task of achieving a desired droplet velocity $\vec{v} = (v_x, v_y)$ is to cycle through a set of pre-computed velocity modes and choosing the resulting velocity (at the droplets position) that brings the droplet closer to the desired position.

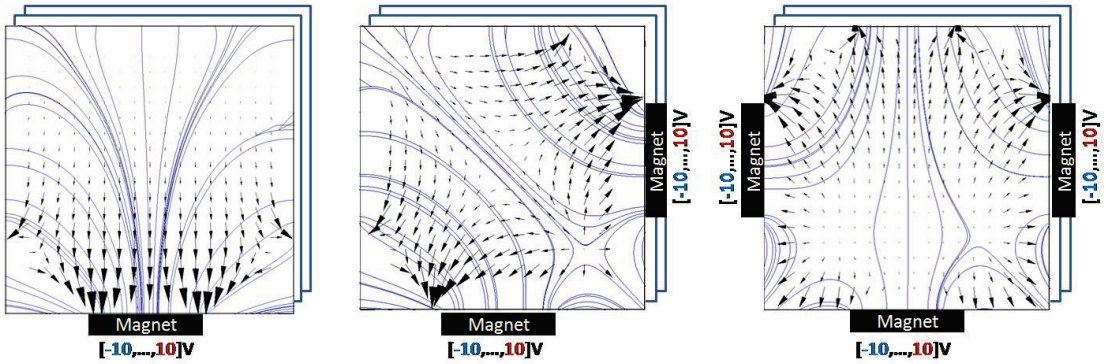

Figure 43: This figure illustrates the set (database) of pre-computed force field modes resulting from the electromagnets. The magnetic force on the ferrofluid is represented by arrows and the magnetic field is represented by stream lines. On the left is the set of partial modes for a single magnet actuated from -10 to 10 volts and in the middle and on the right is the set modes for partial combinations of two and three magnets individually actuated from -10 to 10 volts. The modes that are visible in the figure were produced by actuating the magnets with 1V.

This is equivalent to minimizing the objective function

$$J = \| \vec{e} \|^2 \tag{39}$$

Therefore, the control problem can be formulated in terms of minimizing (39) subject to the droplet dynamics(37) . My approach to this optimization problem is to first identify a parametric family of all solutions as illustrated in Figure 43 (the constraint space), then explicitly express the cost function (39) in terms of the parameters of this family, and finally minimize the cost with respect to the parameters.

At any specific (x, y) droplet location, for each desired velocity $\vec{v} = (v_x, v_y)$, the constraint space is a two-dimensional surface in the four-dimensional space of the magnets – all points on this surface create droplet velocities.

The nature of the resulting control algorithm is illustrated in Figure 42 and Figure 43. It minimizes the amount of control effort used and explicitly accounts for the nonlinear nature of the magnetic force. The parameters used for generating these graphs are those of the experimental test-bed. To reduce problem size, I chose only two dominant modes for the optimization procedure. These modes are shown in the next figure.

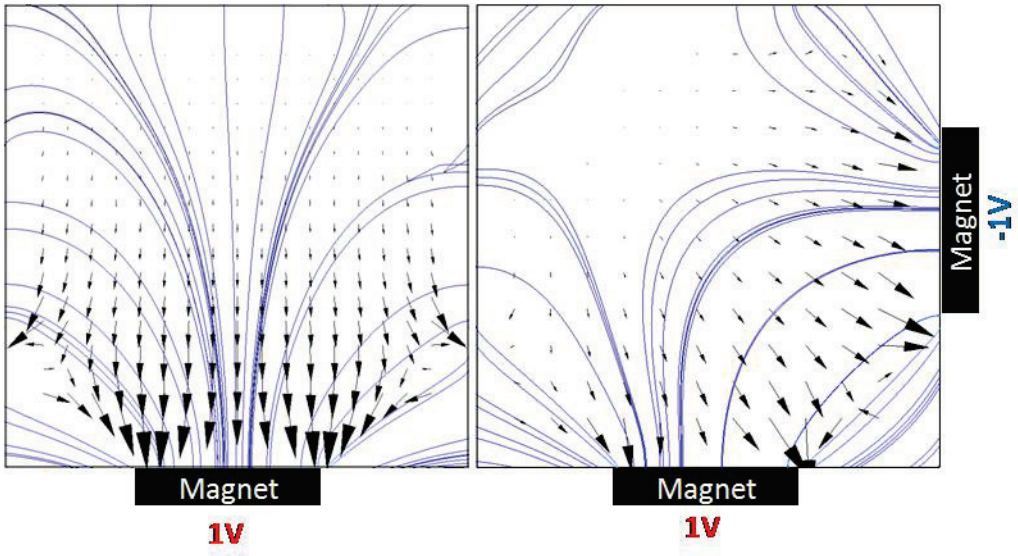

Figure 44: Figure shows the two chosen modes for optimization. These modes can be rotated to achieve motion that consists of movements of multiples of 45deg and the forces can be increased or decreased by changing the actuation voltage.

Experimental Design and Methods

This section describes the details of the experimental setup. There are four major components, the materials (petri dish, ferrofluid, and liquid medium), the camera, the control algorithm software and hardware, and the electromagnets.

Materials Used

I used a commercially available ferrofluid (Chemicell). The ferrofluid contains 8% by volume of 100 nm diameter multi-core particles. Each particle contains a 70-75 nm in diameter starch encapsulated magnetite core that consists of a fused cluster of single-domain crystals. These magnetic particles were chosen for their size and high magnetic susceptibility (χ~72) which allowed them to be actuated at up to 4 cm away from the moderate strength (0.13 Tesla at magnet faces), inexpensive ($57.51), and commercially available (E-28-150 Tubular Electro-magnet, Solenoidcity) electromagnets. A future experimental platform with strong magnets is currently under construction and will be able to manipulate a ferrofluid at a greater distance from the magnets.

A 1.5 inch (3.8 cm) diameter Petri-dish (Fisher Scientific) was used to contain the ferrofluid. The petri dish was filled with a high viscosity mineral oil (Heavy Viscosity Mineral Oil, CQ Concepts), which served as a suspending medium for the droplet (as done in [189]). I used mineral oil because of its density, viscosity and surface tension properties which caused the ferrofluid (which comes in the form of magnetic particles suspended in DI water) to remain as a single droplet and significantly reduces sticking of the ferrofluid to the petri dish surface.

Camera and Real-Time Ferrofluid Position Detection Software

The vision system consisted of a lens, camera, external lighting, and in-house imaging software. The camera (Guppy F-033B/C, 1st Vision) operated at 58 frames-per-second, had 656 by 494 color pixels, and was equiped with a 6 mm lens (1st Vision Inc.). A 56-LEDs ring light (Microscope Ring Light, AmScope) was mounted above the petri dish, around the camera, to create a shadow-free illumination of the ferrofluid.

The image software was coded in Matlab version 2007b, with a data acquisition toolbox (version 2.11) and an image acquisition toolbox (version 3.0), and ran on a Dell computer (2.4GHz Intel Core2 Duo CPU). It allowed accurate real-time tracking and velocity estimation of the ferrofluid droplet or blob. This was achieved by combining an algorithm that finds all blobs in an image frame and an algorithm that tracks a blob of interest among other visual features. (It is possible for me to track one droplet through a field of many others [82] by using a Kalman tracking filter but this is not necessary for the results presented in this paper.) Each image frame is transferred from the camera to Matlab through a firewire (IEEE 1394) interface. The image is threshold, filtered, and operated on by an algorithm that finds the center of the ferrofluid droplet. This method finds and tracks the position of the ferrofluid droplet in less than 20 ms and passes that position to the control algorithm. The vision tracking is completely automated and does not require any user input during control operation.

Control Algorithm Implementation Hardware and Software

Like the vision code, the control algorithm is written in Matlab and runs on the same computer as the droplet image tracking. It finds the optimal control magnet voltage actuation at each time by solving the mathematics described above, and it takes 66.7 milliseconds to do so (hence the feedback loop runs at 15 Hz). This rate can be improved (e.g. by using C or MEX files to do the evaluation) and that will allow faster control of the ferrofluid in the future.

Output from the computer is used to command the four electromagnets. The computer is connected to a digital-to-analog signal converter (DAQ USB-3101, Measurement Computing) which connects to four linear DC servo amplifiers (MSE421, Mclennan). The latter allows me to increase the low current, low voltage control signal (0-20 mA, ± 10 volts) generated by the digital-to-analog signal converter to the higher current, higher voltage (0-1 A, ± 28 volts) output signal required to power the four electromagnets.

Electromagnets

I used four small, inexpensive, and commercially available electromagnets to achieve the ferrofluid control results in this paper. These electromagnets (E-28-150 Tubular Electromagnet, Solenoidcity, $57.51 each) have a length of 71.4 mm and a diameter of 38.1 mm each. They contain a 14 mm diameter iron core, their internal resistance

was measured to be 43 Ω, and they operate at 28 volts while drawing 0.651 amperes and producing 24 watts of heat. The strength of the magnets was unrated by the manufacturer but I measured the magnetic field distribution around these magnets with a 4.3 mm wide Hall probe (DC Magnetometer (Gauss), AlphaLab Inc.) on a square grid in the petri dish (with a placement accuracy of ~ 1 mm) and a field measurement accuracy of ± 2 % (as rated by the manufacturer) and verified that it matched the simulation data shown in Figure 41. I found that these magnets generated a magnetic field of approximately 0.13 Tesla at their faces, 0.20 Tesla at their corners, and ~0.003 Tesla at a distance of 3.7 cm thus yielding a magnetic field of approximately ~0.016 Tesla at the center of the petri dish. During longer experimental runs, the magnets were cooled by rigid foam ice packs (Fisher Scientific) that were packed around them.

Results

I tested the magnetic control for a variety of ferrofluid droplet sizes and desired trajectory shapes and speeds. The promising droplet volume was 15 μL, which, under the action of surface tension, correspond to droplet radii of 1.2 mm. I also attempted control of a 150 μL droplet (3.3 mm radius) but this droplet was too large to be held together by surface tension during control and it broke apart. Trajectories were varied from the simplest to more complicated. The simplest task was to control the droplet in a straight line from its current to a desired location (to the center and to the outside of the petri dish). Figure 45 shows control of a single ferrofluid droplet along a 'UMD' path, for the University of Maryland.

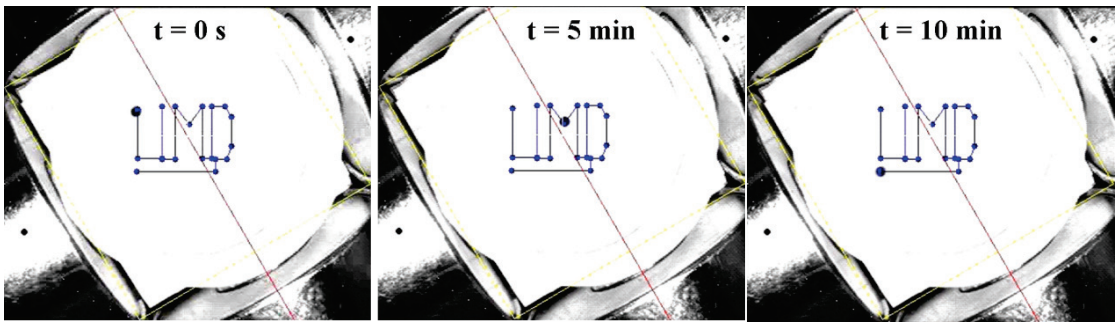

Figure 45: Control of a medium size 15 μL (1.2 mm radius) ferrofluid droplet slowly along a UMD path.

Above I have shown optimal control of a single droplet to 4 cm depth using four medium-strength (0.13 Tesla at their face), small, commercially available and inexpensive magnets. Based on the mathematical analysis above, using scaled-up stronger (2 Tesla), larger (30 cm length, 30 cm coil diameter, 12 cm core diameter) electromagnets, will enable the same control forces on a single drop of ferrofluid at a depth of half a meter. Advanced magnets with optimally matched materials and shaped coils and cores, as presented in [190-192], could enable even stronger and deeper magnetic control forces.

Chapter 6: Conclusion and Outlook

Feedback control allows simple micro-fluidic devices to execute sophisticated tasks. I demonstrate experimentally that vision-based optimal feedback control allows a multi channel PDMS device to steer single and multiple particles (polystyrene beads, biological cells, swimming microbes and quantum dots) along arbitrary paths with nanometer precision. At each time instant a vision system identifies the current locations of the particles, a control algorithm determines the actuator voltages that will create a fluid flow (for electroosmosis actuation) or an electric field (for electrophoretic actuation) to move the neutral or charged particles from their current locations toward their next desired positions, and the necessary flow or electric field is then created by voltage actuation. It permits the steering of any visible particles (neutral particles are carried by the flow, charged particles are also actuated electrophoretically), for neutral or almost neutral particles the method is non-invasive because it does not actuate the particles directly but instead moves them by transporting the surrounding medium.

I have shown the ability to individually select, characterize, and position single nanoscopic objects with nanometer accuracy. This capability could enable integration of single quantum dots, or other visualizable nano-scale objects, with photonic structures and enable the development of novel nanophotonic devices and sensors. Additional techniques providing immobilization of objects via surface chemistry [160] or cross linking polymerization [161] could be further incorporated with the

procedure demonstrated here for scalable fabrication of integrated devices that require the precise placement of preselected nanoparticles with desired properties.

I have shown manipulation of multiple particles simultaneously by creating the right actuation at the right location by precisely combining fluid actuation modes. Further, I developed optimal path planning tools to manipulate particles with minimal voltages (power) and miniaturized the imaging and control system to permit laser tweezers capabilities in a handheld format.

The next major issue was to control in the third (vertical) dimension. I invented a novel method that extends flow control capabilities to the third dimension by creating a multilayer system that has up and down flow modes in addition to horizontal ones. This method can achieve accurate full 3D positioning of single or multiple particle (micro, nano, charged or neutral) and presents a valuable tool for molecular biology, i.e. to monitor and manipulate protein confirmation.

In the last part of the thesis I have shown manipulation of ferrofluids by magnetic fields, with a view toward controlling therapeutic magnetic nano particles in patients. I considered the simplest archetypical example problem: control of a single droplet of ferrofluid in the plane by 4 electromagnets. The control algorithm explicitly takes into account the nonlinear pull-only nature of the magnetic actuation, it is designed for both the quadratic dependence of the magnetic force on the actuated strength of each magnet and the sharp drop off of force with distance from each magnet.

The theoretical and experimental results in this thesis are a key next step towards my broader effort of precision control of magnetic drug delivery to deeper tissue targets [117-119, 177]. It was necessary to first understand and overcome the experimental challenges for control of a single droplet of ferrofluid. Results here will allows me to move towards using stronger magnets for deeper control of a single droplet, as well as to begin to experimentally implement the theoretical and numerical results developed in [119] which show time-averaged focusing of a distributed ferrofluid, a fluid not held together by surface tension, to internal targets between magnets.

In conclusion, I have shown frameworks for electrokinetic and electromagnetic manipulation of micro and nano scaled objects to nanometer precision.

Chapter 7: Intellectual Contributions

Several graduate students in Dr. Benjamin Shapiro's research group have contributed to these projects. This section outlines my intellectual contributions within a larger multi-disciplinary team.

I developed a system to manipulate single and multiple micro scaled and nano scaled objects, such as biological cells and quantum dots, by flow control. To manipulate living organisms I had to address cell viability during manipulation. Cell viability was significantly improved by optimizing methods to maintain physiological conditions.

To control nano scaled objects, such as quantum dots, to nm accuracy I had to address diffusion and imaging errors. Diffusion was reduced by the right choice of chemistry that significantly increased the viscosity of the fluid but kept quantum dots stable and suspended. Imaging accuracy was achieved to sub wavelength of light resolution by using laser illumination and by exploiting sub pixel averaging algorithms.

Controlling multiple particles simultaneously is difficult because the flow used to move one particle also moves all the others. It is not possible to actuate each particle individually. I create the right actuation at the right location by precisely combining fluid actuation modes.

As particles approach each other, actuation voltages can increase dramatically. I developed optimal path planning tools to manipulate particles with minimal voltages

(power). The next major issue was control in the third (vertical) dimension. I invented a novel method that extends flow control capabilities to the third dimension in a multilayer system that has up and down flow modes in addition to horizontal ones.

I also manipulated particles by magnetic fields, with a view toward controlling therapeutic magnetic nano particles in patients. The forces on magnetic particles are nonlinear with respect to the actuation. I developed a model based optimal control algorithm that partially inverts this nonlinearity and an experimental platform for ferrofluid control. Later, in collaboration with Arash Komaee, we developed and demonstrated improved control algorithms that effectively and precisely invert this nonlinearity.

Authors Contribution to the Research within the Larger Team

The concept of microfluidic particle control was first suggested by Dr. Benjamin Shapiro in 2002. The author independently designed an experimental setup and together with Michael Armani demonstrated the first experimental particle steering in 2003 [1]. The author designed a system of multiple channels feeding into a planar control region, improved and applied control algorithms previously developed by Satej Chaudhary to demonstrate multiple particle steering in 2005. The author further miniaturized the system and successfully demonstrated particle steering in a hand held device at conferences.

Both, the author and Satej, led a thorough investigation into the factors that prevented demonstration of steering more than 3 particles in experiments. The author suggested optimizing the device to increase the electric field in the control area and to develop path planning methods. To demonstrate steering of multiple [this is the case for 2 and more particles] particles it was imperative to carefully design the paths. Improperly designed paths would lead to actuator saturation and consequently loss of control. In the process the author worked on developing power optimal path planning methods (2005). Satej adopted the concept in 2007 and achieved a complementary approach. This thesis presents the research on power optimal path planning carried out by the author. At this stage, Zach Cummins became involved in the project and during his overlap with the author his contribution was on improving the vision system and on creating an improved matlab graphical user interface. The author, Satej and Zach then demonstrated steering of five particles in an experiment.

The author developed a Nature protocol to make this technology available to other fields (biology, biophysics and photonics). Together with Zach he demonstrated steering of living cells, bacteria and swimming microbes.

In 2007, the author led a team of interdisciplinary students (Sina Sahand and Rakesh Kumar) to demonstrate steering of a single quantum dot to micro meter accuracy.
Later, Chad Ropp and Zach joined the team. The team extended and improved the experimental setup to achieve positioning to nano meter accuracy.

In all previous applications steering was restricted to the two dimensional space. The author invented a novel method that allows control of micro and nano particles in full three dimensional spaces by flow control. This technology allows monitoring of protein conformation and three dimensional assemblies of nano structures.

In 2006, Benjamin Shapiro and the author started a new project for magnetic guidance of nano particles to deep tissue tumors. The author contributed to the concept and to writing a NIH exploratory research grant proposal (R21). He led a team of students (John Lin, Alek Nacev, Zach Cummins) to design a magnetic control test bed for visual feedback control of ferro fluids. The author independently designed a control algorithm and together with the team demonstrated model based magnetic control of a ferro fluid droplet in a plane.

Bibliography

1. Ashkin, A., *History of Optical Trapping and Manipulation of Small-Neutral Particles, Atoms, and Molecules.* IEEE Journal on Selected Topics in Quantum Electronics, 2000. **6**(6): p. 841-856.
2. Curtis, J.E., B.A. Koss, and D.G. Grier, *Dynamic holographic optical tweezers.* Optics Communications, 2002. **207**(1-6): p. 169-75.
3. Grier, D.G., *A revolution in optical manipulation.* NAture, 2003. **424**(810-816).
4. Chiou, P.Y., Ohta, A. T., et al., *Massively parallel manipulation of single cells and microparticles using optical images.* Nature, 2005. **436**: p. 370-372.
5. Hughes, M.P., *Strategies for dielectrophoretic separation in laboratory-on-a-chip systems.* Electrophoresis, 2002. **23**: p. 2569-2582.
6. Muller, T.e.a., *Trapping of micrometre and sub-micrometre particles by high-frequency electric fields and hydrodynamic forces.* J. Phys. D: Appl. Phys., 1996. **29**: p. 340-349.
7. Pethig, R., Talary, M. S. , et al., *Enhancing traveling-wave dielectrophoresis with signal superposition.* IEEE Eng. Med. Biol. Mag., 2003. **22**: p. 43-50.
8. Morgan, H., Green, N. G., et al., *Large-area travelling-wave dielectrophoresis particle separator.* J. Micromech. Microeng., 1997. **7**(2): p. 65-70.
9. Hertz, H.M., *-wave acoustic trap for nonintrusive positioning of microparticles.* J. Appl. Phys., 1995. **78**: p. 4845-4849.
10. Lee, H., T.P. Hunt, and R.M. Westervelt. *Magnetic and Electric Manipulation of a Single Cell in Fluid*. in *Material Research Society Symposium*. 2004: Materials Research Society.
11. Fukuta, Y., et al. *A MEMS array for pneumatic conveyor and its control based on distributed systems*. in *Micro-Electro-Mechanical Systems (MEMS)*. 2005. Miami, Florida.
12. Cohen, A.E., *Control of nanoparticles with arbitrary two-dimensional force fields.* Phys. Rev. Lett., 2005. **94**: p. 118102.
13. Cohen, A.E. and W.E. Moerner, *Method for Trapping and Manipulating Nanoscale Objects in Solution.* Appl. Phys. Lett., 2005. **86**: p. 093109.
14. Hoogenboom, J.P., et al., *Patterning surfaces with colloidal particles using optical tweezers.* Applied Physics Letters, 2002. **80**(25): p. 4828-4830.
15. Armani, M., et al. *Using Feedback Control and Micro-Fluidics to Steer Individual Particles*. in *18th IEEE International Conference on Micro Electro Mechanical Systems*. 2005. Miami, Florida.
16. Chaudhary, S. and B. Shapiro, *Arbitrary Steering of Multiple Particles at Once in an Electroosmotically Driven Microfluidic System.* IEEE Transactions on Control Systems Technology, 2005. **accepted**.

17. Doyle, J.C., B.A. Francis, and A.R. Tannenbaum, *Feedback Control Theory*. 1992, New York, NY: Macmillan Publishing Company.
18. Murray, R.M., et al., *Control in an Information Rich World*. 2002, Air Force Office of Scientific Research (AFOSR).
19. Terreros, D.A. and J.J. Grantham, *Marshall Barber and the origins of micropipette methods.* Am J Physiol Renal Physiol, 1982. **242**(3): p. F293-296-F293-296.
20. Sagvolden, G., et al., *Cell adhesion force microscopy.* Proceedings of the National Academy of Sciences of the United States of America, 1999. **96**(2): p. 471-476.
21. Hulsen, H., T. Truper, and S. Fatikow. *Control system for the automatic handling of biological cells with mobile microrobots*. in *American Control Conference, 2004. Proceedings of the 2004*. 2004.
22. Chronis, N. and L.P. Lee, *Electrothermally Activated SU-8 Microgripper for Single Cell Manipulation in Solution.* Microelectromechanical Systems, Journal of, 2005. **14**(4): p. 857-863.
23. Ashkin, A., J.M. Dziedzic, and T. Yamane, *Optical trapping and manipulation of single cells using infrared laser beams.* Nature, 1987. **330**(6150): p. 769-771.
24. Qian, F., et al., *Combining optical tweezers and patch clamp for studies of cell membrane electromechanics.* Review of Scientific Instruments, 2004. **75**(9): p. 2937-2942.
25. Lee, W.M., et al., *Construction and calibration of an optical trap on a fluorescence optical microscope.* Nat. Protocols, 2007. **2**(12): p. 3226-3238.
26. Sheetz, M.P., *Laser Tweezers in Cell Biology*. Methods in Cell Biology. Vol. 55. 1998: Academic Press.
27. Shah, G.J., et al., *EWOD-driven droplet microfluidic device integrated with optoelectronic tweezers as an automated platform for cellular isolation and analysis.* Lab on a Chip, 2009. **9**(12): p. 1732-1739.
28. Valley, J.K., et al., *Parallel single-cell light-induced electroporation and dielectrophoretic manipulation.* Lab on a Chip, 2009. **9**(12): p. 1714-1720.
29. Thomas, R.S., H. Morgan, and N.G. Green, *Negative DEP traps for single cell immobilisation.* Lab on a Chip, 2009. **9**(11): p. 1534-1540.
30. Hunt, T. and R. Westervelt, *Dielectrophoresis tweezers for single cell manipulation.* Biomedical Microdevices, 2006. **8**(3): p. 227-230.
31. Glynn, J.R., et al., *Capillary Electrophoresis Measurements of Electrophoretic Mobility for Colloidal Particles of Biological Interest.* Appl Environ Microbiol, 1998. **64**(7): p. 2572-7.
32. Lytle, D.A., et al., *Electrophoretic mobilities of Escherichia coli O157:H7 and wild-type Escherichia coli strains.* Appl Environ Microbiol, 1999. **65**(7): p. 3222-5.
33. Kremser, L., Blaas, D., Kenndler, E., *Capillary electrophoresis of biological particles: viruses, bacteria, and eukaryotic cells.* Electrophoresis, 2004. **25**(14): p. 2282-91.

34. Alenghat, F.J., et al., *Analysis of Cell Mechanics in Single Vinculin-Deficient Cells Using a Magnetic Tweezer.* Biochemical and Biophysical Research Communications, 2000. **277**(1): p. 93-99.
35. Yan, J., D. Skoko, and J.F. Marko, *Near-field-magnetic-tweezer manipulation of single DNA molecules.* Physical Review E, 2004. **70**(1): p. 011905-011905.
36. Vries, A.H.B.d., et al., *Micro Magnetic Tweezers for Nanomanipulation Inside Live Cells.* Biophysical Journal, 2005. **88**(3): p. 2137-2144.
37. Lee, J. and K.K. Shung, *Effect of ultrasonic attenuation on the feasibility of acoustic tweezers.* Ultrasound in Medicine & Biology, 2006. **32**(10): p. 1575-1583.
38. Junru, W., *Acoustical tweezers.* The Journal of the Acoustical Society of America, 1991. **89**(5): p. 2140-2143.
39. Zhang, H. and K.-K. Liu, *Optical tweezers for single cells.* Journal of the Royal Society, Interface / the Royal Society. **5**(24): p. 671-690.
40. Eriksson, E.O., et al., *Automated focusing of nuclei for timelapse experiments on single cells usingholographic optical tweezers.* Optics Express, 2009. **17**(7): p. 5585-5594.
41. Zhang, H. and K.-K. Liu, *Optical tweezers for single cells.* Journal of the Royal Society, Interface / the Royal Society, 2008. **5**(24): p. 671-690.
42. Mirsaidov, U., et al., *Optimal optical trap for bacterial viability.* Physical Review. E, Statistical, Nonlinear, and Soft Matter Physics, 2008. **78**(2 Pt 1): p. 021910-021910.
43. König, K., et al., *Effects of ultraviolet exposure and near infrared laser tweezers on human spermatozoa.* Human Reproduction (Oxford, England), 1996. **11**(10): p. 2162-2164.
44. Neuman, et al., *Characterization of photodamage to escherichia coli in optical traps.* Biophysical Journal, 1999. **77**(5): p. 2856-63.
45. Neuman, K.C. and A. Nagy, *Single-molecule force spectroscopy: optical tweezers, magnetic tweezers and atomic force microscopy.* Nat Meth, 2008. **5**(6): p. 491-505.
46. Hiemenz, P.C. and R. Rajagopalan, *Principles of Colloid and Surface Chemistry*. 3 ed. 1997, New York, Basel, Hong Kong: Marcel Dekker, Inc.
47. Probstein, R.F., *Physicochemical Hydrodynamics: An Introduction*. 2003: Wiley-Interscience.
48. Armani, M.D., et al., *Using feedback control of microflows to independently steer multiple particles.* Journal of Microelectromechanical Systems, 2006. **15**(4): p. 945-956.
49. Alex, e.P. Fields, and A.E. Cohen, *A Flexible Anti-Brownian Electrokinetic (ABEL) Trap for Single-Molecule Immobilization in Solution.* Biophysical Journal, 2009. **96**(3): p. 288a-288a.
50. Leclerc, E., Y. Sakai, and T. Fujii, *Cell Culture in 3-Dimensional Microfluidic Structure of PDMS (polydimethylsiloxane).* Biomedical Microdevices, 2003. **5**(2): p. 109-114.
51. Tourovskaia, A., X. Figueroa-Masot, and A. Folch, *Long-term microfluidic cultures of myotube microarrays for high-throughput focal stimulation.* Nat. Protocols, 2006. **1**(3): p. 1092-1104.

52. Park, J.W., et al., *Microfluidic culture platform for neuroscience research.* Nat. Protocols, 2006. **1**(4): p. 2128-2136.
53. McDonald, J.C., et al., *Fabrication of microfluidic systems in poly(dimethylsiloxane).* Electrophoresis, 2000. **21**(1): p. 27-40.
54. Walker, G.M., M.S. Ozers, and D.J. Beebe, *Insect Cell Culture in Microfluidic Channels.* Biomedical Microdevices, 2002. **4**(3): p. 161-166.
55. *Microfluidic Foundry :: California Institute of Technology*. [cited; Available from: http://kni.caltech.edu/foundry/index.html.
56. *Stanford University Microfluidics Foundry*. [cited; Available from: http://thebigone.stanford.edu/foundry/.
57. Duffy, D.C., et al., *Rapid Prototyping of Microfluidic Systems in Poly(dimethylsiloxane).* Anal Chem, 1998. **70**(23): p. 4974-4984.
58. Ebersole, R.C. and R.M. McCormick, *Separation and Isolation of Viable Bacteria by Capillary Zone Electrophoresis.* Nat Biotech, 1993. **11**(11): p. 1278-1282.
59. Zimmermann, U., *Electrical breakdown, electropermeabilization and electrofusion.* Reviews of Physiology, Biochemistry and Pharmacology, 1986. **105**: p. 176-256.
60. Weaver, J.C. and Y.A. Chizmadzhev, *Theory of electroporation: A review.* Bioelectrochemistry and Bioenergetics, 1996. **41**(2): p. 135-160.
61. Chaudhary, S. and B. Shapiro, *Arbitrary steering of multiple particles independently in an electro-osmotically driven microfluidic system.* Control Systems Technology, IEEE Transactions on, 2006. **14**(4): p. 669-680.
62. Badolato, A., et al., *Deterministic Coupling of Single Quantum Dots to Single Nanocavity Modes.* Science. **308**(5725): p. 1158-1161.
63. Hennessy, K., et al., *Quantum nature of a strongly coupled single quantum dot-cavity system.* Nature. **445**(7130): p. 896-899.
64. Englund, D., et al., *Controlling cavity reflectivity with a single quantum dot.* Nature. **450**(7171): p. 857-861.
65. Akimov, A.V., et al., *Generation of single optical plasmons in metallic nanowires coupled to quantum dots.* Nature. **450**(7168): p. 402-406.
66. Chang, D.E., et al., *A single-photon transistor using nanoscale surface plasmons.* Nat Phys. **3**(11): p. 807-812.
67. Waks, E. and J. Vuckovic, *Dipole Induced Transparency in Drop-Filter Cavity-Waveguide Systems.* Physical Review Letters, 2006. **96**(15): p. 153601-4.
68. Medintz, I.L., et al., *Quantum dot bioconjugates for imaging, labelling and sensing.* Nature Materials, 2005. **4**(6): p. 435-446.
69. Jauffred, L., A.C. Richardson, and L.B. Oddershede, *Three-Dimensional Optical Control of Individual Quantum Dots.* Nano Letters, 2008. **8**(10): p. 3376-3380.
70. Pei-Yu, C., et al., *Light-Actuated AC Electroosmosis for Nanoparticle Manipulation.* Microelectromechanical Systems, Journal of, 2008. **17**(3): p. 525-531.
71. Yang, A.H.J., et al., *Optical manipulation of nanoparticles and biomolecules in sub-wavelength slot waveguides.* Nature, 2009. **457**(7225): p. 71-75.

72. Dienerowitz, M., M. Mazilu, and K. Dholakia, *Optical manipulation of nanoparticles: a review.* Journal of Nanophotonics, 2008. **2**(1): p. 021875-021875.
73. Cohen, A.E. and W.E. Moerner, *Suppressing Brownian motion of individual biomolecules in solution.* Proceedings of the National Academy of Sciences of the United States of America, 2006. **103**(12): p. 4362-4365.
74. Lubbe, A.S., C. Alexiou, and C. Bergemann, *Clinical applications of magnetic drug targeting.* Journal of Surgical Research, 2001. **95**(2): p. 200-206.
75. Lubbe, A.S., et al., *Clinical experiences with magnetic drug targeting: A phase I study with 4'-epidoxorubicin in 14 patients with advanced solid tumors.* Cancer Research, 1996. **56**(20): p. 4686-4693.
76. Lubbe, A.S., et al., *Preclinical experiences with magnetic drug targeting: Tolerance and efficacy.* Cancer Research, 1996. **56**(20): p. 4694-4701.
77. Rosensweig, R.E., *Ferrohydrodynamics*. 1985, Mineola, NY: Dover Publications, Inc.
78. Mikkelsen, C.I., *Magnetic separation and hydrodynamic interactions in microfluidic systems*, in *Department of Micro and Nanotechnology*. 2005, Technical University of Denmark: Lyngby, Denmark.
79. Engel-Herbert, R. and T. Hesjedal, *Calculation of the magnetic stray field of a uniaxial magnetic domain.* Journal of Applied Physics, 2005. **97**(7): p. 74504-74505.
80. Domokos, I.H.C., *Computation and visualization of magnetic fields*, in *Department of Image Processing and Computer Graphics*, University of Szeged: Szeged, Hungary.
81. Armani, M., et al. *Micro flow control particle tweezers*. in *uTAS*. 2004. Malmo, Sweden.
82. Armani, M., et al., *Using Feedback Control and Micro-Fluidics to Independently Steer Multiple Particles.* Journal of Micro-Electro-Mechanical Systems, 2006. **15**(4): p. 945-956.
83. Probstein, R.F., *Physicochemical Hydrodynamics: An Introduction*. 2 ed. 1994, New York: John Wiley and Sons, Inc.
84. Meeker, D.C., et al., *Optimal Realization of Arbitrary Forces in a Magnetic Stereotaxis System.* IEEE Transactions on Magnetics, 1996. **32**(2): p. 320 - 328.
85. Creighton, F.M., *Control of Magnetomotive Actuators for an Implanted Object in Brain and Phantom Materials*, in *Department of Physics*. 1991, University of Virginia: Charlottesville. p. 203.
86. Martel, S., et al., *Automatic Navigation of an Untethered Device in the Artery of a Living Animal Using a Conventional Clinical Magnetic Resonance Imaging System.* Applied Physics Letters, 2007. **90**: p. 114105-1:4.
87. Mathieu, J.-B., G. Beaudoin, and S. Martel, *Method of Propulsion of a Ferromagnetic Core in the Cardivascular System Through Magnetic Gradients Generated by an MRI System.* IEEE Transactions on Biomedical Engineering, 2006. **53**(2): p. 292-299.

88. Tamaz, S., et al., *Real-Time MRI-Based Control of a Ferromagnetic Core for Endovascular Navigation.* IEEE Transactions on Biomedical Engineering, 2008. **55**(7): p. 1854-1863.
89. Yesin, K.B., K. Vollmers, and B.J. Nelson, *Modeling and Control of Untethered Biomicrorobots in a Fluidic Environment Using Electromagnetic Fields.* The International Journal of Robotics Research, 2006. **25**(5-6): p. 527-536.
90. Yesin, K.B., K. Vollmers, and B.J. Nelson. *Analysis and design of wireless magnetically guided microrobots in body fluids*. in *Robotics and Automation, 2004. Proceedings. ICRA '04. 2004 IEEE International Conference on*. 2004.
91. Mathieu, J.B. and S. Martel. *In vivo validation of a propulsion method for untethered medical microrobots using a clinical magnetic resonance imaging system*. 2007.
92. Martel, S., et al., *Flagellated Magnetotactic Bacteria as Controlled MRI-trackable Propulsion and Steering Systems for Medical Nanorobots Operating in the Human Microvasculature.* The International Journal of Robotics Research, 2009. **28**(4): p. 571-582.
93. Martel, S., O. Felfoul, and M. Mohammadi. *Flagellated bacterial nanorobots for medical interventions in the human body*. in *Biomedical Robotics and Biomechatronics, 2008. BioRob 2008. 2nd IEEE RAS & EMBS International Conference on*. 2008.
94. Potts, H.E., R.K. Barrett, and D.A. Diver, *Dynamics of freely-suspended drops.* Journal of Physics D-Applied Physics, 2001. **34**(17): p. 2629-2636.
95. Alenghat, F.J., et al., *Analysis of Cell Mechanics in Single Vinculin-Deficient Cells Using a Magnetic Tweezer.* Biochemical and Biophysical Research Communications. **277**(1): p. 93-99.
96. Hosu, B.G., et al., *Magnetic tweezers for intracellular applications.* Review of Scientific Instruments. **74**(9): p. 4158-4163.
97. Vries, A.H.B.d., et al., *Micro Magnetic Tweezers for Nanomanipulation Inside Live Cells.* Biophysical Journal. **88**(3): p. 2137-2144.
98. Kanger, J.S., V. Subramaniam, and R. van Driel, *Intracellular manipulation of chromatin using magnetic nanoparticles.* Chromosome Research: An International Journal on the Molecular, Supramolecular and Evolutionary Aspects of Chromosome Biology. **16**(3): p. 511-522.
99. Amblard, F., et al., *A magnetic manipulator for studying local rheology and micromechanical properties of biological systems.* Review of Scientific Instruments, 1996. **67**(3): p. 818-827.
100. Gosse, C., *Magnetic Tweezers: Micromanipulation and Force Measurement at the Molecular Level.* Biophysical Journal, 2002. **82**(6): p. 3314-3329.
101. Lipfert, J., X. Hao, and N.H. Dekker, *Quantitative Modeling and Optimization of Magnetic Tweezers.* Biophysical Journal, 2009. **96**(12): p. 5040-5049.
102. Wilson, M.W., et al., *Hepatocellular Carcinoma: Regional Therapy with a Magnetic Targeted Carrier Bound to Doxorubicin in a Dual MR Imaging/ Conventional Angiography Suite--Initial Experience with Four Patients.* Radiology, 2004. **230**(1): p. 287-293.

103. Lemke, A.J., et al., *MRI after magnetic drug targeting in patients with advanced solid malignant tumors.* European Radiology, 2004. **14**(11): p. 1949-1955.
104. Polyak, B. and G. Friedman, *Magnetic targeting for site-specific drug delivery: applications and clinical potential.* Expert Opinion on Drug Delivery, 2009. **6**(1): p. 53-70.
105. Widder, K.J., et al., *Tumor Remission in Yoshida Sarcoma-Bearing Rats by Selective Targeting of Magnetic Albumin Microspheres Containing Doxorubicin.* PNAS, 1981. **78**(1): p. 579-581.
106. Hafeli, U.O., et al., *Effective targeting of magnetic radioactive 90Y-microspheres to tumor cells by an externally applied magnetic field. Preliminary in vitro and in vivo results.* Nuclear Medicine and Biology, 1995. **22**(2): p. 147-155.
107. Goodwin, S., et al., *Targeting and retention of magnetic targeted carriers (MTCs) enhancing intra-arterial chemotherapy.* Journal of Magnetism and Magnetic Materials, 1999. **194**(1-3): p. 132-139.
108. Goodwin, S.C., et al., *Single-Dose Toxicity Study of Hepatic Intra-arterial Infusion of Doxorubicin Coupled to a Novel Magnetically Targeted Drug Carrier.* Toxicol. Sci., 2001. **60**(1): p. 177-183.
109. Kubo, T., et al., *Targeted delivery of anticancer drugs with intravenously administered magnetic liposomes in osteosarcoma-bearing hamsters.* International Journal of Oncology, 2000. **17**(2): p. 309-315.
110. Hirao, K., et al., *Targeted gene delivery to human osteosarcoma cells with magnetic cationic liposomes under a magnetic field.* International Journal of Oncology, 2003. **22**(5): p. 1065-1071.
111. Ritter, J.A., K.D. Daniel, and A.D. Ebner, *High gradient magnetic implants for targeted drug delivery.* Abstracts of Papers of the American Chemical Society, 2003. **225**: p. U991-U992.
112. Iacoba, G.H., et al., *Magnetizable needles and wires–modeling an efficient way to target magnetic microspheres in vivo.* Biorheology, 2004. **41**: p. 599–612.
113. Aviles, M.O., et al., *Theoretical analysis of a transdermal ferromagnetic implant for retention of magnetic drug carrier particles.* Journal of Magnetism and Magnetic Materials, 2005. **293**(1): p. 605-615.
114. Rosengart, A.J., et al., *Magnetizable implants and functionalized magnetic carriers: A novel approach for noninvasive yet targeted drug delivery.* Journal of Magnetism and Magnetic Materials, 2005. **293**(1): p. 633-638.
115. Rotariu, O. and N.J.C. Strachan, *Modeling magnetic carrier particle targeting in the tumor microvasculature for cancer treatment.* Journal of Magnetism and Magnetic Materials - Proceedings of the Fifth International Conference on Scientific and Clinical Applications of Magnetic Carriers, 2005. **293**(1): p. 639-646.
116. Yellen, B.B., et al., *Targeted drug delivery to magnetic implants for therapeutic applications.* Journal of Magnetism and Magnetic Materials, 2005. **293**(1): p. 647-654.

117. Shapiro, B., et al. *Control to Concentrate Drug-Coated Magnetic Particles to Deep-Tissue Tumors for Targeted Cancer Chemotherapy*. in *46th IEEE Conference on Decision and Control*. 2007. New Orleans, LA.
118. Shapiro, B., et al., *Dynamic Control of Magnetic Fields to Focus Drug-Coated Nano-Particles to Deep Tissue Tumors*, in *7th International Conference on the Scientific and Clinical Applications of Magnetic Carriers*. 2008: Vancouver, British Columbia.
119. Shapiro, B., *Towards Dynamic Control of Magnetic Fields to Focus Magnetic Carriers to Targets Deep Inside the Body.* Journal of Magnetism and Magnetic Materials, 2009. **321**(10): p. 1594-1599.
120. Locascio, L.E., C.E. Perso, and C.S. Lee, *Measurement of electroosmotic flow in plastic imprinted microfluid devices and the effect of protein adsorption on flow rate.* Journal of Chromotography A, 1999. **857**: p. 275-284.
121. Harrison, D.J., et al., *Micromachining a Miniaturized Capillary Electrophoresis-Based Chemical-Analysis System on a Chip.* Science, 1993. **261**(5123): p. 895-897.
122. Manz, A., et al., *Electroosmotic Pumping and Electrophoretic Separations for Miniaturized Chemical-Analysis Systems.* Journal of Micromechanics and Microengineering, 1994. **4**(4): p. 257-265.
123. Chaudhary, S. and B. Shapiro, *Arbitrary Steering of Multiple Particles at Once in an Electroosmotically Driven Micro Fluidic System.* IEEE Trans. on Control Systems Technologies, 2004: p. submitted.
124. Feynman, R.P., R.B. Leighton, and M. Sands, *The Feynman Lectures on Physics*. 1964: Addison-Wesley Publishing Company.
125. Chaudhary, S. and B. Shapiro, *Arbitrary steering of multiple particles at once in an electroosmotically driven microfluidic system.* IEEE Transactions on Control Systems Technology, 2006. **14**(4): p. 669-680.
126. Strang, G., *Linear Algebra and Its Applications*. 3 ed. 1988, New York, NY: Brooks Cole. 520 pages.
127. Rodriguez, I. and N. Chandrasekhar, *Experimental study and numerical estimation of current changes in electroosmotically pumped microfluidic devices.* ELECTROPHORESIS, 2005. **26**(6): p. 1114-1121.
128. Venkataraman, P., *Applied optimization with MATLAB programming*. 2002: Wiley-IEEE.
129. Regele, R. and P. Levi. *Cooperative Multi-Robot Path Planning by Heuristic Priority Adjustment*. in *2006 IEEE/RSJ International Conference on Intelligent Robots and Systems*. 2006. Beijing, China.
130. Kalman, R., Emil, *A New Approach to Linear Filtering and Prediction Problems.* Transactions of the ASME--Journal of Basic Engineering, 1960. **82**(Series D): p. 35-45.
131. Roland Probst, Z.C., Benjamin Shapiro, *Electrokinetic tweezers: living cells manipulation by vision sensing and feedback control.* Nature Protocols, 2009: p. accepted with revisions.
132. Probst, R., Z. Cummins, and B. Shapiro, *Steering swimming microbes by vision sensing and flow control.* Lab-On-A-Chip, 2009: p. submitted.

133. Chad, R., et al., *Manipulating Quantum Dots to Nanometer Precision by Control of Flow*. Nano Letters, Manuscript ID: nl-2010-01105j, 2009.
134. Light, T.S., Kingman, E.A., and Bevilacqua, A.C. *The Conductivity of Low Concentrations of CO2 Dissolved in Ultrapure Water From 0-100°C*. in *209th American Chemical Society National Meeting*. 1995. Anaheim, CA.
135. Liu, Y., Fanguy, J.C., et al., *Dynamic Coating Using Polyelectrolyte Multilayers for Chemical Control of Electroosmotic Flow in Capillary Electrophoresis Microchips.* Analytical Chemistry, 2000. **72**: p. 5939-44.
136. Spehar, A.M., et al., *Electrokinetic characterization of poly(dimethylsiloxane) microchannels.* Electrophoresis, 2003. **24**(21): p. 2674-8.
137. Vanifatova, N.G., et al., *Separation of unmodified polystyrene nanosphere standards by capillary zone electrophoresis.* J Chromatogr A., 2000. **898**(2): p. 257-63.
138. Jones, H.K., and Ballou, N.E., *Separations of chemically different particles by capillary electrophoresis.* Analytical Chemistry, 1990. **62**(22): p. 2484-90.
139. Nakari-Setala, T.e.a., *M. Expression of a fungal hydrophobin in the Saccharomyces cerevisiae cell wall: effect on cell surface properties and immobilization.* Appl Environ Microbiol, 2002. **2002**(68): p. 7.
140. Vargas, F.F., et al, *Surface charge of endothelial cells estimated from electrophoretic mobility.* Membrane Biochemistry, 1989. **8**(4): p. 221-7.
141. Smith, B.A., Ware, B.R., Weiner, R.S., *Electrophoretic distributions of human peripheral blood mononuclear white cells from normal subjects and from patients with acute lymphocytic leukemia.* Proc Natl Acad Sci U S A., 1976. **73**(7): p. 2388-91.
142. Elimelech, M.a.O.M.C.R., *Effect of Electrolyte Type on the Electrophoretic Mobility of Polystyrene Latex Colloids.* Colloids and Surfaces, 1990. **44**: p. 165-178.
143. Xia, Y.N. and G.M. Whitesides, *Soft lithography.* Annual Review of Materials Science. **28**: p. 153-184.
144. *SYLGARD® 184 SILICONE ELASTOMER KIT*. [cited; Available from: http://www.dowcorning.com/applications/search/default.aspx?R=131EN.
145. Acar, Y.B., Alshawabkeh, A. N., Parker, R.A., *Theoretical and experimental modeling of multi-species transport in soils under electric fields project summary*. 1997, Cincinnati, OH: U.S. Environmental Protection Agency, National Risk Management Research Laboratory.
146. Slivinsky, G.G., et al., *Cellular electrophoretic mobility data: A first approach to a database.* Electrophoresis, 1997. **18**(7): p. 1109-1119.
147. Mehrishi, J.N. and J. Bauer, *Electrophoresis of cells and the biological relevance of surface charge.* ELECTROPHORESIS, 2002. **23**(13): p. 1984-1994.
148. Camp, J.P. and A.T. Capitano, *Size-dependent mobile surface charge model of cell electrophoresis.* Biophysical Chemistry, 2005. **113**(2): p. 115-122.
149. Takamura, Y., et al., *Low-voltage electroosmosis pump for stand-alone microfluidics devices.* ELECTROPHORESIS, 2003. **24**(1-2): p. 185-192.

150. Dasgupta, P.K. and S. Liu, *Electroosmosis: A Reliable Fluid Propulsion System for Flow Injection Analysis.* Analytical Chemistry, 1994. **66**(11): p. 1792-1798.
151. Lazar, I.M. and B.L. Karger, *Multiple Open-Channel Electroosmotic Pumping System for Microfluidic Sample Handling.* Analytical Chemistry, 2002. **74**(24): p. 6259-6268.
152. Ross, D., M. Gaitan, and L.E. Locascio, *Temperature Measurement in Microfluidic Systems Using a Temperature-Dependent Fluorescent Dye.* Analytical Chemistry, 2001. **73**(17): p. 4117-4123.
153. Walker, S. and B. Shapiro, *A Control Method for Steering Individual Particles Inside Liquid Droplets Actuated by Electrowetting.* Lab on a Chip, 2005. **12**(1): p. 1404 -1407.
154. C. Ropp, R.P.Z.C.R.K.S.R.R.E.W.B.S., *Manipulating Quantum Dots to Nanometer Precision by Control of Flow.* Science manuscript submitted, Manuscript Number: 1185687, 2009.
155. Kumar, R., et al., *Wormlike Micelles of a C22-Tailed Zwitterionic Betaine Surfactant : From Viscoelastic Solutions to Elastic Gels.* Langmuir, 2007. **23**: p. 12849-12856.
156. Kumar, R. and S.R. Raghavan, *Thermo-thickening in solutions of telechelic associating polymers and cyclodextrins.* Langmuir, 2009: p. in press-in press.
157. Thompson, R.E., D.R. Larson, and W.W. Webb, *Precise nanometer Localization Analysis for Individual Fluorescent Probes.* Biophysical Journal, 2002. **82**: p. 2775-2783.
158. Berglund, A.J., K. McHale, and H. Mabuchi, *Feedback localization of freely diffusing fluorescent particles near the optical shot-noise limit.* Optics Letters, 2007. **32**(2): p. 145-147.
159. Michler, P., et al., *Quantum correlation among photons from a single quantum dot at room temperature.* Nature, 2000. **406**(6799): p. 968-970.
160. Zhang, Q., et al., *Large ordered arrays of single photon sources based on II-VI semiconductor colloidal quantum dot.* Opt. Express, 2008. **16**(24): p. 19599, 19592-19599, 19592.
161. Liu, J., et al., *Controlled photopolymerization of hydrogel microstructures inside microchannels for bioassays.* Lab on a Chip, 2009. **9**(9): p. 1301-1305.
162. Barz, D.P.J. and P. Ehrhard, *Model and verification of electrokinetic flow and transport in a micro-electrophoresis device.* Lab on a Chip, 2005. **5**(9): p. 949-958.
163. Santiago, J.G., *Electroosmotic Flows in Microchannels with Finite Inertial and Pressure Forces.* Analytical Chemistry, 2001. **73**(10): p. 2353-2365.
164. Laser, D.J. and J.G. Santiago, *A review of micropumps.* J. Micromech. Microeng., 2004. **14**: p. R35-R64.
165. Probst, R., Z. Cummins, and B. Shapiro, *Electrokinetic tweezers: living cells manipulation by vision sensing and electrokinetic feedback control.* Nature Protocols, 2010: p. accepted with revisions.
166. Cohen, A.E. and W.E. Moerner, *Controlling Brownian motion of single protein molecules and single fluorophores in aqueous buffer.* Optics Express, 2008. **16**(10): p. 6941-6956.

167. Mathai, P.P., et al., *Simultaneous Positioning and Orientation of a Single Nanorod by Flow Control.* Under review, 2010.
168. Walker, S.W., B. Shapiro, and R.H. Nochetto, *Electrowetting with Contact Line Pinning: Computational Modeling and Comparisions with Experiments.* Physics of Fluids, 2009. **23**(10): p. 102103.
169. Gorman, J. and B. Shapiro, eds. *Feedback Control of Systems on the Micro- and Nano-Scales: from MEMS to Atoms*. Microsystems Series, ed. S. Senturion. 2010, Springer-Verlag: New York, NY.
170. King, J.K., et al., *Microfluidic Device for the 3-D Electrokinetic Manipulation of Single Molecules.* 2009.
171. Pavani, S.R.P., et al., *Three-dimensional, single-molecule fluorescence imaging beyond the diffraction limit by using a double-helix point spread function.* Proceedings of the National Academy of Sciences, 2009. **106**(9): p. 2995-2999.
172. Pavani, S.R.P. and R. Piestun, *Three dimensional tracking of fluorescent microparticles using a photon-limited double-helix response system.* Optics Express, 2008. **16**(26): p. 22048-22057.
173. Jo, B.-H., et al., *Three-dimensional micro-channel fabrication in polydimethylsiloxane (PDMS) elastomer.* J. Microelectromech. Syst., 2000. **9**(1): p. 76 - 81.
174. Zhang, M., et al., *A simple method for fabricating multi-layer PDMS structures for 3D microfluidic chips.* Lab on a Chip. **10**(9): p. 1199-1203.
175. Zhou, T., et al., *Physicochemical and Engineering Aspects : Time-dependent starting profile of velocity upon application of external electrical potential in electroosmotic driven microchannels.* Colloids and Surfaces A, 2006. **277**(1-3): p. 136-144.
176. Yan, D., et al., *Visualizing the transient electroosmotic flow and measuring the zeta potential of microchannels with a micro-PIV technique.* The Journal of Chemical Physics, 2006. **124**(2): p. 021103-4.
177. Yu, J., et al., *Nanoscale 3D Tracking with Conjugated Polymer Nanoparticles.* Journal of the American Chemical Society, 2009. **131**(51): p. 18410-18414.
178. Forbes, Z.G., et al., *An approach to targeted drug delivery based on uniform magnetic fields.* IEEE Transactions on Magnetics, 2003. **39**(5): p. 3372-3377.
179. Fleisch, D.A., *A student's guide to Maxwell's equations*. 2008, Cambridge, UK; New York: Cambridge University Press.
180. Forbes, Z.G., et al., *Validation of high gradient magnetic field based drug delivery to magnetizable implants under flow.* IEEE Transactions on Biomedical Engineering, 2008. **55**(2 Part 1): p. 643-649.
181. Incropera, F.P., *Fundamentals of heat and mass transfer*. 2007, Hoboken, NJ: John Wiley.
182. Saltzman, W.M., *Drug delivery: engineering principles for drug therapy*. 2001, New York, NY: Oxford University Press.
183. Smith, N.P., A.J. Pullan, and P.J. Hunter, *An anatomically based model of transient coronary blood flow in the heart.* SIAM Journal on Applied mathematics, 2001: p. 990-1018.

184. Odenbach, S., *Magnetoviscous Effects in Ferrofluids*. 2002: Springer.
185. Zubarev, A.Y., S. Odenbach, and J. Fleischer, *Rheological properties of dense ferrofluids. Effect of chain-like aggregates.* Journal of magnetism and magnetic materials, 2002. **252**: p. 241-243.
186. Wu, M., et al., *Magnetic field-assisted hydrothermal growth of chain-like nanostructure of magnetite.* Chemical Physics Letters, 2005. **401**(4-6): p. 374-379.
187. Mendelev, V.S. and A.O. Ivanov, *Ferrofluid aggregation in chains under the influence of a magnetic field.* Physical Review E, 2004. **70**(5): p. 51502.
188. Wang, Z. and C. Holm, *Structure and magnetic properties of polydisperse ferrofluids: A molecular dynamics study.* Physical Review E, 2003. **68**(4): p. 41401.
189. Lehmann, U., et al., *Two-dimensional magnetic manipulation of microdroplets on a chip as a platform for bioanalytical applications.* Sensors and Actuators B: Chemical. **117**(2): p. 457-463.
190. Creighton, F.M. *Optimal Distribution of Magnetic Material for Catheter and Guidewire Cardiology Therapies*. in *Magnetics Conference (INTERMAG 2006)*. 2006. San Diego, CA: IEEE International.
191. Choi, J.-S. and J. Yoo, *Design of a Halbach Magnet Array Based on Optimization Techniques.* IEEE Transactions on Magnetics, 2008. **44**(10): p. 2361-2366.
192. Alexiou, C., et al., *A High Field Gradient Magnet for Magnetic Drug Targeting.* Applied Superconductivity, IEEE Transactions on, 2006. **16**(2): p. 1527-1530.
193. Shapiro, B., I. Rutel, and K. Dormer, *A System to Inject Therapeutically-Coated Magnetic Nano-Particles into the Inner Ear: Design and Initial Validation*, in *Proceedings on the 3rd International Conference on Micro- and Nanosystems (IDETC 200)*. 2009, ASME: San Diego, CA.